Developing a Framework for Thermodynamic Measurements of Fluoride Salt Nuclear Fuel

by

Daniel Bryan Hallatt

A thesis submitted to the School of Graduate and Postdoctoral Studies in partial fulfillment of the requirements for the degree of

Master of Applied Science in Nuclear Engineering

Faculty of Energy Systems and Nuclear Science
Ontario Tech University
Oshawa, Ontario, Canada
October 2019

Thesis Examination Information

Submitted by: **Daniel Hallatt**

Master of Applied Science in Nuclear Engineering

Thesis title:
Developing a Framework for Thermodynamic Measurements of Fluoride Salt Nuclear Fuel

An oral defense of this thesis took place on October 15, 2019 in front of the following examining committee:

Examining Committee:	
Chair of Examining Committee	Prof. Brian Ikeda
Research Supervisor	Prof. Markus Piro
Examining Committee Member	Prof. Matthew Kaye
Thesis Examiner	Dr. Daniel Cluff

Abstract

With a single liquid acting simultaneously as a primary coolant and a nuclear fuel, molten salt reactor development has been challenged with understanding the behaviour of its complex fluoride solution under various conditions. Experimental thermodynamics can address part of this challenge by providing insights into the system's behaviour, such as melting points, heat capacities, and solubilities.

The current work develops an experimental framework for studying the experimental thermodynamics of fluoride nuclear salt materials. By establishing experimental capabilities and practises, experimental routines are qualified with the goal of providing background on the environment of error of future thermodynamic measurements using differential scanning calorimetry.

Infrastructure, standard procedures, a custom crucible, and qualification of a routine for thermodynamic measurements have been developed. Study on particle size reduction, material interactions, and techniques for purification demonstrated a promising environment for thermodynamic measurements.

Keywords: thermodynamics; molten salt reactor; nuclear

Acknowledgements

I want to extend my thanks to my supervisor Prof. Markus Piro at University of Ontario Institute of Technology who gave me the opportunity to begin my research career in an area of science I am passionate about. I also want to acknowledge the inviting environment that Prof. Piro has instilled within his Nuclear Fuels and Materials Group, where my daily questions and requests for advice never seemed to burden anyone. I also would like to formally thank Prof. Matthew Kaye at University of Ontario Institute of Technology not only for allowing me to use (and break) as much equipment as I wanted to within his lab, but also for the intimate discussions on experimental design we shared. Thanks should also be made to all of the graduate students, post-doctoral fellows, and undergraduate students of the Nuclear Fuels and Materials Group, for their help when working together on a number of projects and for their honest advice. The lab technicians Robert Ulrich and Callan Brown, and the two security officers for the Faculty of Energy Systems and Nuclear Science at University of Ontario Institute of Technology also deserve many thanks, for their help with facilitating my experimental measurements during some tight timelines.

Furthermore I would like to acknowledge Dr. Ondřej Beneš and Dr. Rudy J. M. Konings, both from the European Commission Joint Research Centre; and also Dr. Elisa Capelli from the Frascati Research Centre for their invaluable advice when sharing their wealth of experience with me. Vaughn Shaw of Advanced Machining and Imran Atcha should also certainty be acknowledged for their understanding and time in turning my conceptual crucible design into a real prototype. There are many collaborators who I also had routine conversations with as part of an informal working-group. These individuals include Dr. Ted Besmann, Kaitlin Johnson, and Denise Adorno Lopes of the University of South Carolina, and Dr. Stephen Raiman, Dr. Jake McMurray, and Dr. Joanna McFarlane of Oak Ridge National Laboratory. These individuals actively included me in a large collaborative effort in developing related salt research and provided copious amounts of advice for my efforts at University of Ontario Institute of Technology. Lastly, Canadian Nuclear Laboratories is also due acknowledgement, where I was hosted to participate in a series of experiments with their remarkably experienced staff to study irradiated molten salts within one of their hot cell facilities.

This research was undertaken, in part, thanks to funding from the Canada Research Chairs (950-231328) program of the Natural Sciences and Engineering Research Council of Canada. Funding for equipment from the Canadian Foundation for Innovation and the Ontario Ministry of Economic Development are greatly appreciated.

Author's Declaration

I hereby declare that this thesis consists of original work which I have authored. This is a true copy of the thesis, including any required final revisions, as accepted by my examiners.

I authorize the University of Ontario Institute of Technology to lend this thesis to either institutions or individuals for the purpose of scholarly research. I further authorize the University of Ontario Institute of Technology to reproduce this thesis by photocopying or by other means, in total or in part, at the request of other institutions or individuals for the purpose of scholarly research. I understand that my thesis will be made electronically available to the public.

Daniel Hallatt

Statement of Contributions

The data used to generate Figure 3.7 was provided by Dr. Bernie Fitzpatrick of the Nuclear Fuels and Materials Group at Ontario Tech University. I constructed the figure from the raw data file.

Contents

List of Figures

List of Tables

Abbreviations

ARE Aircraft Reactor Experiment.

ASTM American Society for Testing and Materials.

BN Boron Nitride.

CALPHAD CALculation of PHAse Diagrams.

CMSR Compact Molten Salt Reactor.

DMM Direct Mixing Method.

DSC Differential Scanning Calorimetry.

DTA Differential Thermal Analysis.

ERC Energy systems and nuclear science Research Centre.

EXAFS Extended X-ray Absorption Fine Structure.

GIF Generation IV International Forum.

HDPE High Density PolyEthylene.

ICDD International Center for Diffraction Data.

ICP-MS Inductively Coupled Plasma-Mass Spectrometry.

ICP-OES Inductively Coupled Plasma-Optical Emission Spectrometry.

IMSBR Indian Molten Salt Breeder Reactor.

IMSR Integral Molten Salt Reactor.

KEMS Knudsen Effusion Mass Spectrometry.

LFTR Liquid Fluoride Thorium Reactor.

MOSART MOlten Salt Actinide Recycler and Transmuter.

MSBE Molten Salt Breeder Experiment.

MSBR Molten Salt Breeder Reactor.

MSFR Molten Salt Fast Reactor.

MSR Molten Salt Reactor.

MSRE Molten Salt Reactor Experiment.

NFMG Nuclear Fuels and Materials Group.

NMR Nuclear Magnetic Resonance.

ORNL Oak Ridge National Laboratory.

PLM Polarized Light Microscopy.

REE Rare Earth Elements.

SMR Small Modular Reactor.

SOP Standard Operating Procedure.

SSR Stable Salt Reactor.

STA Simultaneous Thermal Analysis.

TAF-ID Thermodynamics of Advanced nuclear Fuels - International Database.

TGA Thermal Gravimetric Analysis.

THORCON THORium CONverter reactor.

TMSR Thermal Molten Salt Reactor.

TRU Transuranic Waste.

UOIT University of Ontario Institute of Technology.

USC University of South Carolina.

XRD X-Ray Diffraction.

CHAPTER 1

Introduction

With a maturing standard of living and a growing population, today's developing society is challenged with an increasing demand for energy [1–5]. Localized, critical demands for energy are also confronting the population, as consequences of climate change strain the international energy landscape in some of the world's most vulnerable regions [2]. Moreover, burgeoning concerns for commercial environmental responsibility are also developing, causing the sustainability of the energy sector to be scrutinized and identifying quickly that energy production is a primary component in the discussion on climate change [5–7]. It is clear that a successful energy landscape must provide a reliable, sustainable, economical, flexible, and safe energy to both dense and sparse populations in the modern world [5, 8–10].

Within the energy sector, electricity has established itself as the central supply to the complex energy demand; in 2018, not only was two-thirds of global energy demand met with electricity, but the increase in demand for electricity was nearly double that of energy as a whole [2]. As an alternative to carbon-based energy, elec-

tricity generated by nuclear power is a highly reliable, economical, safe, efficient, and deployable source of electricity utilized by many nation states [2, 5, 10]. Comparing alternative energy options, evidence continues to suggest that nuclear energy may not only provide a reliable and efficient source of energy, but that nuclear power can meet the economic, environmental, and safety interests of a modern energy landscape [5–7, 10–14]. However, as evidenced by continued relapses to coal and natural gas, and with large infrastructural costs limiting nuclear to centralized, base-load demand, developing improved next generation nuclear energy technologies is required if increasing concerns regarding climate change and energy demand are to be met by means of nuclear energy [2, 10].

As an international group of technical experts, the Generation IV International Forum (GIF) was initiated by the US Department of Energy in 2002 to identify promising new generation nuclear energy technologies and to establish research and development requirements to benefit the deployment of such. The GIF described, and continues to update progress on, six promising reactor designs in roadmaps for next generation nuclear energy in a modern energy landscape [15, 16]. By developing a suite of next generation nuclear power reactors, the objective of the GIF is to address areas of improvement in traditional nuclear energy with highly efficient, safe, reliable, economical, and proliferation resistant nuclear reactor designs [16].

One of the technologies recommended by the GIF is called the Molten Salt Reactor (MSR) [17]. The MSR is a highly non-conventional reactor design, defined by a single, circulating, inorganic fluid (molten salt) to serve as both a primary circuit working fluid and a solvent for fissile nuclear fuel content. The result of such a design is a source of electricity which maintains the high energy density, reliability, and low carbon (and physical) footprint of conventional nuclear energy, while benefitting from advancements in safety, cost, and efficiency [18, 19]. While the potential versatility of the MSR concept affords the design with applicability to meet both base-load and lo-

calized, small scale energy demand (*e.g.*, Small Modular Reactors [SMRs]), the MSR design also provides flexibility in its ability to adapt to number of supplementary functions, such as breeding fertile material or burning inventories of nuclear waste from other reactor types.

One of the strongest justifications for developing the MSR is the inherent, passive safety afforded by use of a liquid nuclear fuel. By employing a nuclear fuel in a liquid state, passive safety makes the MSR inherently tolerant and predictable to power excursions with the fuel's highly negative temperature and reactivity coefficients [18, 19]. In such a way, safety of the MSR can be achieved intrinsically, affording the MSR with potential economic and licensing benefits. Considering the theorized proposals for high fuel utilization, increased margins for accident safety, fuel versatility, reduced fissile inventories, improved thermal efficiencies, demand driven scalability, and breeding/burning options, the MSR demonstrates a promising multifunctional source of energy that could potentially compete with the complexities of a modern energy landscape [10, 14, 20].

However, as routinely summarized by the GIF, a number of challenges in developing a commercial MSR have been identified [16]. Independent conclusions indicating the MSR's low technology readiness level is evidence of this challenge [5, 14]. Understandably, the novelty of a liquid fuelled nuclear reactor introduces an area of inexperience and uncertainty regarding the ability to leverage knowledge pertaining to solid fuelled nuclear reactors. With the liquid state of the fuel, a majority of considerations including neutronics, corrosion, thermal system management, proliferation, safeguards, and fission product behaviour are required to be re-evaluated to a much more thorough extent than if the reactor was simply a modification of a solid-fuel design. Benefiting from experience made in the development of solid fuelled nuclear reactors, one area requiring considerably more understanding is the behaviour of the fuel itself. As a result of the high operating temperature and the liquid state of the

fissile inventory, fuel behaviour is of particular importance with regards to the safety, efficiency, lifetime, and economics of the generation IV reactor.

The topic of this thesis aims to contribute to the community's understanding of prospective MSR fuel behaviour by establishing capabilities in fabricating and studying the nuclear fuel at University of Ontario Institute of Technology (UOIT). This thesis outlines the development and qualification of standardized fabrication and processing methods of molten salt nuclear fuel and provides foundation and outline for experimental campaigns in molten salt fuel thermodynamics by the Nuclear Fuels and Materials Group (NFMG).

CHAPTER 2

The Molten Salt Reactor Concept

Illustrated in Figure 2.1 is a prospective representation of how full employment of molten salts in a nuclear power plant setting may be achieved. Figure 2.1 presents a general concept, which not only employs molten salt as a working fluid for heat transfer but also to serve as fissile fuel solvent within the reactor core. While as a primary heat transfer fluid, dissolved fissile content provides heat to its own molten solvent as it flows through the reactor core. Exiting the reactor core with a high temperature (*e.g.* 600 °C, the molten salt solution may then transfer its thermal energy to secondary coolant loops for practical use such as the generation of electricity or high temperature industrial applications. With beneficial heat transfer properties, Figure 2.1 also illustrates how molten salt compositions may also be designed for use as secondary coolant fluids. This secondary salt loop represents a challenge in some MSR designs: separating the highly radioactive fission products of the fuel solution from the steam system of electricity generation.

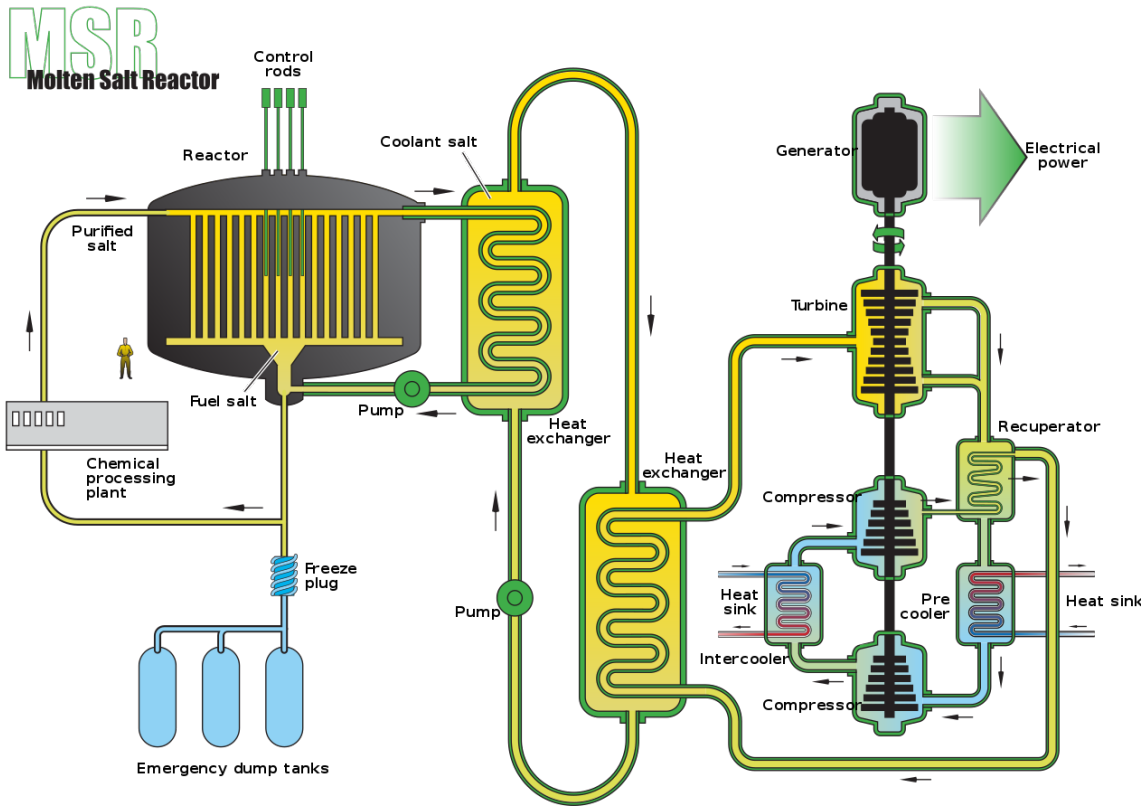

Figure 2.1. A schematic of a general MSR concept [15].

The typical fuel-coolant mixture in an MSR is based on a lithium fluoride (LiF) solvent. However, it is also common for supplementary components (such as KF, NaF, ZrF_4, BeF_2, RbF, *etc.*) to be added to the LiF solvent for optimizing physical properties of the solution, such as fission product and actinoid solubility, melting point, viscosity, corrosion/electrochemistry, and neutronic properties [21, 22]. However with such materials, the employment of salt facing materials for the MSR design is a unique challenge due to the highly corrosive nature of the liquid salts at high temperatures. Nickel or molybdenum alloys have been found to be the typical material of choice to minimize wall-salt interactions, where Oak Ridge National Laboratory (ORNL) has even developed an alloy designed specifically for the MSR, *Hastelloy-N* [18]. The liquid state of the nuclear fuel also suggests that the design of an MSR can facilitate management of the fuel during operation. As a result, a number of developing MSR

designs include additional online fuel management techniques, such as gaseous sparging, precipitate filtering, chemical reprocessing, refuelling, and redox control. Beyond the capability of the MSR to utilize transuranic waste as fuel, MSRs have also been conceptualized as breeder reactors with single-fluid or two-fluid designs. However, with such capabilities the MSR is challenged with proliferation and fuel handling concerns.

By designing a nuclear power reactor to operate with dissolved fissile fuel in a liquid solution of coolant, a number of distinct improvements can be realized over traditional nuclear power. Firstly, with the events experienced at the Fukushima Daiichi Nuclear Power Plant in 2011, inherent safety features are a neoteric motive for continued interest in the MSR. One of the most intriguing safety characteristics of a liquid nuclear fuel for example is its inherent negative temperature reactivity coefficient [17, 19]. With the MSR design achieving criticality when the fuel reaches a liquid state the fission reaction is driven towards a slower reaction rate if temperature increases [19]. In this sense, the MSR operates with a neutronic driving force towards a subcritical state, requiring constant criticality preservation. This behaviour is unlike most solid fuelled nuclear reactors, which demand attentive control of the reactor to prevent an inherent drive towards supercriticality.

The liquid state of the fuel in a MSR has also led conceptual MSR designs to include subcritical fuel drain tanks: gravitationally fed, freeze plug induced tanks for removal of fuel solution from the reactor core to subcritical geometries without moderation. Such a design is reflected in the conceptual MSR plant design illustrated in Figure 2.1. Coupled with negative reactivity coefficients, the MSR is afforded with passive reactivity assurance safeguards inherent to the physics of the reactor. Additionally, not only does the opportunity for online fission product removal in some designs reduce the production of valuable nuclear waste by improving fuel utilization in the MSR design, but delayed decay heat associated with a loss of coolant accident

or after reactor shutdown may be reduced [18, 19, 23]. Radioactivity of the reactor core is also reduced as a result, consequently diminishing radioactivity available for release during a severe accident [18].

Another advantage afforded by using molten salt as a coolant material is the improved heat transfer in comparison to conventional water cooled reactors. Working with a high margin from its boiling point, the low pressure system of a MSR design further mitigates the risk of radioactivity release by reducing the potential for over pressurization. The potential for fuel-clad gap fission product collection, and other challenges introduced by a fuel-sheath design are also mitigated with use of a liquid fuel as in the MSR [24]. Fission product removal and online control of the fissile concentration is further attributed to an absence of excess reactivity required by the conventional solid fuelled reactors to compensate for the build-up of poisonous fission products [18].

Before commitment is made to the design of a nuclear power reactor, however, it is vital that a robust understanding and prediction of the chemical, phase, and isotopic evolution of the reactor be constructed. The liquid state and flowing nature of the fuel within the MSR complicates this by coupling heat and mass transport, thermodynamics, and reactor kinetics/neutronics, to thermalhydraulics. Coupled with the use of a high temperature and liquid form of highly corrosive salt solution, if a design of a MSR includes a form of fuel maintenance, such as fission product removal or online refuelling, predictive capabilities and experimental evidence must also consider the effects of corrosion, fuel chemistry, and electrochemistry to a much more exhaustive extent. With such a dynamic nature of the fissile fuel in a MSR, understanding a number of design characteristics such as fuel behaviour, neutronics, and fuel maintenance is challenged. Clearly, some of the inherent challenges with the development of the MSR design are related to the sciences of the nuclear fuel.

CHAPTER 3

Literature Review

The performance of nuclear fuel is influenced by phenomena such as fission, activation, radioactive decay, diffusion, chemical reactions, and irradiation in a reactor environment. In the environment of a solid fuelled reactor for example, Piro *et al.* demonstrated how subjects such as isotopic evolution, heat transfer, and thermochemistry have been coupled to predict a number of phenomena experienced by UO_2 fuel [25]. In liquid fuelled reactors, this environment is markedly different. Not only may it be appropriate to consider additional phenomenon such as fluid mechanics and corrosion, but an understanding of fuel behaviour may need to support a largely different range of thermal, chemical, and irradiation conditions. Liquid fuelled reactors also demand different design requirements on fuel behaviour such as the maintenance of a liquid state, its solubility for actinoids and selective fission products, and its redox control for corrosion behaviour. Complicated by the homogeneous liquid state of the fuel, it is clear that knowledge gained on conventionally fuelled reactors is not directly transferable to the MSR concept.

By invoking chemical thermodynamics, the equilibrium boundary conditions of fuel behaviour may be better understood by providing driving forces on the phase and state of the system. Such properties of a fuel are likewise directly related as inputs to other fuel behaviour topics such as heat transfer, mechanical behaviour, corrosion, and isotopic evolution. For the MSR, chemical thermodynamics of the fuel must not only provide confidence that the fuel is in a liquid state and that it is soluble in the salt solution, but that it does so through a relatively large range of temperature and composition conditions as the liquid flows through the reactor-heat exchanger primary circuit. A number of auxiliary considerations in an MSR design are also related to the chemical thermodynamics of the fuel, such as fuel maintenance, fission product removal, and fuel species additions for material property improvement. In such arguments, solubilities of transient species such as fission, activation, corrosion, and decay products, along with intentionally added species, must be understood through the range of potential conditions of a particular MSR design. Other aspects of fuel behaviour such as kinetics based theories are also important to this discussion; however, thermodynamics provides the unique insight into the equilibrium boundary conditions which other behaviour are inherently bound between.

With the liquid fuel of an MSR continuously subject to changing thermal and chemical states, there is motivation for developing a thermodynamic understanding of the fuel's behaviour in the form of a multi-component treatment. Such a treatment is most commonly visualized by phase diagrams for binary or ternary systems [26–29]. Phase diagrams can not only provide insight into properties such as liquidus, solidus, and solvus surfaces, but also the sensitivity of such properties to temperature or compositional variations. Early work from ORNL demonstrates this importance, where high operating temperatures permitted by the use of a liquid nuclear fuel approached the upper limits of structural materials at the time.

An international effort by the modern MSR community has been therefore focused

on the development of a systematic approach for employing both first principles and experimental results in thermodynamic model development for molten salt chemical systems [20, 28–32]. Utilizing the CALculation of PHAse Diagrams (CALPHAD) method, predictions on the phase stability of nuclear fuel may be enabled by construction of phase diagrams extrapolated continuously through X-T-P between limited experimental information [32–34]. A practical example of the utility of a comprehensive database is an international database called the Thermodynamics of Advanced nuclear Fuels - International Database (TAF-ID). The TAF-ID is an effort at the forefront of developing a collection of knowledge on the thermodynamic behaviour of solid state UO_2 fuel compositions [35]. By developing a similar thermodynamic database on molten salt fuel compositions, evaluations and predictions can be made on a salt's thermochemical properties, which can permit optimizations on the composition of MSR fuel systems to be performed specific to reactor intentions (breeding, burning, converting, *etc.*) [28]. An extensive thermodynamic database would also aid in predicting fuel behaviour in the event of changing conditions in the reactor such as accident scenarios or fuel maintenance schemes. Required to make such predictions is accurate thermodynamics data to fit empirical models. Specifically within the nuclear sector, where the basis of safety and licensing is on empirical evidence, a progressively large value is placed on obtaining such information through experimental measurements.

3.1 Experimental Thermodynamics

The earliest literature found on thermodynamics related to MSR fuel was reported on homogenous fuelled reactors in 1951 [36]. Shortly thereafter, as a product of ORNL's initial interest in MSR technology, the Molten Salt Breeder Reactor (MSBR) and Molten Salt Reactor Experiment (MSRE) provided the community with a large quantity of MSR fuel specific thermodynamics research from the 1950's to the mid-1960's, as evidenced by two extensive reviews by Thoma *et al.* [26, 27]. It is evident

from these reviews that interest in performing thermodynamic studies in the molten salt space was in part thanks to its ability to predict phase behaviour of molten salt mixtures and subsequently provide partial clarity in the discussion of fuel solvent choice. Compositions of solvents for actinoid elements were clearly an interest at the time, as most phase diagrams predominantly described fission product free chemical compositions of salt mixtures [26, 27, 37]. Despite an impressive number of phase diagrams organized by Thoma *et al.*, early understandings of such systems were also a result of compositionally low resolution conclusions drawn from semi-quantitative experimental techniques [26, 27].

At the time, experimentally proposed phase diagrams were constructed solely from evidence on phase boundary positions themselves, as thermodynamic modelling efforts could not capture the complex behaviour of molten salts. Tucker *et al.* explained that the primary techniques employed by such efforts were various forms of quench analyses, who's direct measurements on phase boundary locations were commonly coupled with deductions made from thermal analyses [37]. As a result, campaigns on experimental MSR fuel thermodynamics were performed to resolve phase boundary locations which supported conclusions drawn from a number of coupled techniques [26, 27]. However, with the inherent compositional sensitivity of thermodynamics measurements, and the hygroscopic, reactive nature of molten fluoride salts, researchers were tasked with developing experimental infrastructure which could provide confident measurements from such techniques in a controllable and reliable manner. For example, researchers from Mound Laboratories developed an exceptionally novel suite of experimental infrastructure which afforded the community with robust thermal gradient quenching, thermal analysis, and quench shouldering capabilities specific for molten salt materials [38, 39]. Such infrastructure was then adopted and committed to by ORNL, where reports were published discussing improvements to the designs and and additions to the experimental campaigns such as high temperature phase-filtering [37–39].

In early quench analyses reported by ORNL, known compositions of salt samples were first equilibrated in a thermal gradient furnace, where a material could be subject to a definitive thermal gradient. The material under assumed equilibrium was subjected to a rapid thermal quench by use of a floor shutter, to capture the equilibrium phase behaviour across a high-temperature range of interest [37]. Such an approach, as depicted in Figure 3.1, offered studies an initial indication of temperatures where a potential phase change may have occurred at the known composition (similar in concept to a Jominy bar test for hardness testing). To identify particular phase transitions by quenching, changes in both the number and type of captured phases were observed by scrutinizing the crystallography of quenched samples through microscopy techniques such as Polarized Light Microscopy (PLM), standard optical microscopy, and petrographic imaging, while coupling the results to changes in peak strength intensity and diffraction patterns produced by X-Ray Diffraction (XRD) [40, 41]. Crystallographic changes could then be related to corresponding composition-temperature coordinates as potential phase boundary locations. In an attempt to improve the resolution of the potential phase boundary, a pair of higher resolution, isothermal quenches are described to then be performed which would strategically shoulder the proposed phase transition on both sides of the equilibria. Isothermal quenching across phase boundaries also provided the capability to perform phase identification with XRD. By performing XRD, structural information about potential phases could be proposed across quenched phase boundaries.

Furthermore, innovative thermal analysis infrastructure was also developed specifically for molten salts. A multi-sample thermal analysis reaction vessel was designed, which included live mixing capabilities and gaseous environment control. The community thus was afforded with a quantitative, yet indirect, technique for publishing deductions on phase transitions from measurements of thermal effects of heating and cooling curves. Subjecting a sample of known composition salt through a series of

heating and cooling ramps, thermocouples installed in a custom furnace allowed researchers to record the temperature profile while salt samples underwent potential phase transformations and identified when supplied heat from the furnace transitioned between sensible and latent states [37]. Figure 3.2 illustrates the innovative thermal analysis technique which offered early studies a repeatable and much more quantifiable approach to compliment the collection of quench analysis techniques.

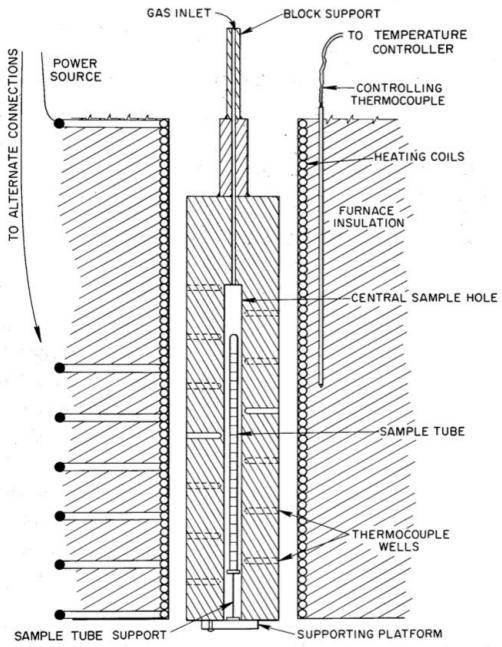

Figure 3.1. The early thermal gradient quenching furnace developed by ORNL for phase equilibria studies on molten salt [37].

Lastly, early research also reports using high temperature filters for *in-situ* solid-liquid phase investigation [39]. Equilibrating a particular composition of salt within a suspected two phase region, fritted glass or nickel filters were used to separate solid phase fractions from quantities of a liquid phase in-situ. By performing phase separation at equilibrium conditions, coupling filtration with quenching and thermal analysis not only provided an additional approach to measuring phase fractions and phase equilibria, but sensitivities of the other techniques to non-equilibrium condi-

tions (such as quenching) could be understood.

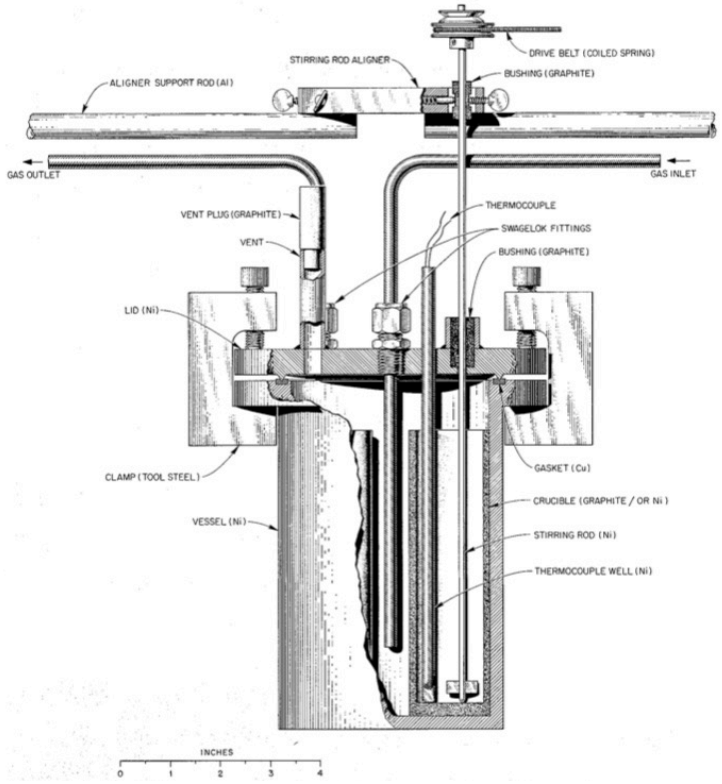

Figure 3.2. The early thermal analysis infrastructure developed by ORNL for phase equilibria studies on molten salt [37].

However, a portion of early literature also acknowledged that such techniques were not only limited by their technological capabilities, but inconsistent in their findings. Thoma *et al.* reported, for example, that the assumption of pre-measurement thermal equilibration consistently hindered the confidence in reporting thermal analysis data [42]. Furthermore, effects from supercooling remained unquantified in thermal analysis of cooling curves and were shown by Janz *et al.* to be non-trivial [43]. It was significantly more common for reports in the literature to also discount other auxiliary cooling and heating curve techniques, such as Differential Thermal Analysis (DTA), as they proved even less accurate and less sensitive [40, 44].

Techniques based on quenching were also technically subject to inaccuracy by the attempt to force equilibrium states to a non-equilibrium environment. Although an interest in equilibrium phase identification was addressed with high temperature XRD and *in-situ* filtering, literature suggests that other investigators did not follow suit [39, 40]. Dependant on the resolution of the temperature range between quenched shoulders, techniques reliant on quenched samples were also subject to obvious inaccuracies. For instance, solid phase transitions were reported to be identified more precisely by quenching techniques, while liquidus surfaces were claimed to be captured by thermal analyses with higher precision [41, 44]. Although uncertainty analysis was performed on each technique, many works published phase diagrams deduced from varying techniques with differing errors. It was also noted that quenching techniques were resorted to when small energy phase transitions could not be resolved by DTA [44]. With BeF_2 containing systems for example, disparities have since been discovered on results between a number of similar studies which had used similar techniques [45]. Additionally, when the experimental suite of techniques had been scrutinized by modern studies using the older data, a disagreement between early results from complimentary techniques has been found [46]. One of the most restrictive traits of early thermal analysis techniques was the inability to measure energy related parameters by thermal analysis or DTA. If such studies were the only source of empirical measurement, modern modelling efforts would not only be limited to a small quantity of low resolution, low confidence quantitative data, but properties such as enthalpies of phase transitions and mixing may not be considered in generating and verifying thermodynamic models.

After the MSBR program at ORNL ended, a lack of published literature suggests that justification for research related to thermodynamics of molten salts was partially stymied. During that time however, Differential Scanning Calorimetry (DSC) was maturing as a technique with higher precision and an ability to perform measurements based on energy as compared to the temperature based thermal analysis

employed earlier. Sporadically published literature shows evidence of this, where, in 1984, Rogers *et al.* published the first use of DSC in molten salt thermodynamics studies [43, 47]. Additionally, calorimetric analysis was also developing to provide thermodynamic measurements on molten salt mixtures beyond the location of phase transitions.

Marking a change in interests beyond phase equilibria studies, the development of modern techniques afforded newer studies with the ability to measure properties such as heat capacities, enthalpies of fusion, and enthalpies of mixing which could be used to experimentally inform thermodynamic model development [46, 48–53, 53]. Where molten salt electrolysis for rare-earth processing drove interest in lanthanoid fluoride solutions, MSR research now also benefitted: the systems applicable to metal processing were the same expected fission product systems generated in MSR fuel solvent compositions.

Around 2000, Pelton *et al.* began publishing molten salt thermodynamic predictions made from the modified quasi-chemical model, while the US Department of Energy led the GIF to establish a renewed interest in developing the MSR concept [54–56]. Demonstrating an ability to capture the short-range ordering complexities of molten salt, new modelling capabilities afforded the community with a more flexible approach to generate phase diagrams of molten salt. No longer were phase diagrams only generated by inferences on phase boundary locations, but measurements of thermodynamic properties could act as input into models which could construct more realistic phase diagrams. Inconsistencies were also being identified between measurements from DTA and thermal analysis with those made from drop calorimetry and DSC. Consequently, researchers started providing the community with a renewed source of modernized thermodynamics research on molten salt solutions [46, 57–59].

A renewed interest began with literature publishing improvements to phase dia-

grams after considering original phase equilibria measurements in modern thermodynamic models [26, 27, 45, 60–62]. Demonstrating an improved capability to generate phase diagrams from experimental measurements, and with a maturing interest in understanding more realistic compositions, the community was faced with a need for not only higher resolution and higher confidence in thermodynamic data, but also with an interest in obtaining data on additional molten salt systems [22,28,29,63–65].

A significant improvement in modern research has been the availability of commercial measurement systems. As discussed, early research was highly dependant on customized quench and thermal analysis techniques which resulted in a questionable ability to draw replicable and quantitative conclusions [37, 38]. Within the present literature however, the Joint Research Council of the European Union has been at the forefront of international research for developing capabilities in experimental thermodynamics measurements on MSR fuel which are founded on a number of commercially available modern techniques. With innovative experimental infrastructure for DSC, drop calorimetry, and mixing enthalpy measurements, a majority of modern experimental practises and routines reported in literature benefit from the work by Beneš *et al.* [28, 66]. A custom designed crucible for DSC of MSR salts is shown in Figure 3.3 for instance, which has not only been qualified against a known salt system, but consequently has also been employed by a number of other researchers [29, 66].

Similar to early work in the 1960's, most modern research is also founded on a complimentary suite of experimental techniques. Phase equilibria bounds are still deduced from measurements of thermal analysis and phase identification is obtained by crystallographic characterizations, such as XRD. Employing DSC for thermal analyses however, modern studies are also able to improve or make new measurements on phase transition boundaries such as solidus surfaces, liquidus surfaces, and invariant points, along with energy based properties such as enthalpies of mixing and melting and heat capacity. There are also a number of techniques that are not commonly

reported on in modern literature such as microscopy and thermal gradient analysis. Not only are different measurement techniques available to modern studies, but with advancements in modelling techniques, modern investigations are afforded the opportunity to consider thermodynamic properties in the generation of phase diagrams, something early studies could not. As such, experimental infrastructure has instead been developed to exploit techniques such as Knudsen Effusion Mass Spectrometry (KEMS) and drop calorimetry for the inclusion of thermochemical activity measurements and heat capacities into phase diagram prediction [28,67,68]. Table 3.1 depicts a summary of the experimental techniques commonly reported by studies on the thermodynamics of molten salt solutions.

Figure 3.3. Beneš' innovative DSC crucible design for phase equilibria studies on molten salt [28, 66].

Despite modern literature demonstrating improvements to early experimental investigations, there are still a number of considerations that have not been thoroughly reported on in literature. For instance, published understanding of the influence of

Table 3.1. A summary of experimental practises used by individual campaigns on the construction of salt phase diagrams.

Techniques	Reference
Thermal analysis, XRD*, visual observation, optical microscopy*, DTA	[69]
DTA, XRD*, petrographic microscopy*	[42]
Thermal analysis, XRD*, in-situ phase filtering, PLM*	[39]
DTA, XRD, & petrographic microscopy	[41]
DTA, XRD*, petrographic microscopy†, PLM†	[40]
DTA, drop calorimetry	[46]
DSC	[43]
DSC, XRD†, drop calorimetry	[28]
DSC, TGA	[67]
DTA, DSC‡	[70]
DSC, XRD†, KEMS	[68]
DSC, XRD†, KEMS, drop calorimetry	[29]
DSC, calorimetry, e.m.f[a]	[71]

* Thermal gradient quenching & shoulder quenching.
† Room temperature, no quench.
‡ DTA for phase boundaries, and DSC for heat capacity.
[a] ElectroMotive Force for determining Gibbs energy of formation.

a majority of experimental parameters and the sensitivity of measurements on such parameters is incomplete. Within the international community, modern reporting of reproducible experimental practises is also rare, where inconsistencies are found between experimental practises reported in literature. For instance, a review by the National Institute of Standards and Technologies in 2005 concluded that comprehensive uncertainty analyses in experimental thermodynamics research was found to be rare [72]. With relation to the Guide to the Expression of Uncertainty in Measurement, the uncertainty in early measurements on molten salts in particular may fall within ranking 2, device specification, without its use of statistical replication or uncertainty quantification beyond a propagation of errors [73]. With modern literature's qualification against known phase diagrams, uncertainty analyses has improved to a possible rank 4 in some instances thanks to the type-B evaluations [66, 72]. However, a majority of published phase diagrams are without statistical uncertainty reflected in their phase boundaries [27, 34, 41, 65, 74–76]. Lastly, by evaluating repeated thermograms within the same measurement, most published analyses of measurement

variance are also reported as only within-group [42, 43].

3.1.1 Material Purity

From the earliest recordings to the most sophisticated techniques of modern studies, experimental thermodynamic techniques have been challenged by the intransigent nature of molten salts to degrade in purity at high temperatures [29, 37]. Thermodynamic measurements are of particular relevance, as deductions on the behaviour of such systems are inherently related to finite composition coordinates in phase diagrams. Unfortunately, early and modern literature consistently report experimental challenges introduced by the behaviour of molten fluoride and chloride salts. As summarized by one of the earliest innovators of experimental molten salt thermodynamics, molten halides possess a number of experimentally challenging properties, such as being highly hygroscopic, hydrolyzable, and chemically reactive [37]. As a result, literature on molten salt thermodynamics reflects the findings of the National Institute of Standards and Technologies, where a lack of uncertainty analyses published in experimental thermodynamics particularly originates from an incomplete understanding of the influence of sample purity on measurement uncertainty [72].

An immediate attention for compositional accuracy has been the purity of single components before being used in fabricating specific salt mixtures. To examine component purity, early work established that material properties such as a material's melting point, crystallographic structure, and density could be taken as indications of component purity. By coupling thermal analysis, XRD, spectroscopy methods, and gravimetry, early works were afforded an indirect assessment of material purity after correlating measured values with standard reference data [36, 42, 69].

Owing to experimental experience, one of the most common indications of a ma-

terial's purity adopted by modern literature is melting point verification. Secondly, modern techniques have also maintained an interest in determining a material's purity by employing XRD for crystal structure comparison to reference standards. However, consideration of each technique's limitations should be made. For example, melting point measurements are susceptible to type I errors when reporting acceptable levels as an insight into a material's purity (the rejection of a true null hypothesis, as a result of indirectly inferring purity from a property such as melting point). With melting point, there is an inherent inaccuracy in reporting a single deduction on a material's purity when competing effects from multiple contaminants could be present. Furthermore, XRD patterns are a product of bulk material measurements, where interpretations of a material's purity are only relevant for quantities and types of contaminants which influence the material's crystal structure at detectable limits. As a result, modern campaigns also commonly report a multi-technique approach in an attempt to improve the confidence in reported material compositions. Some recent experimental campaigns have since also expanded to include direct composition analyses such as Inductively Coupled Plasma-Optical Emission Spectrometry (ICP-OES), Inductively Coupled Plasma-Mass Spectrometry (ICP-MS), or ion exchange for trace impurity analysis [43, 52, 68, 71, 77]. Employing such techniques afford modern studies with an ability to perform direct and highly sensitive measurements on the composition of salt quantities, something unobtainable in past research. By proposing that contaminant species (*nucleation impurities*) act as nucleation sites, Rogers *et al.* also uniquely suggest that the effect of supercooling may be taken as a metric for purity [43].

Not only have studies employed a myriad of techniques to quantify the purity of salt components, but research has also allocated efforts to improving the purity of materials beyond their as-received state. Early efforts to improve the purity of oxidized materials report employing an *in-situ* reaction with NH_4HF_2, an approach first introduced by Wani *et al.*. Such a technique afforded early work with a source of fluorination directly inside the quenching or thermal analyses measurement cru-

cible [37, 52, 78]. The same technique is also reported by modern literature, however only applied to actinoid materials as only they exhibit oxide impurity in modern as-received states [29]. Some modern fluorination with NH_4HF_2 also differs from early works, where the reaction is reportedly performed pre-measurement in bulk quantity [67, 79, 80]. Other reported research has also published use of direct hydrofluorination instead, where materials are purged with $HF_{(g)}$ [39, 41].

However, it is also clear that reports on molten salt thermodynamics which have used NH_4HF_2 as a material purification method are incomplete. Although NH_4HF_2 fluorination has been successfully demonstrated to improve XRD and melting point behaviour, inconsistencies are reported between practises employed in thermodynamic studies and those considered by dedicated studies on NH_4HF_2 fluorination [29, 78]. A report on ThF_4 fluorination by Che *et al.* for example concludes that immediate heating of NH_4HF_2 may in fact introduce additional impurities like $ThOF_2$, however this practise is commonly reported by molten salt thermodynamic investigations [29, 81]. By employing XRD as an indication of purity, dedicated research on NH_4HF_2 fluorination has since reported an optimized procedure for actinoid fluoride synthesis which includes a delayed heating sequence using 1:5.5 molar ratio of ThF_4:NH_4HF_2, neither of which are reflected in thermodynamic literature [81].

The extreme hygroscopic nature of fluoride salts has also required most studies to report additional dehydration techniques. However, as is evident in Figure 3.4, a wide range of dehydration practises have been published without clear justification. Work has also been conducted on different purification methods, such as fusion/crystallization, filtering, and pre-electrolysis, which demonstrates that the handling required with additional purification processes in fact introduces the possibility of nucleation impurities [43]. Table 3.2 summarizes the common techniques employed by studies to control and understand the extent of contamination of such reactive fluoride salts.

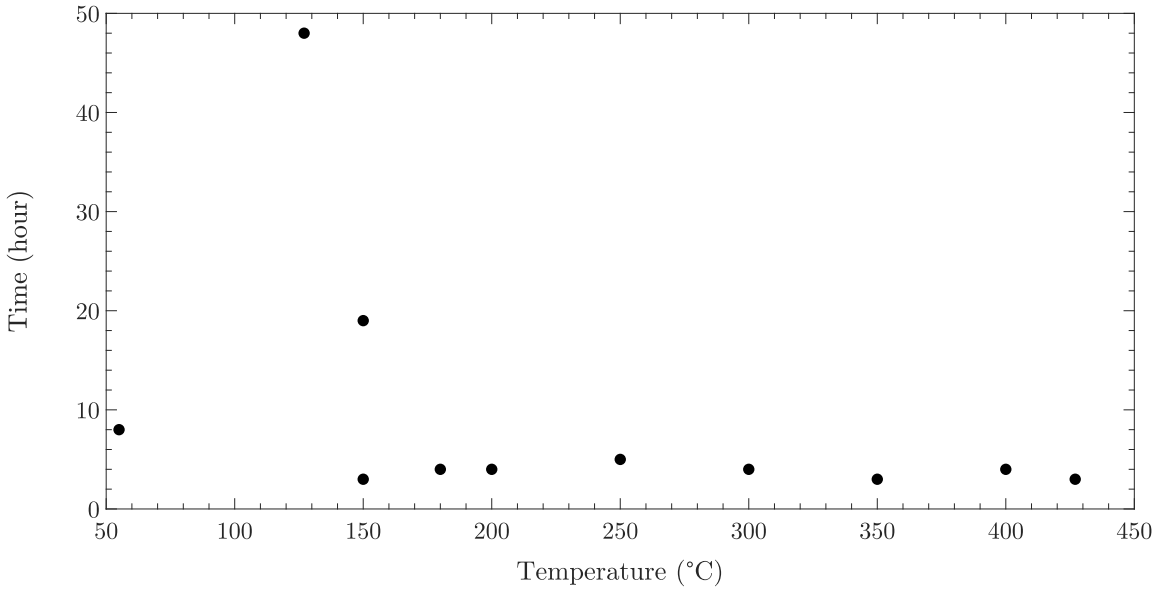

Figure 3.4. An overview of temperatures and times used for the dehydration of salt materials by individual studies. Each data point is an individual study's reported dehydration parameters. [28, 29, 46, 64, 67, 68, 80, 82–85].

Beyond purification improvements made to the materials, the maintenance of purity has also been common practise in most thermodynamic work by utilizing an atmosphere controlled glovebox, Figure 3.5. By providing an anhydrous and oxide free environment while processing materials and sealing measurement crucibles, the extreme hygroscopic nature of molten salt materials has been managed the same way in almost any study.

Table 3.2. A summary of purification practises reported in literature studying salt materials related to the MSR.

Techniques	Details	Composition analysis	Reference
Fluorination	600 °C for 3-5 hrs passing $HF_{(g)}$	Gravimetry, spectrography, & T_m	[36]
Drying	110 °C for 24 hrs	"	[36]
Fluorination	$HF_{(g)}$ or NH_4HF_2	Optical microscopy	[69]
Fluorination	120 °C with NH_4HF_2 in situ for >1 hr followed by ramp to 550 °C	Not reported	[37]
Fluorination	NH_4HF_2	XRD, microscopy, spectroscopy	[42]
Fluorination	NH_4HF_2	T_m & analytical techniques	[39]
Fluorination	$HF_{(g)}$ or NH_4HF_2	BrF_3	[41]
Fluorination	NH_4HF_2	Atomic absorption, ion exchange, & emission spectroscopy	[48]
Drying	150 °C overnight	"	[48]
Drying	180 °C slow ramp	Atomic absorption spectroscopy, & supercooling†	[43]
Purification	Fusion/crystallization, filtering, & pre-electrolysis	"	[43]
Drying	126 °C for 48 hrs	Not reported	[46]
Drying	180 °C for 4 hrs	T_m	[28]
Fluorination	250 °C with excess NH_4HF_2 for 12 hrs followed by 400 °C for 3 hrs twice	T_m, ICP-MS, & XRD	[29]
Drying	350 °C for several hrs	"	[29]
Drying	400 °C for several hours	T_m & XRD both inside glovebox	
Drying	80 °C for 8 hrs	T_m & XRD	[84]
Drying	Hotplate at 200 °C for 4 hrs followed by DSC furnace at 250 °C for 10 hrs	Not reported	[85]
Drying	277 °C	ICP-MS & XRD	[71]
Filtering	BPS catalyst, silica gel, molecular sieves, and $Mg(ClO_4)_2$	"	[71]
Fluorination	$1 : 5.5^*(ThO_2 : NH_4HF_2)$ for 5 days at T_{room} followed by 450 °C - 550 °C	XRD	[81]‡

* Molar ratio.
† The extent of supercooling was interpreted as an indication of purity.
‡ A thorough investigation dedicated to understanding the optimized ThF_4 fluorination by NH_4HF_2.

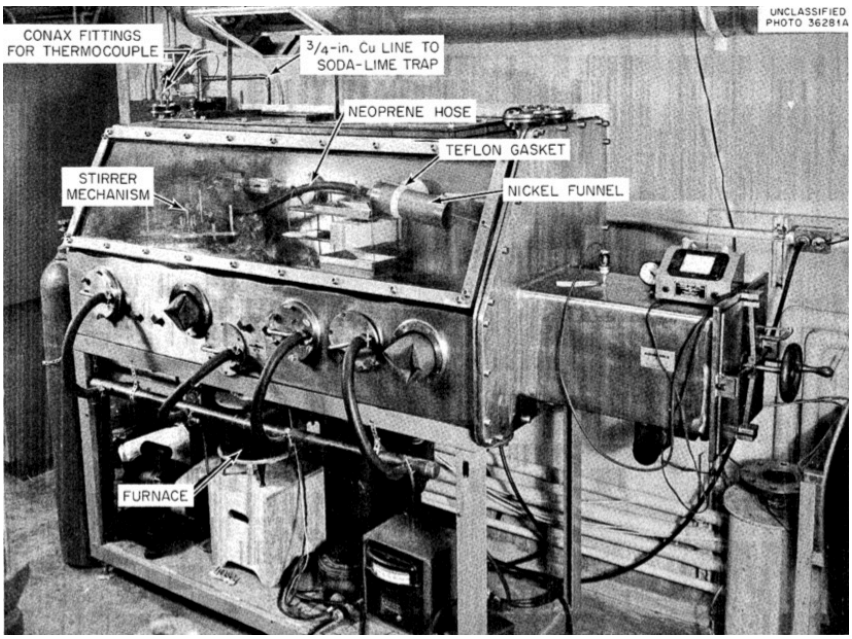

Figure 3.5. ORNL's early use of a glovebox for processing hygroscopic salt materials [37].

Lastly, mixing methods for fabricating particular compositions of interest have also been acknowledged in literature, with independent research employing both a bulk mixing approach or the Direct Mixing Method (DMM) [43, 86]. A report by Jones *et al.* explains how by reducing the handling and potential sources of external contamination, the DMM has been demonstrated to be a valuable technique in obtaining higher accuracy in thermal analyses measurements [39]. Despite the DMM providing a source of random error variance to independent measurement replicability, the DMM is the primary approach to obtaining mixtures of salt components in literature.

3.1.2 Salt Facing Materials

Due to the high temperatures in MSR applications, the purity of salt samples is also challenged during the measurement of thermodynamic properties. Innovative encapsulation devices have thus not only been developed to protect salt samples from

rehydrating or oxidizing with ambient air, but also to minimize potential wall-salt interactions during various types of experimental measurements. For example, Beneš described how the design and employment of custom crucibles specifically for DSC and drop calorimetry addressed the possibility of salt-wall interaction during measurements by using boron nitride or Ni as salt facing materials [28, 66]. Summarized in Table 3.3, the multi-disciplinary use of salt facing materials is clearly focused on highly inert materials such as graphite, boron nitride, nickel, and platinum.

Despite the sensitivity of experimental works on salt facing material selection, an understanding of the influence of different salt facing materials during measurement has not been consistently reported. Qualifications of experimental procedures (type B considerations) are the only insight into this source of error in literature. Instead, direct insights can only be made by making deductions from corrosion studies on common molten salt compositions and their behaviour with common structural materials. For example, research suggests that by using ICP-MS, ICP-OES, glow-discharge optical emission spectroscopy, and electron probe x-ray microanalysis, that graphite can exhibit corrosion and microstructure changes at high temperatures under the presence of molten fluoride salts [87]. The presence of graphite has also been found to accelerate corrosion, alloys such as Hastelloy-N and Inconel exhibit moderate corrosion, and pure nickel (such as Ni-201) is generally demonstrated as being corrosion resistant [88].

Table 3.3. A summary of salt facing materials reported in open research.

Material	Technique	Reference
Graphite or Nickel	Thermal analysis	[37]
Nickel or platinum	Quenching	[37]
Graphite	Calorimetry on LiF & NaF	[52]
Platinum	Calorimetry on KF	[52]
Nickel	Purification	[52]
Nickel	Calorimetry	[89]
Inconel	DSC	[46]
Inconel	Calorimetry on CsF and RbF	[46]
Glassy carbon	Calorimetry on LiF–LaF_3 and NaF–LaF_3	[46]
Boron nitride	DSC	[66]
Nickel	Calorimetry	[28]
Platinum-rhodium	DSC	[67]
Platinum-gold	DSC & DTA	[70]
Platinum or graphite	DSC	[63]
Graphite	Spectrophotometry	[90]
Boron nitride	DSC	[68]
Nickel	DSC	[64]
Platinum	DSC	[65]
Boron nitride	NMR	[91, 92]
Boron nitride	EXAFS	[91, 92]
Quartz	DTA	[71]
Nickel	DSC	[71]
Gold plated nickel alloy	DSC	[84]
Copper	DSC	[85]
Agate	Mixing/particle size reduction	[79, 81]
Boron nitride	NMR	[93]
Graphite	Raman spectroscopy	[94]

3.2 Experimental Phase Boundaries

Popular measurement techniques used in determination of phase diagrams exploit the latent energy of first order phase transformations. In the past, locations of phase transformations were defined by a temperature profile's first order discontinuities [95]. However small energy phase transformations are difficult to resolve by identifying changes in the slope of an experimentally measured temperature profile [95]. Instead, a modern approach is to record differential measurements of the temperature or energy difference required by a first order phase transformation as a material experiences

a phase transformation. By realizing the relation between the profile of a differential measurement and the topology of a phase diagram, signal peaks from a differential measurement can provide a more sensitive probe of phase transformations than first order slopes. Figure 3.6 illustrates how differential thermal profiles provide a clearer artifact of a phase change compared to the first order derivative of traditional temperature profiles.

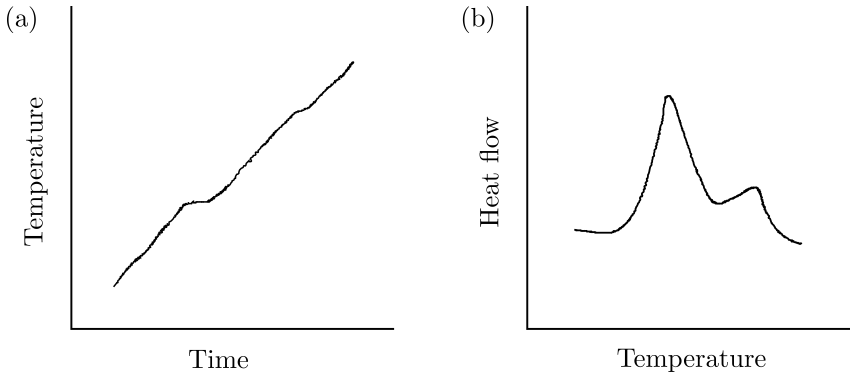

Figure 3.6. A conceptual illustration of the differences between a thermal analyses temperature profile and a differential thermogram from DTA or DSC. (a) Hypothetical temperature profile from a thermal analysis measurement.
(b) Hypothetical differential thermogram from a DSC measurement.

With any thermal analysis technique however, such deductions of thermodynamic properties are subject to inherent sources of error from the measurement made in non-equilibrium. For example, thermal lag caused by non-spontaneous heat transfer through a finite quantity of material suggests that experimental parameters (*e.g.* ramp rate and sample mass) can influence the confidence in a thermodynamic (equilibrium) result. Unlike quench techniques, reporting a phase transition from a thermogram is not a direct observation of a phase change, and is formulated on deductions made with assumptions that a phase transformation is the source of such thermogram behaviour [37]. Thus, the interpretation of thermal analyses measurements is also an important consideration.

Despite these concerns, with thoughtful experimental design, one can demonstrate a quantifiable and reproducible technique for providing high throughput and relatively inexpensive insights into the phase equilibria of salt mixtures by employing a range of thermal analyses techniques. Early literature on thermal analyses reports employing innovative crucible designs with in-situ mechanical mixing capabilities to address reducing thermal gradients and compositional inhomogeneity before materials were subject to cooling ramps [37]. In literature which did not report live mechanical mixing during melting, high temperature shaking was employed [39, 40]. By reducing the surface area of liquid salts with a floating graphite disc, early thermal analyses also reduced the evaporation of mixture components during measurements and addressed concerns of in-situ composition drift [37].

Modern thermal analyses also employ strategic infrastructure and techniques for reducing the extent of uncertainty in reported measurements. Commonly reported in modern literature is the calibration of thermal analyses measurements against known equilibria properties. By measuring phase equilibria bounds such as melting points, modern literature demonstrates type-B qualification by accounting for systematic errors such as ramp rate, material-wall wetting behaviour, and crucible design [28]. The differential techniques of modern efforts are naturally resistant to random errors themselves. By measuring differential phenomena between a reference crucible and a sample crucible, random errors occurring during a measurement are effectively blocked out. Modern research is also afforded with published American Society for Testing and Materials (ASTM) standards [96–98] on topics such as calibration and measurement interpretation, along with commercial recommendations from device vendors who fabricated the modern thermal analyses technologies [99]. Modern calibration practises reported by research from the European Commission are even more encompassing across a number of phenomena such as ramp rate [28]. Early works notably do not report calibration efforts in conclusions drawn from thermal analyses, but instead report a single qualification of the experimental device with the NaCl – KCl system [37].

Despite novel work by the European Commission demonstrating a modern calibration procedure for DSC, inconsistent calibration practises are still evident between international efforts [67, 70, 71, 82, 84]. One aspect of calibration that is of particular significance is the relation between calibrant materials and crucible materials. Table 3.4 summarizes the reported calibrant materials employed in phase boundary determination and the respective materials holding the calibrant during calibration. Of particular note is the possible inaccuracy of studies employing metallic calibration materials with metallic calibrants. With the potential for alloying solutions of calibrant and crucible material, inappropriate adjustments to the accuracy of published data from such studies may exist [67]. Furthermore, an intermittent interest in modern literature is made to employ calibrant salt materials which reflect the wetting behaviour of molten fluoride salts.

Another important aspect in quantitative thermal analysis is the manner in which measurements are interpreted. For systems such as stoichiometric compositions, pure end-members, eutectics, or peritectics, the Gibbs phase rule explains how first order phase transformations hold zero degrees of freedom in X-T space, and likewise can be defined by a standard, reproducible artifact of a thermogram. Equation 3.1 illustrates the Gibbs phase rule for an isobaric system, which demonstrates the freedom (or lack thereof) of invariant equilibrium of a single component system (F representing the degrees of freedom, C being the number of components, and P being the number of phases in equilibria where, *i.e.*, where $C = 1$ and $P = 2$ for the solid and liquid phases). A melting point of a pure species, for example, is consistently referred to in literature as the onset of a heating thermogram [82]. In general, literature is in agreement with the ASTM standard, where invariant points can be deduced from the onset of a heating peak [98].

$$\begin{aligned} F &= C - P + 1 \\ &= 1 - 2 + 1 \\ &= 0 \end{aligned} \tag{3.1}$$

The deduction of multi-component phase transformations is however non-trivial. Instead of point phenomena, first order phase transformations of such systems withhold compositional degrees of freedom and therefore can demonstrate ranges of temperatures that phase equilibria exist, shown isobarically in Equation 3.2 (in this case $C = 2$ and $P = 2$). Phase diagrams in such a system are thus defined by onset and endset phase boundaries, such as the liquidus and solidus of melting. With thermal analyses' sensitivity to transient thermal phenomena, such an environment is complicated when interpreting definitive traits of a thermogram for thermodynamic measurements [98].

$$\begin{aligned} F &= C - P + 1 \\ &= 2 - 2 + 1 \\ &= 1 \end{aligned} \tag{3.2}$$

Across the literature, many interpretations of non-invariant thermogram artifacts are reported. In melting phenomena for example, some define the endset of single heating curves to represent the liquidus, whereas others define the onsets of cooling curves and heating curves to be the liquidus and solidus respectively [28,70,82]. Using the latter interpretation, studies have assumed that negligible effects of supercooling have been experienced, comparing the onset and endset positions of heating curves with the endset and onsets of cooling curves respectively. Interestingly, such behaviour is opposite to findings by Rogers *et al.*, which suggest that supercooling itself may

be used as an indication for purity (*i.e.* impurities act as nucleation sites) [43]. By interpreting the peak of a differential curve as the point at which latent energy is no longer present, literature generally interprets the peak of a heating curve to be the liquidus (implying that the non-infinite slope following the peak is purely an artifact of thermal lag) [83, 100]. There is also theory in literature which suggests that with slow enough ramp rates, individual solidus and liquidus curves should diverge, where the liquidus can be identified by a predominant tale, as was shown in Figure 3.6 (b) [100].

There are other uncertainty considerations published by studies on molten salt thermal analyses as well. For example, some approaches employ pre-treatment thermal cycling before recording meaningful thermograms. An understanding on the effect of supercooling, volatile species' evaporation on mixture compositions, and homogenization/mixing are all direct benefits of studies employing pre-measurement ramps. In one study in particular, Khoklov *et al.* investigated the converging behaviour of sequential heating ramps and suggested that confidence measurements could be taken from the fourth or fifth sequential thermograms [67].

One area of little discussion in literature are details and uncertainty of mixing compositions. The DMM is described by a majority of literature, however only Rogers *et al.* discussed a quantitative assessment of the influence of mixing procedures [43, 83]. For example, no report has been made on either the benefit of bulk mixing for replicability of independent measurements or the effect of particle size on mixing error [79]. There is also no report of enthalpy plotting with Tammann diagrams, which literature suggests is a more accurate method for identifying eutectic compositions and maximum solubilities (eutectic endpoints) for a phase diagram [95, 100].

Table 3.4. A summary of calibration materials reported in literature for thermal analysis for phase boundary determination.

Calibrant	Technique	Crucible material	Reference
KCl & NaCl	Thermal analysis	Graphite or Nickel	[37]*
In, Sn, Pb, KNO_3, LiCl−$KCl_{(eut.)}$	DSC	Not reported	[43]
CsCl, $BaCO_3$, AG_2SO_4, $CKlO_4$, NaCl, KCl, In, Sn, Bi	DSC	Boron nitride	[82]
Sn, Pb, Zn, Al, Ag, Au	DSC	Boron nitride	[28]
$RbNO_3$, $KClO_4$, Ag_2SO_4, CsCl, K_2CrO_4, $BaCO_3$	DSC	Platinum-rhodium	[67]
Zn, Au, In, Ni, $BaCO_3$	DSC	Platinum-gold	[70]
In, Al, Au, Pb, Cu, Zr, Ag, Sn	DSC	Boron nitride	[68]
Al, Ag, Au, Ni, Sn	DSC	Platinum	[65]
$BaNO_3$, NaCl, $K_2Cr_2O_7$, Ca_2O_4	DSC	Quartz	[71]
$C_{10}H_{16}$, In, Sn, Bi, CeCl	DSC	Ni−Cr alloy	[101]

* Not a calibration, but instead was an uncertainty qualification for further studies.

3.3 Solvent Salt Systems

With the working fluid in an MSR simultaneously serving as primary circuit coolant and solvent for fissile fuel, the design criteria of such a fluid is clearly multi-faceted. As suggested in literature, working fluid composition may have an imperative influence on the safety, operation, design, efficiency, and the economics of an MSR [29, 102]. The working fluid of choice in an MSR is also an important factor in the design and research activity of a reactor depending on what function the reactor intends to serve. With composition influencing subjects such as neutronics, thermal hydraulics, thermodynamics, transport properties, corrosion, and chemistry, reactor designs for breeding, burning, or generating electricity may converge to different compositions of working fluid. With the infancy stage of the NFMG's experience in the MSR thermochemistry domain, establishing a baseline literature review on salt solution compositions is valuable to identify the most applicable and beneficial compositions to be studied. As such, an intent of this literature review is not only to establish motivation for the thesis itself, but also to establish a common background for future MSR research.

One working function of the fuel solution in an MSR is its role as a primary coolant for the fission heat. Along with Sabharwall *et al.* [103], Saltarella [104] references Boyd and Taylor [105] in outlining universal properties which a primary coolant fluid should possess: (a) high boiling point, (b) low vapour pressure, (c) high specific heat, (d) high thermal conductivity, and (e) a high density at low pressure [59]. Serrano-López *et al.* [106] further specify that to avoid freezing, primary coolant must exhibit a melting point below the minimum temperature in the fluid's circuit, while also exhibiting a large change in specific volume with temperature to offer natural circulation in the event of pump failure [106]. As such, numerous authors, including LeBlanc *et al.* [23] and Serrano-López *et al.* [106], identify that not only do molten salts meet these conditions advantageously, but Capelli specifies that fluoride salts in

particular best fulfill these targets [19, 103]. It is in addition to a lack of development in other salt forms such as chlorides, that the focus of this thesis will be on fluoride salt systems.

Beneš *et al.* [19, 107], Serp *et al.* [17], and Briant *et al.* [108] specify that further physico-chemical properties of a working fluid in a MSR may be desired beyond their use as primary heat transfer fluids, as they also function as solvent for fissile fuel [106, 109]. In the company of Serrano-López *et al.*, these authors explain that neutronic properties such as a small neutron capture cross section, chemical and thermal properties such as chemical stability, high actinoid solubility, irradiation stability, structural material compatibility, along with transport properties are important factors for consideration in the choice of nuclear fuel carrier salt [17, 19, 31, 103, 106, 108]. At ORNL, Grimes developed a molten salt selection process which concluded that no single fluoride could reasonably act as a solvent, but instead, a solution of fluoride compounds would be necessary to achieve a depressed melting point [110, 111].

Concerned with developing MSR salts for the thermal spectrum, Grimes identified that fluorides of beryllium (BeF_2) and lithium (^7LiF) were the most promising salt solution components able to support the delicate neutron economy of a thermal breeder MSR [110–112]. Haubenreich explains how this argument was the leveraging point for the selection of $^7LiF-BeF_2$ (FLiBe) as the primary working fluid in the MSRE and MSBR at ORNL and continues to be a base component of a number of modern MSRs [19, 112].

However, considering the interests of a modern energy landscape, Serrano-López *et al.* also identify that the criteria for an acceptable working fluid are changing. In part, thanks to experience gained with the MSRE and MSBR, particular attention to the working fluid's potential toxicity, economics, and compatibility with structural materials is maturing [106, 113]. Specifically, Serrano-López *et al.* outline a main

threat to the deployment of an outdated MSR design: the highly toxic Be working fluids and the burden that comes with their management. However, with changing interests from the 1960's thermal breeding spectrum, modern opportunities for developing fast spectrum breeding reactors, TRU burners, or thermal spectrum electricity generators are inspiring a number of research endeavours to focus on the replacement of Be containing salts. Such modern interests may consider alternative melting point depressors beyond BeF_2, such as sodium fluoride (NaF), zirconium fluoride (ZrF_4), potassium fluoride (KF), and rubidium fluoride (RbF) [110,111]. Along with the cost of processing to obtain a neutronically acceptable isotope of Li (^{7}Li), tritium retention exhibited by Li is also driving interest in alternative alkali fuel solvents such as NaF [106, 114]. Reflecting a number of these arguments is Table 3.5, which summarizes the base fluoride salt solutions identified by the designers of commercial and research MSRs.

Table 3.5. A summary of fluoride molten salts reported by commercial and research MSRs.

Designator	Temperature (°C)	Neutron spectrum	Typical base composition	References
ARE	860	Thermal	$0.50\,NaF - 0.46\,ZrF_4 - 0.04\,UF_4$	[112, 115, 116]
MSRE	635-663	Thermal	$0.65\,LiF - 0.291\,BeF_2 - 0.05\,ZrF_4 - 0.09\,UF_4$	[112, 117]
MSBR	565-704	Thermal	$0.717\,LiF - 0.16\,BeF_4 - 0.12\,ThF_4 - 0.03\,UF_4$	[117–119]
MSBE	565-704	Thermal	$0.715\,LiF - 0.16\,BeF_2 - 0.12\,ThF_4 - 0.5\,UF_4$	[19, 117]
MSFR	630-650	Fast	$0.78\,LiF - 0.176\,ThF_4 - 0.04\,UF_4 - 0.02\,(Pu - An)F_3$	[31, 118, 120, 121]
	Not reported	Fast	$0.78\,LiF - 0.16\,ThF_4 - 0.06\,UF_4$	[31, 118, 122]
MOSART	600-715	Fast	$0.15\,LiF - 0.58\,NaF - 0.27\,BeF_3 - 0.013\,(Pu - An)F_3$	[28, 123, 124]
TMSR	600-700	Thermal & fast	$LiF - BeF_2 - ThF_4 - UF_4$	[107, 125]
MSR-FUJI	565-704	Thermal	$0.7176\,LiF - 0.16\,BeF_2 - 0.12\,ThF_4 - 0.0024\,UF_4$	[107, 126, 127]
CMSR	Not reported	Thermal	$NaF - KF - UF_4$	[128]
Copenhagen*	700	Thermal	$LiF - ThF_4$	[129]
THORCON	540-704	Thermal	$0.76\,NaF - 0.12\,BeF_2 - 0.095\,ThF_4 - 0.025\,UF_4$	[130]
LFTR	500-650	Thermal	$LiF - BeF_2 - ThF_4 - UF_4$	[131]
IMSBR	800	Fast	$LiF - BeF_2 - ThF_4 - UF_4$	[132]
IMSR	625-700	Thermal	$NaF - UF_4 - ZrF_4$†	[133]
SSR-W	550-700	Fast	$0.10\,NaF - 0.48\,KF - 0.42\,ZrF_4$‡	[134]
SSR-U	550-700	Thermal	$0.33\,NaF - 0.30\,RbF - 0.37\,UF_4$	[134, 135]
SSR-Th	650-750	Thermal	$NaF - ThF_4$[a]	[134]

* Copenhagen Atomics.
† Conjecture.
‡ Chloride salt fuelled.
[a] Coolant blanket

3.4 Operational Molten Salt Compositions

Beyond the base salt systems for an MSR system, such compositions are only realistic before operation of the reactor. With operation comes an immediate addition of species such as those from fission, corrosion, and activation. A common trend is evident in early works however, where compositions of interest focused on salt constituents that could act as solvent components. Relatively little has been reported on the fission products, activation products, corrosion products, or redox control additives in high resolution. For example, although consideration of lanthanoid containing systems was presented by Thoma *et al.*, data used to generate published phase diagrams is not only of low resolution and non-replicated, and is also populated in compositions far too saturated with the fission products to be applicable to reactor burn-up conditions [44].

The challenge with developing an understanding of realistic compositions of operational molten salt systems is the high degree of complexity with such a large number of possible constituents from fission, corrosion, activation etc. One approach reported throughout literature is to simplify the high number of combinations of salt components by grouping such components into groups which are predicted to exhibit similar behaviour in an MSR environment. Such a technique is common in conventional solid fuel research as well, where fission products are grouped into categories to aid in their general understanding [24]. For instance, LeBlanc *et al.* suppose that the fission products within an MSR are either soluble within the molten salt or are insoluble and may be removed with online processing [23]. There also exists reports of generalizing species such as the noble gases or noble metals which are quoted as insoluble in common molten salt solutions [23]. Thoma *et al.* for example have published results on the lanthanoid fluoride systems, where the phase diagrams exhibit similar simple eutectic system behaviour [27]. Examples of such classifications are illustrated in Tables 3.6 and 3.7.

Table 3.6. Categorization of elements according to their expected solubility in fluoride salt [19, 136].

Category	Element
Gases	Xe and Kr
Stable & soluble fluorides	Rb, Sr, Y, Zr, Cs, Ba, La, Ce, and REE
Insoluble (noble) metals	Nb, Mo, Tc, Ru, Rh, Pd, Sb, Ag, and Te

Table 3.7. Categorization of elements according to the periodic table [114, 137, 139].

Category	Element	Note
Noble gases	Xe and Kr	Assumed to be removed by helium sparging [114].
Lanthanoids	Ce, Nd, Eu, Sm, Sc, Y, La, Pr Pm, Er, Dy, Gd, Er, Tm, Yb, and Lu	Less well studied but tolerable in solution [137].
Noble metals	Mo, Ru, Pd, Tc, Rh, Zn, Gd, Ge As, Nb, Cd, In, and Sn	Insolubility consensus [114, 124, 138–141].
Actinoids	Pu, Am, Cm, and Np	Solubility important for burner [138].
Alkali-metal halides	Br, At, Na, K, Rb, Cs, and I	Actinide solubility improvers [139].

Another technique is to identify the importance of particular classes of species with respect to one another. In such an approach, many considerations could be made such as neutronic influence, thermodynamic influence (melting point, solubility, etc.), their capability to be removed from molten salt solutions, and their predicted quantity within the fuel salt system. As an initial screening, Fitzpatrick [142] provided a burn-up calculation to predict the most probable fission products generated by the MSBR, which is illustrated in Figure 3.7.

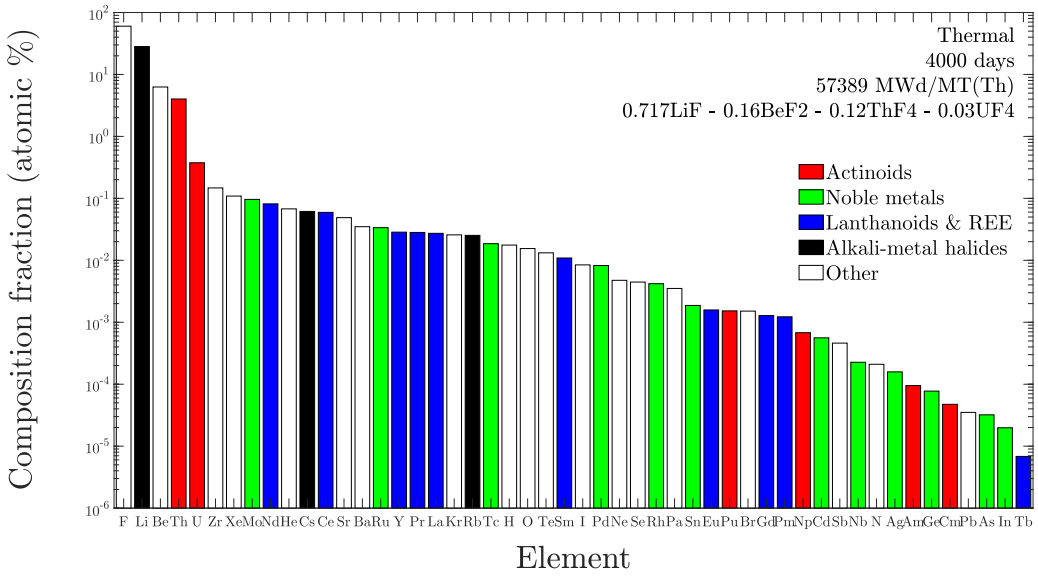

Figure 3.7. High-level prediction of molten salt composition in a thermal MSR fuelled with $0.717\,\mathrm{LiF}-0.16\,\mathrm{BeF_2}-0.12\,\mathrm{ThF_4}-0.03\,\mathrm{UF_4}$ and operated under 57389 MWd/Mt(U) for 4000 days [142].

Relative to early publishings, such as those summarized by Thoma *et al.* [26, 27], Capelli [29] exemplifies the advancement of modern activity in not only experimental and modelling techniques but also in the focus of compositions under study. Afforded by a maturing understanding of fuel solvent choice (and even optimization), modern research has begun to address the influence of species introduced into fuel solvents as a product of reactor operation. Species such as fission products, activation products, and corrosion products now make up a non-trivial fraction of the current research

activity on MSR related phase diagram construction. With the increasing complexity of a number of salt component combinations being published in open literature, a literature review has been conducted to develop a database of reported salt system compositions. Because of the size of such a collection of literature (with components covering a majority of the periodic table), a portion of the database has been summarized in Table 3.8.

Table 3.8. A summary of the binary systems considered in the literature as an example of the more extensive database which was developed. Black circles represent systems whose thermodynamic behaviour have been reported in literature.

	LiF	CsF	CsI	LiI	ThI_4	ThF_4	NaF	CaF_2	KF	RbF	BeF_2	LaF_3	ZrF_4	UF_4	CeF_3	NiF_2	PuF_3
CsF	•																
CsI	•	•															
LiI	•		•														
ThI_4			•	•													
ThF_4	•	•	•		•												
NaF	•	•				•											
CaF_2	•					•	•										
KF	•	•				•	•										
RbF	•	•					•		•								
BeF_2	•					•	•										
LaF_3	•	•					•	•	•	•							
Zr_4	•																
UF_4	•					•	•						•				
CeF_3	•					•								•			
NiF_2	•						•		•								
PuF_3	•	•				•	•		•	•	•	•		•	•		
UF_3	•						•										
MgF_2	•					•				•							

CHAPTER 4

Goals of Research

Performing an extensive literature review has given this thesis direction for developing a framework for performing thermodynamic measurements on fluoride salt materials. As part of the proposed framework, this thesis aims to develop infrastructure and experimental practises for obtaining accurate and well characterized measurements on molten salt. Standard Operating Procedures (SOPs) will be a tool in the standardization and transparency in the developed practises. In order to thoughtfully propose an experimental campaign, this thesis also intends to qualify the extent of uncertainty and the sensitivity to experimental parameters which is incomplete in current literature. The influence of aspects such as particle size, sample preparation and purification, and crucible design are to be characterized in the scope of experimental thermodynamics. Furthermore, for measurement systems outside of those developed and qualified by researchers at the European Commission, this thesis will work to design a DSC crucible for use in a NEZTSCH 449 F1 Jupiter STA.

Within the scope of the foregoing literature review, this thesis is also intended to

provide an initial roadmap for the study of particular molten salt systems. A goal of the literature review is to provide a summary outlining experimental practises and molten salt systems published in literature, and solvent salt components and fission products which have been already reported on. In this way, the NFMG may be able to efficiently focus their efforts on valuable and novel measurements in the fluoride salt space.

CHAPTER 5

The Measurement Routine and its Qualification

In campaigns studying thermodynamics of fluoride salts, literature consistently reports a series of pre-measurement techniques employed to improve the confidence in conclusions which may be drawn. Within this thesis there has therefore been developed a catalogue of infrastructure and practises which adopt a number of these considerations. The framework demonstrated by following the black arrows in Figure 5.1 illustrates the complete lifecycle of a salt eventually subject to thermodynamic measurement by DSC. Firstly, besides DSC and XRD measurements which are performed within commercial infrastructure in normal laboratory spaces, all salt handling and processing is performed within an inert atmosphere glovebox filled with Ar and actively scrubbed to maintain a working environment with $< 0.5\ ppm\ H_2O and < 0.5\ ppm\ O_2$. After procuring high purity salts (generally on the scale of 99.99%), as-received materials are first ground by hand to a reduced particle size by using a mortar and pestle. The powder is then subjected to a purification process by drying or fluorination depending on whether one expects the fluoride salt to be contaminated with an oxide impurity or not (modern literature has routinely assumed that only flu-

orides of actinoids are susceptible to significant oxidation). Purification is performed using custom infrastructure within the glovebox which has been developed to safely subject salts to treatments of high temperature and chemical reactions while minimizing sources of inadvertent sample contamination by the atmosphere or reaction vessel. Bulk quantities of purified salt quantities are then stored in double sealed High Density PolyEthylene (HDPE) containers within the glovebox until being decanted for measurement. DSC of a single salt component can be performed after filling a DSC crucible with a known quantity of purified salt, tamping the salt to the base of the crucible, and hermetically sealing the crucible while inside the glovebox. Mixtures of salt materials can be fabricated by either directly mixing and weighing fractions of components on top of a scale within the glovebox, or by mixing a bulk quantity of such a mixture to be subsequently decanted for repeat measurements. Mixed salt fractions are sealed in crucibles within the glovebox in the same approach that single component systems are, both of which are egressed from the glovebox for immediate DSC.

By introducing such practises into the DSC measurements of fluoride salts, improvements to the standardization of procedures and subsequently the replicability of measurements and accuracy of results is sought. With the development of such a routine however, qualification and understanding of the influence of each process of a thermodynamic measurement is important in both the reporting of conclusions with a quantifiable degree of certainty and in possibility for diagnosis and minimization of the inevitable sources of error. In particular, sources of compositional error have been given the most attention in both mitigation efforts and qualification routines in this thesis. Such effects cannot feasibly be calibrated out of a measurement unlike those originating from the thermodynamic measurement itself. As such, the dashed, red arrows in Figure 5.1 illustrate a qualification scheme directed at characterizing the influence of salt processing activities on material composition in addition to effects on particle size and their physical feasibility. A suite of techniques such as DSC,

XRD, ICP-MS, and ICP-OES are reported by literature to have been employed for exploiting a number of material properties of fluoride salt materials such as melting point, crystal structure, mass-charge ratio, and emission spectra for insights into their composition. Considering the available infrastructure at UOIT, Figure 5.1 illustrates how DSC and XRD have been employed as complimentary techniques for material purity qualification.

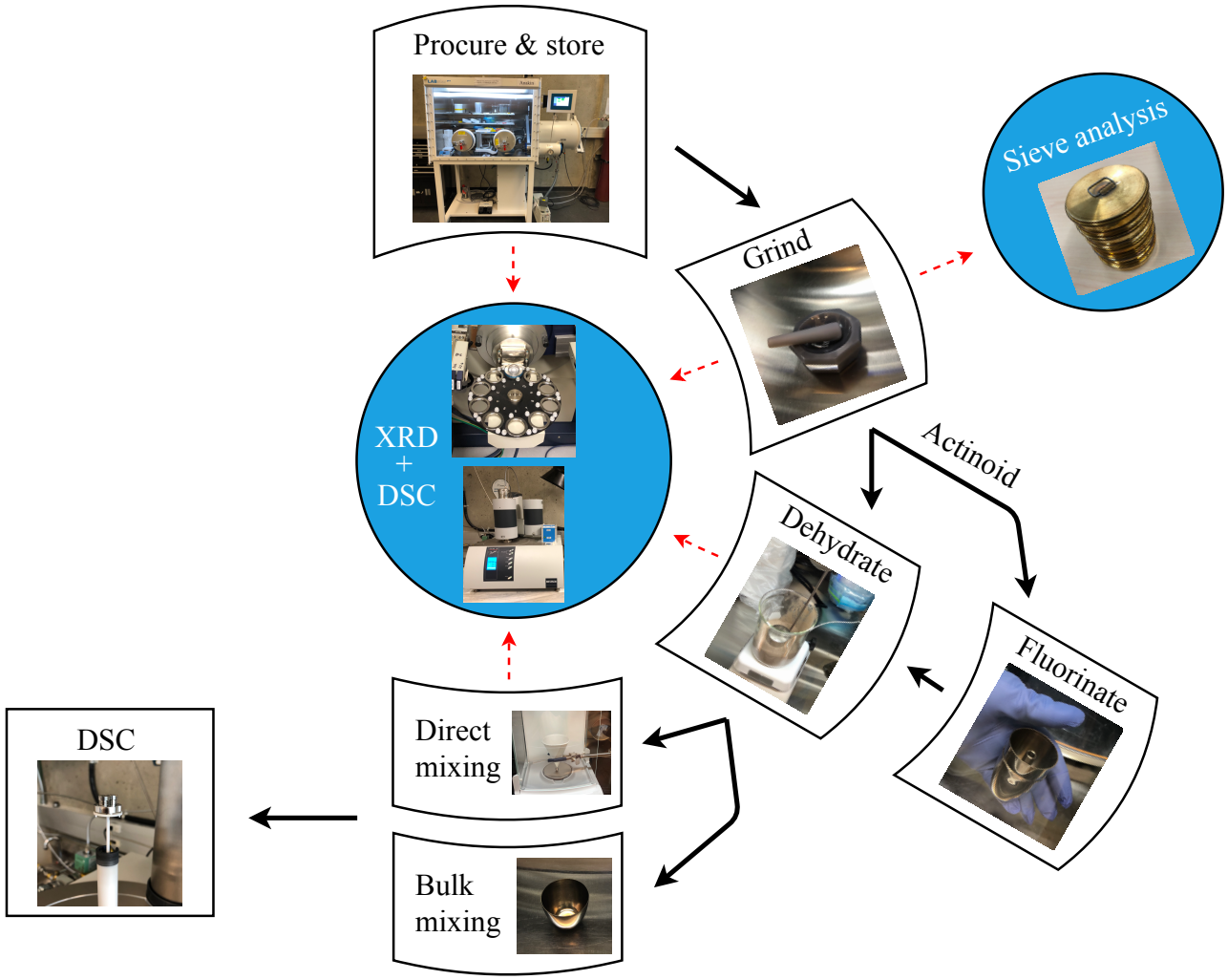

Figure 5.1. A proposed framework for regular DSC measurements (solid, black arrows) by the NFMG, overlaid with a periodic qualification plan (dashed, red arrows) for each processing technique.

5.1 Storage and Working Environment

Consistent with a majority of literature, an inert atmosphere glovebox was utilized for conducting a majority of handling and processing techniques on hygroscopic and reactive fluoride salts. Employing an inert atmosphere box is a practise reported in the earliest MSR related thermodynamic research, where in Figure 3.5 for example ORNL demonstrated their ability to purify, mix, and encapsulate salt materials all within an inert atmosphere [37]. The glovebox of the NFMG is shown in Figure 5.2, which provides with a < 0.5 *ppm* $H_2O, < 0.5$ *ppm* O_2 argon environment to work within. The glovebox is also operated under negative pressure and has been outfitted with high efficiency particulate air filters on all inlet and outlet tubing as a form of radioactivity containment. The $-2.5\,\text{bar}$ to $-4.0\,\text{bar}$ (gauge) that the glovebox operates at also provides a possible under-pressure atmosphere to anything sealed within the glovebox's environment. An implication of this is the reduction of fluoride salt vapour pressures during a high temperature DSC measurement, as Beneš *et al.* identify [28]. Such a possibility is an advantage in safety, by reducing the pressure that the crucibles may be subject to throughout a measurement.

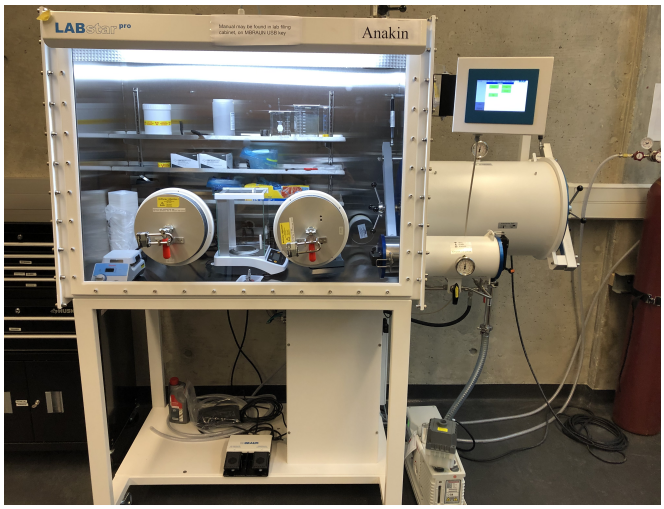

Figure 5.2. The MBRAUN glovebox used to handle, purify, and mix salt materials in an inert atmosphere of < 0.5 ppm H_2O and < 0.5 ppm O_2.

5.2 Particle Size Reduction

Within the glovebox, capabilities have been established to reduce and quantify the particle size distribution of salt materials. There are a number of implications of particle size on a thermodynamic measurement. If directly mixing salt fractions into a crucible, for example, the particle size of a salt material is an important consideration because of the relationship between a finite sample mass of a crucible and compositional accuracy. With a finite amount of total material permitted in a crucible, obtaining a highly accurate composition with respect to an intended target is inherently dependant on the smallest particle size. The precision of repeat measurements when directly mixing is also related to particle size, as replicability of individually weighed compositions have a finite resolution. In bulk mixing techniques particle size plays less of a factor, as sample quantities are effectively unbound and good replicability is easier to achieve. Additionally, particle size is also a significant factor if DSC calibration techniques employ specific salt mixture compositions as standard references, such as the eutectics suggested by Khokhlov *et al.* [67]. The influence of particle size is further accentuated if studies are conducted on simulated fuel with trace fission product fractions. A small average particle size is also important for obtaining high density compaction of salt materials pre-measurement, a practise proposed to reduce the transient parameters of a measurement. In literature discussing the synthesis of fluoride actinoids from actinoid oxides, particle size has also been reported to play an important role in reaction times [78, 143, 144]. Yet, particle size quantification is unreported in open literature on molten salt thermodynamics.

As per common practise, an agate mortar and pestle was implemented within the glovebox, along with a sieve stack of 63, 150, 250, and 850 µm in accordance with ASTM standard B214-16 [79, 145]. The mortar, pestle, and sieves are depicted in Figure 5.3 and associated SOPs founded on ASTM standard B214-16 [145] are given in Appendix A.2 and A.1.

(a)  (b) 

Figure 5.3. (a) The agate mortar and pestle used to reduce particle size of as-received salt materials. (b) The sieve stack for determining particle size distribution within the glovebox according to ASTM B214-16.

5.3 Purification

Beyond reducing the particle size, the literature standard after procuring salt materials is to conduct a form of purification. As a result of the hygroscopic nature of most fluoride salts, and the oxidative nature of actinoid salts, numerous reports in literature demonstrate the importance of purifying as-received materials beyond their quoted as-received purity [28, 29, 39, 84].

The purification of non-actinoid salts followed work by Capelli [29], where an inert atmosphere heat treatment is employed for material dehydration. However, as illustrated in Table 3.2, there are several variations of dehydration procedures reported in the literature. Within this thesis, considerations of materials interaction during purification have been made, where custom equipment has been developed to dehydrate salt components in a pure nickel reaction vessel. A sand bath was used to house a Ni reaction vessel, capped with a loose Ni lid, which sat all together on top of a hotplate within the glovebox. A type-S thermocouple was submerged in the sand bath to the same depth as the reaction vessel and used to predict the actual tem-

perature of material within the vessel by means of an attached temperature recorder. Figure 5.4 depicts the dehydration equipment employed within the glovebox. The dehydration process developed within this thesis is thoroughly described by a written SOP, included in Appendix A.3. Summarizing the literature practises of dehydration, Figure 3.4 helped propose a dehydration procedure subjecting materials to 350 °C for 5 hours.

Figure 5.4. The non-actinoid fluoride purification infrastructure developed for use within the glovebox. A Ni reaction vessel holds fluoride salts in a sand bath, while being heated with a hot plate. There is also a thermocouple recording the temperature of the sand as a best approximation of the temperature of the salt quantity within the vessel.

According to Table 3.2, the purification of actinoid fluorides is more demanding than the simple dehydration procedures on non-actinoid fluorides. Actinoid oxides such as $ThOF_2$ are very stable, and readily form as impurities in the fluoride forms of the actinoids. As such, different conversion processes are employed throughout literature to addresses the oxide contaminant. One common approach is to utilize a reaction with NH_4HF_2, which benefits from not requiring the safety and infrastructure required by a direct hydrofluorination process, but instead employs a multi-step reaction to acquire $HF_{(g)}$ for fluorination as an intermediate reaction product. Equation 5.1 summarizes a simplified form of the conversion reaction of a ThO_2 contaminant in ThF_4.

$$\begin{aligned} NH_4HF_2 &\xrightarrow{\Delta} NH_3 + 2\,HF \\ ThO_2 + 4\,HF &\longrightarrow ThF_4 + 2\,H_2O \end{aligned} \tag{5.1}$$

However, practises reported in literature on molten salt thermodynamics (Table 3.2) do not reflect the optimal process reported in dedicated studies on the NH_4HF_2 method [78, 81]. In particular, the direct heating of a mixture of NH_4HF_2 with ThO_2 is reported by Che *et al.* as producing undesirable contaminants (such as $ThOF_2$), yet this phenomena is not suggested by molten salt literature employing such reactants [81]. Che *et al.* show with crystal structure that complete purification may only be obtained with a multi-day long reaction at room temperature followed by a heat treatment, whereas Capelli demonstrates that a direct heating procedure produces an improved ThF_4 purity according to crystal structure and melting point measurements [29].

Despite varying reports in the literature on the employment of NH_4HF_2 purification, an excess of $HF_{(g)}$ generated within the glovebox is not desired. As a result, a novel reaction vessel was designed to house such a reaction within the controllable atmosphere of the glovebox. Such a design is shown in Figure 5.5 (a), which shows a two chamber Ni vessel for separating neutralizing agent NaOH from the NH_4HF_2 reaction. In the stacked reaction vessel design, the upper Ni vessel holds solid NaOH to neutralize $HF_{(g)}$ which escapes the lower Ni vessel by means of a welded Ni pipe welded to the floor of the upper vessel. As a result, an excess of NH_4HF_2 is expected to be required, considering the losses of escaped $HF_{(g)}$ to the upper chamber. By holding a mixture of 1:5.5 (molar fraction ThO_2:NH_4HF_2) at room temperature for 5 days, followed by heating at 450 °C for 5 hours, literature reports that a synthesis of high purity actinoid fluorides can be achieved [81]. The equipment for fluorination and subsequent dehydration of actinoid materials is depicted in Figure 5.5 and the

details of the procedure were developed in the form of an SOP according to the most recent paper on the topic, shown in Appendix A.5 [81].

(a) (b)

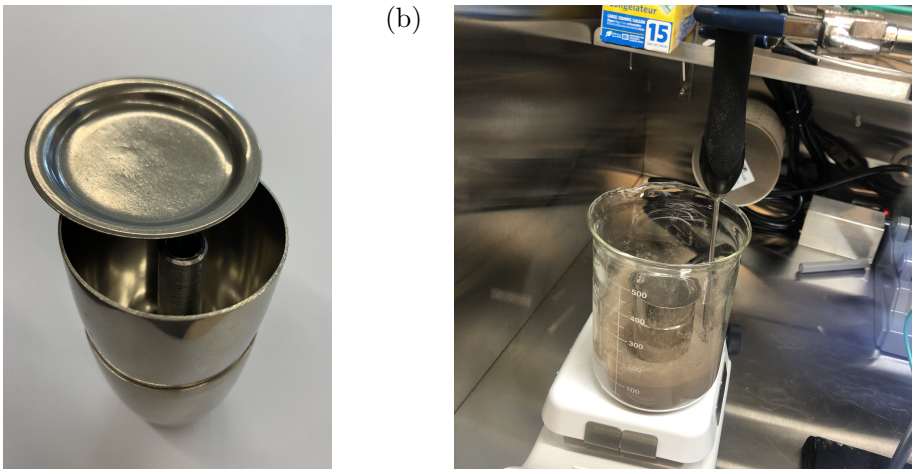

Figure 5.5. (a) The NH_4HF_2 stacked reaction vessel for purification of actinoid fluorides. (b) The actinoid fluoride purification apparatus where the stacked reaction vessels are immersed in a sand bath with a thermocouple recording the temperature for use within the glovebox.

5.4 Mixing

To mix compositions of multi-component salt mixtures, two approaches have been reported in the literature. One method is the use of bulk mixing, which favours the replicability of repeat measurements without compositional error effects. Another method that is commonly employed is to directly weigh salt components into a crucible at the particular fractions, referred to in literature as the DMM [79, 83, 86]. Although the DMM introduces compositional variance in repeat measurements, Rogers *et al.* reflect that for single measurements, the DMM reduces the handling of the samples, and subsequently provides the lowest probability of introducing contamination into particular salt mixtures [43]. Additionally, samples of decanted mixtures from a bulk mixed quantity are not explicitly known to such a degree as the DMM. Such an ap-

proach would specifically require a statistical approach for repeat measurements to estimate the only known composition, the bulk.

To perform the DMM, a single-use paper funnel system was used with integration into the scale within the glovebox. Figure 5.6 demonstrates how salt components may be directly introduced to the small DSC crucibles and weighed with a low probability of spilling the crucible.

Figure 5.6. The DMM technique developed for mixing specific compositions directly into DSC crucibles within the glovebox.

5.5 Qualification of the Measurement Routine

Investigating the success of purification efforts by crystal structure and melting point measurements has been a common practise reported across both early and modern literature. Furthermore, to qualify the influence of processing and pre-measurement handling on fluoride salt compositions, developing a framework for studying fluoride salts may rely on such approaches. For instance, the use of an agate mortar and pestle may be understood with respect to its influence on material composition, or the storage and materials interactions during DSC measurements themselves may be

qualified. Across the framework of experimental techniques illustrated in Figure 5.1, qualification efforts have therefore also been proposed, including crystallographic and melting point analysis for purity assessment and particle size measurements for the procedure of grinding.

However, literature demonstrates that such measurements are generally conducted by XRD and DSC, techniques performed outside of the inert atmosphere of the glovebox [29]. This is reflected by the qualification scheme proposed as red arrows Figure 5.1. The encapsulation of compositionally constant material samples for DSC has been discussed with the development of a screw-top crucible which can be sealed within the environment of the glovebox. The STA instrument employed is shown in Figure 5.7 (a), and a close up image of two crucibles sitting in the STA's sample holder is depicted in Figure 5.7 (b).

Little discussion is available in open literature on considerations made to minimize composition errors during XRD however. The only detail in the open literature that was found on details of XRD was from Capelli who reports the use of an epoxy matrix to set and protect powdered materials within the solidified material [29]. In an effort to reduce the infrastructure required in the limited space of the glovebox, and to avoid vapour generation within the glovebox, a dome-style XRD holder was procured for sealing materials with an encapsulated inert atmosphere from the glovebox. The base of the dome-style holder is made of silicon zero-background material, and the dome of the holder of an X-ray transparent plastic. The Rigaku Ultima IV XRD instrument available is shown in Figure 5.8, along with the dome-style holder used for reducing the possibility of in-situ contamination during measurement. In an attempt to standardize the XRD practises within the NFMG, an SOP was written and is included as Appendix A.4.

(a) 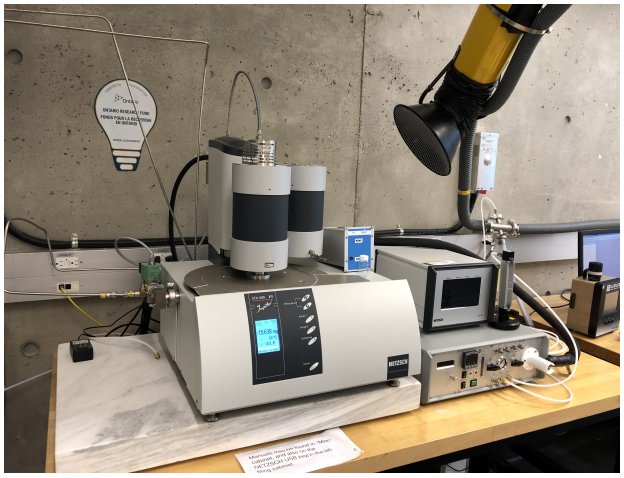 (b) 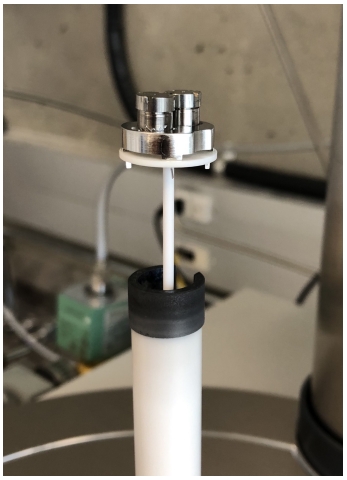

Figure 5.7. (a) The Netzsch STA 449 F1 Jupiter used. (b) A differential pair of crucibles sitting on top of inert Al_2O_3 discs within the high sensitivity TGA-DSC-C_p sample holder. Included is the presence of the Netzsch Oxygen Trap System.

(a)  (b) 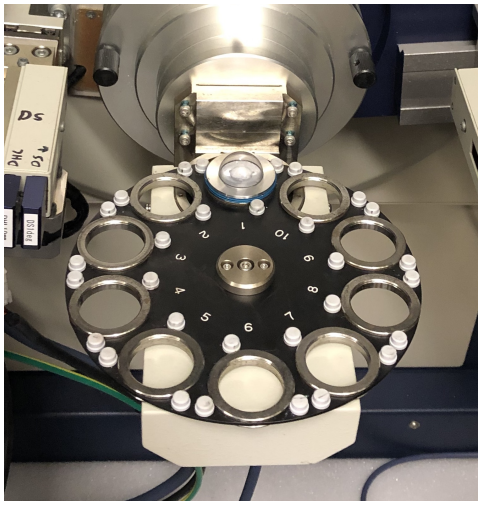

Figure 5.8. (a) The Rigaku Ultima IV XRD instrument available to the NFMG at UOIT. (b) The dome-style XRD sample holder employed for all fluoride salt materials. Materials filled in the holder and sealed within the dry and inert atmosphere glovebox.

CHAPTER 6

A Crucible for Differential Scanning Calorimetry

One consideration in an experimental measurement on fluoride salts is the crucible used to hold the sample during measurement. This is evident in a majority of published literature, where the development and performance of custom encapsulation techniques have been reported for measurements ranging from rudimentary thermal analysis (Figure 3.2) and quenching studies to modern EXAFS and DSC investigations (Figure 3.3) [38, 66, 92]. Such crucible designs were complicated beyond traditional crucible designs as a result of the reactive nature of fluoride salts. In measurements such as DSC for nuclear applications however, where there is an utmost stress on safely understanding phenomena to a high degree of accuracy and replicability, implications from crucible design are magnified. Specifically, such a crucible may be designed with the intention of studying radioactive material in a liquid and gaseous state, and small sample sizes may exhibit energetically small thermal events which may be difficult to observe experimentally. Thus, prior to qualification of the measurement routine or to performing novel measurements, an evaluation of available fluoride compatible DSC crucibles was made, along with a consideration of designing a custom crucible for the

Netzsch STA 449 F1 Jupiter instrument. This is especially significant considering that a portion of a thermodynamic measurement's qualification is concerned with inferring material purity by melting point determination, which in itself requires the use of a crucible for DSC.

6.1 The Crucible Design Process

Crucible design is not the only consideration in the accuracy of a measurement from DSC. Instead, accuracy may be typically realized through post- and pre-test techniques such as calibration, where, as long as measurements are replicable, a systematic error may be quantified and accounted for by calibrating the campaign to reference measurements. Furthermore, subtracting the behaviour of an empty crucible under identical conditions from an actual measurement allows phenomena experienced only by the sample material to be deduced, with theoretically no fingerprint from the crucible on the measurement [84]. Lastly, transient thermal effects which are systematic can be captured by calibration encompassing varying ramp rate measurements [28]. The most imperative function of a DSC crucible is instead to provide precise, high-resolution measurements. For the study of non-reactive systems, the precision of a DSC crucible's measurement is primarily influenced by the consistency of local experiment conditions and the variability in manufactured crucibles. It is clear from reports in the literature that if a crucible design is capable of providing sufficient measurement sensitivity to generate conclusive results, a high level of precision in ordinary DSC measurements is easily achieved [67].

Complications arise in the design of a crucible when its function is to provide DSC measurements of volatile species. With the possibility of crucible-sample interactions as potential sources of compositional error, considerations in the design of a crucible for DSC investigations on fluoride salt (which are corrosive and hygroscopic) are extended beyond the condition to provide precise measurements. Both the accuracy

and precision in the case of a fluoride salt DSC measurement are therefore significant factors in crucible design, as material interactions cannot be accurately calibrated out of a precise measurement, as most other accuracy concerns are. With the following design function, it is evident why numerous techniques in early and modern literature discuss the use of custom designed crucibles for both protecting the composition of the salts and protecting experimental equipment from the vapour of fluoride molten salts [37, 66, 92]. Due to the lack of confidence in the ability of commercially available Netzsch DSC crucibles to meet such a definition for studying fluoride salts, a custom crucible has to be employed. The following design criteria were identified for a crucible compatible with the NFMG's Netzsch STA 449 F1 Jupiter instrument.

An acceptable crucible design must be able to provide high resolution, accurate, and replicable measurements in a safe, economic, and practically feasible manner.

- Maintain a hermetic seal at 1200 °C and 0.5 MPa
- Crucible + sample mass less than 2.5 g [146]
- Constructed by highly replicable techniques
- Constructed with procurable materials
- Experience minimal wall-salt interactions
- Less then 18 mm in total height [146]
- Less than 6.8 mm in outer diameter from the base up to 15 mm in height
- Constructed with a flat, smooth floor
- Constructed with a wall thickness as thin as feasibly possible, particularly the floor
- Rotationally symmetric in the vertical axis

Analogous to related literature reported by the European Commission, this thesis initially proposed adopting the only DSC crucible design presently qualified for fluoride salt measurements, shown in Figure 3.3 [29, 66, 68]. However, differing measurement instruments between the two institutions restricted the employment of such a design, and required that consideration be made into developing a custom crucible for in-house measurements by the NFMG. The measurement device that drove design criteria for the Beneš et al. crucible was a cylindrical Setaram DSC, with a series of thermocouples along the circumference of the crucible [66]. The instrument used by the NFMG at UOIT, however, is a plate style Netzsch STA 449 F1 Jupiter, which has a single thermocouple positioned underneath the floor of the crucible by the sample holder. Although crucibles for both systems serve the same function, two limiting differences were identified between the design criteria of the two systems. The scale in the Netzsch F1 STA is limited to a maximum mass of 5 g and a crucible height of 1.9 cm, whereas the Beneš et al. crucible is itself 14.39 g and 3.563 cm tall. Additionally, advantages of a multi-thermocouple layout in the Setaram DSC afforded the Beneš et al. crucible design with less sensitivity to the heat conduction of the crucible compared to the single floor thermocouple of the Netzsch system.

There are also early crucible designs that were successfully employed by ORNL, as shown in Figure 3.2. Early crucible designs for molten fluoride salts established mitigation techniques to reduce compositional error, such as material selection in Table 3.3, hermetic sealing, and floating graphite discs to reduce evaporation. ORNL's custom crucible also addressed mixture homogeneity with innovative mixing infrastructure which only operated when samples were in a liquid state, and designed room for measuring multiple (4) samples at once [37]. However, with the historical transition from temperature profile thermal analyses to DTA, and with modern approaches advancing further with use of DSC, crucible designs by ORNL cannot be explicitly employed by modern techniques. For example, work by Khoklov et al. and Capelli et al. demonstrated how modern homogenization of sample mixtures can be achieved

by simply performing a number of pre-measurement temperature ramps and evaluating the produced thermogram for convergence [64, 67]. Modern instruments are also commercially available, such that crucible design is now also limited to the functional and physical requirements of the instrument. For instance, most modern devices do not permit room for multiple samples to be measured at once, or for external mixing infrastructure to be incorporated within the furnace. Early work did nonetheless establish the groundwork for material selection and hermetic sealing.

With the advent of commercial measurement devices, there are also commercially available crucibles which are compatible with the Netzsch STA 449 F1 Jupiter. Included in the crucible catalogue from Netzsch are screw top, gold gasket designs, intended for high pressure applications up to 100 bar. By replacing the temperature limiting, stock, gold gasket with nickel, and lining the Ni−Cr alloy crucible with an inert material, discussions on modifying the commercially available, high-pressure (screw-top) crucibles from Netzsch were also explored beyond a completely custom crucible design.

Flexibility in the design of an inert liner was also investigated for a commercial crucible or a custom crucible. It was conceptualized that machined BN such as in the European Commission design, a curable paint of BN, or an inert metallic insert such as nickel or molybdenum could serve as inert material liners. However, it was also understood that a lined crucible design had only been qualified for a Setaram DSC device, where crucible design is not only afforded with greater measurement sensitivity than the single (floor) thermocouple Netzsch design, but sample masses are permitted to be much larger [66]. As a result, concern was identified for the materials compatibility improvements being negated by the thermal conduction degradations of an added floor thickness in the Netzsch DSC instrument. It was also recognized that with an inert metal liner, or a design without a liner (the crucible body being constructed of an inert material instead), that calibration of a crucible may be more

challenging. Standardized calibrant materials being metal elements, alloying with a metal crucible is possible, and thus the use of other calibrants may be required as summarized by literature in Table 3.2. Employing salt based calibrants also has the advantage of capturing the wetting behaviour of molten salt samples, however a main limiting factor is also the standardized reference values available with such materials [71, 82].

There were also economic considerations that were made, given Beneš et al.'s report that that screw-top crucibles are not reusable when subject to temperatures applicable to molten fluoride salts [28]. It is clear that a complex environment of performance considerations is present with a myriad of design options for designing a DSC crucible. A review of the high-level performance considerations of a variety of screw-top crucible designs has been constructed in Table 6.1. Check marks (✓) in Table 6.1 represent parameters which are deemed acceptable, whereas x-marks (✗) identify ones which represent a challenge for the crucible design relative to the other designs in the table. It should also be noted that per crucible costs in Table 6.1 are very approximate and were hence not a driving factor in the crucible design process.

Considering the cost, a hole in the lid, and the challenge of assembling the Netzsch crucibles within a glovebox, a decision was made to investigate an in-house custom crucible design. A secondary benefit was also realized with a designing custom crucible: within the prototyping stage of crucible design, a custom design allowed the possibility of designing a generalized, flexible crucible which could serve as either a body for an inert material liner, or as a non-lined crucible itself.

Table 6.1. A high-level summary of performance trade-offs between potential crucible designs.

Crucible version	Structural integrity	Calibration	Heat conduction	Material interactions	Fabrication (cost [$])[b]
Custom inert metal	t.b.d. *	✗†	✓	✓[a]	Swiss turning (200)
Custom, BN lined	✓	✓	✗‡	✓	Painting (85), machining (180)
Commercial, BN lined	✓	✓	✗‡	✓	Painting (105), machining (180)
Commercial, inert metal lined	✓	✗†	✗‡	✓[a]	Punching (110), machining (140), deposition (120)

* High temperature structural properties of inert metals such as Ni are less understood than traditional structural alloys such as stainless steel.
† Metallic references: potential for alloying, no wetting behaviour captured. Salt materials: Questionable reference data.
‡ Due to additional thickness.
[a] Wetting expected.
[b] Approximate, per crucible.

With a concern for the salt material's hygroscopic and reactive nature, the physical design of a crucible was first limited to one that permitted samples to be sealed inside an inert atmosphere prior to measurement. Maintaining a hermetic seal is also important to protect sensitive instrument electronics from the vapour pressure of fluoride salts. The practicality of achieving a hermetic seal with a screw-top and gasket design, such as that originally established by the European Commission, was the first design decision for the NFMG's crucible. Such a design was driven by both the confidence/replicability of a threading system and the feasibility of employing other techniques within the glovebox employed. Other design techniques such as welding and crimping have been demonstrated in earlier literature to be successful, however the complication of developing the required infrastructure for such processes at UOIT did not favour a crimp and weld seal design [37].

By defining specific design criteria, a number of considerations also became apparent in the process of designing a successful screw-top crucible. Immediately apparent was the underlying influence of materials selection on a large number of aspects of the performance of the crucible. One consideration that was made was the strength of the material to withstand molten fluoride salt vapour pressures and the thermal expansion of such vapours. By providing structural integrity to the crucible, design criteria regarding safety and accuracy may both be met. However, not only is material strength complicated by the application of molten fluoride salts, where high temperature and highly corrosive environments exist, but materials selection is also highly related to corrosion resistance for compositional accuracy concerns. The requirement for hermetic sealing of the crucible further drove materials selection to also consider the fabricability of candidate materials. Materials selection for designing a DSC crucible was thus driven by corrosion resistance, high temperature strength, commercial availability, fabricability, and economics.

Inspired by prior materials selection of the MSRE and MSBR program, an initial

interest in crucible materials was the Hastelloy-N alloy designed by ORNL for early MSRs. Hastelloy-N offers a salt facing material which demonstrates relatively acceptable corrosion resistance to common molten fluoride salts and has applicability to common structural materials of modern MSR designs as well [88]. If quantities of, or sensitivities to impurities could be quantified, even with a finite amount of Hastelloy-N impurity introduced into the salts, such a crucible design may prove applicable to commercial reactor development. Unfortunately, laboratory scale quantities of Hastelloy-N were not found to be available for procurement.

Auxiliary considerations were then made by surveying the literature for materials which demonstrated research quality salt facing behaviour, as summarized in Table 3.3. Considering the design criteria of a hermetic seal, it was clear that crucibles constructed purely out of materials such as Boron Nitride (BN) or graphite could not be obtained easily while meeting the design criteria (an enclosed pressure tight crucible of such material is not feasible). A modification to the European Commission crucible was therefore proposed: a screw-top crucible either constructed purely out of a salt friendly metallic material (*e.g.* nickel, platinum, or molybdenum) or out of traditional alloys internally lined with a salt stable material, such as BN or inert metals. Although few of such crucible designs had been acknowledged in literature, the BN lined stainless steel crucible of the European Commission gave an initial experience towards this variation of the screw-top design, which is shown in Figure 3.3. The BN lined stainless steel crucible has been been actively employed across studies published by the European Commission, and also subject to type-B considerations (qualification) against the $NaNO_3-KNO_3$ system [66]. By lining the walls of a crucible with BN, Beneš et al. also identify BN's ability to reduce the hydrophobic wetting behaviour of salts, something important not only for single measurement sensitivity, but towards the accuracy of calibration as well [147].

Referring to the literature review (Table 3.3) on salt-facing materials which have

been used in research, nickel was identified as a promising candidate material for a non-lined crucible design. Although structural properties of nickel are uncertain at high temperatures (*e.g.* 1000 °C), Ni 201 was selected intentionally to minimize the greening phenomena generally associated with the degradation of such alloys in an oxidizing high temperature environment. Nickel 201 was also ran through a screening qualification test where a Ni-201 tube of (3 mm) wall thickness was heated to 1100 °C in air for 2 hours and subsequently pinched with vice grips to qualitatively assess the extent of high temperature strength degradation. Prior to such treatment the same vice grip was used to establish baseline experience on a separate as-received Ni-201 tube's performance under such a stress at room temperature. The high temperature strength of Ni-201 was qualitatively found to experience little degradation within the stress applicable to molten fluoride salt vapours. Furthermore, Ni 201 is commercially available and economically feasible, however the alloy is also subject to inexperience and challenges when fabricated by traditional machining techniques.

A liner version of the crucible was also developed, which identified conventional stainless steel 304 as a contingency plan which could be used as an easily machinable material for the body of a liner version of the crucible, as per the European Commission design [66]. For inert material liners, solid inserts such as BN, nickel, or molybdenum were proposed as the most promising techniques, as deposition methods were found to introduce impurity concentrations of non-inert materials and exhibit feasibility challenges with their application on such a small scale.

With respect to the physical dimensions of the crucible, an iterative approach was adopted which allowed a number of synergistic considerations to be taken into account. The crucible geometry (*i.e.* wall thickness, volume, diameter) was iterated through a sequence of pressure vessel wall strength, thermal expansion, fabricability, and overall mass calculations to optimize a crucible design which was consistent with the design criteria outlined on page 61. After verifying the 0.5 MPa design pressure

from Beneš et al., wall strength calculations were performed according to pressure wall failure criteria [66]. The structural failure criteria were based on the argument of a thick-walled crucible experiencing an axial (σ_a), radial (σ_R), or hoop stress (σ_h) 0.5 times the high temperature yield strength of the material (1.5 safety factor and a mean diameter:wall thickness ratio of ≈ 12) [28]. The thick-wall pressure vessel calculations were performed according to Equations 6.1, 6.2, and 6.3, where the hoop stress was found to be the pressure limiting stress (P_{outer}, P_{inner}, r_{outer}, and r_{inner} represent the outer and inner pressures and radius of a pressure vessel). It should be noted that no structural degradation as a result of corrosion was accounted for in the stress calculations.

$$\sigma_a = \frac{P_{inner}r_{inner}^2 - P_{outer}r_{outer}^2}{r_{outer}^2 - r_{inner}^2} \tag{6.1}$$

$$\sigma_h = \frac{P_{inner}r_{inner}^2 - P_{outer}r_{outer}^2}{r_{outer}^2 - r_{inner}^2} - \frac{r_{inner}^2 r_{outer}^2 (P_{outer} - P_{inner})}{r^2(r_{outer}^2 - r_{inner}^2)} \tag{6.2}$$

$$\sigma_R = \frac{P_{inner}r_{inner}^2 - P_{outer}r_{outer}^2}{r_{outer}^2 - r_{inner}^2} + \frac{r_{inner}^2 r_{outer}^2 (P_{outer} - P_{inner})}{r^2(r_{outer}^2 - r_{inner}^2)} \tag{6.3}$$

Thermal expansion was considered in the non-liner version of the design by limiting the outer diameter of a nickel crucible body (thermal expansion coefficient of 16.9×10^{-6}) [148] to 1 mm (15%) less than the inner diameter of the platinum Netzsch sample holder (thermal expansion coefficient of 9×10^{-6}) [149]. In the design of a crucible body intended to fit a liner, a BN insert can be designed to be tight-fitting with the inner diameter of the crucible body due to its smaller thermal expansion coefficient (parallel: 1.6×10^{-6}, perpendicular: 0.4×10^{-6}) [150] than stainless steel

(18.7×10^{-6}) [151]. Thermal expansion was also accounted for in the distance between the lids of the sample and reference crucible as placed within the Netzsch STA crucible holder during a measurement, as depicted in Figure 5.7 (b). Thermal expansion calculations were performed according to the strain theory defined in Equation 6.4 (T_{final}, $T_{initial}$, D_{final}, and $D_{initial}$ being the respective temperatures and diameters at final and initial temperatures, while α represents the coefficient of thermal expansion for a given material).

$$D_{final} = ([T_{final} - T_{initial}]D_{initial})\alpha + D_{initial} \tag{6.4}$$

The design iteration process is illustrated in Figure 6.1, where all calculations were made conservatively. As previously mentioned, the iterative design process began with a materials selection identifying either a Ni-201 inert metal crucible design or a stainless steel 304 material for the body of a lined crucible. Material properties from each crucible design were then coupled with initial baseline crucible dimensions as input into pressure wall, thermal expansion, mass calculations, along with fabricability considerations. Each consideration in the iterative process was subject to the design criteria (page 61) and instigated dimensional iterations upon failure of any design criteria. Once all design criteria were met accordingly, a final crucible design was proposed which could serve as a stand-alone crucible or the structural body of a liner version of the crucible.

Intermittently throughout the iteration, prototypes were constructed as shown in Figure 6.2 (a) and (b). Dimensional tolerances were assessed with 3-D printed plastic crucibles, while thread design and physical handling were scrutinized against early stainless steel crucible prototypes. The timeline illustrated in Figure 6.2 concludes at the final prototype of a Ni-201 crucible which was fabricated.

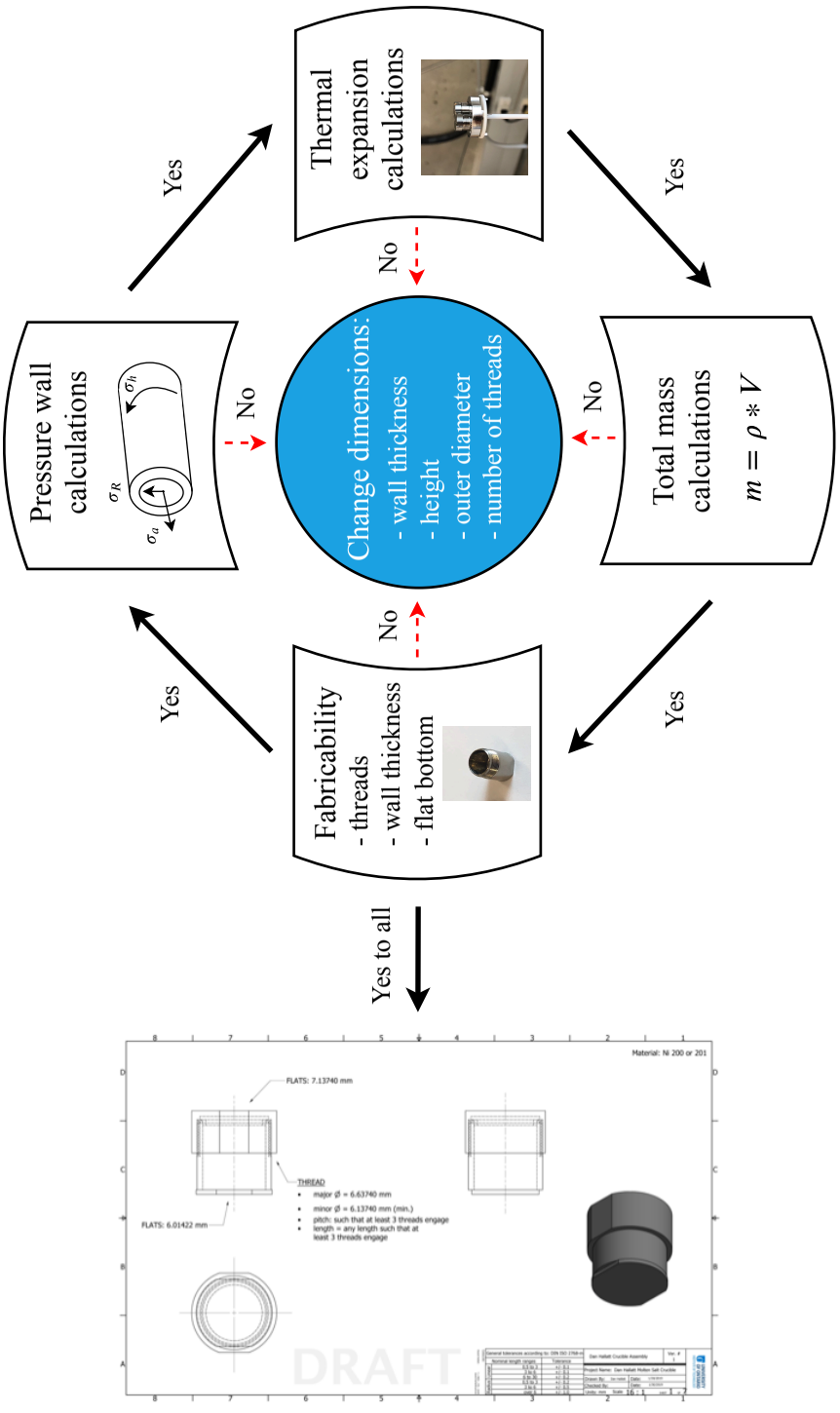

Figure 6.1. The design iteration process of a custom crucible for fluoride molten salt DSC measurements with a Netzsch STA 449 F1 Jupiter. Initial materials selection not shown here (chemical stability, cost, structural). Failure to converge would results in revisting materials selection. Passing conditions subject to design criteria defined on page 61.

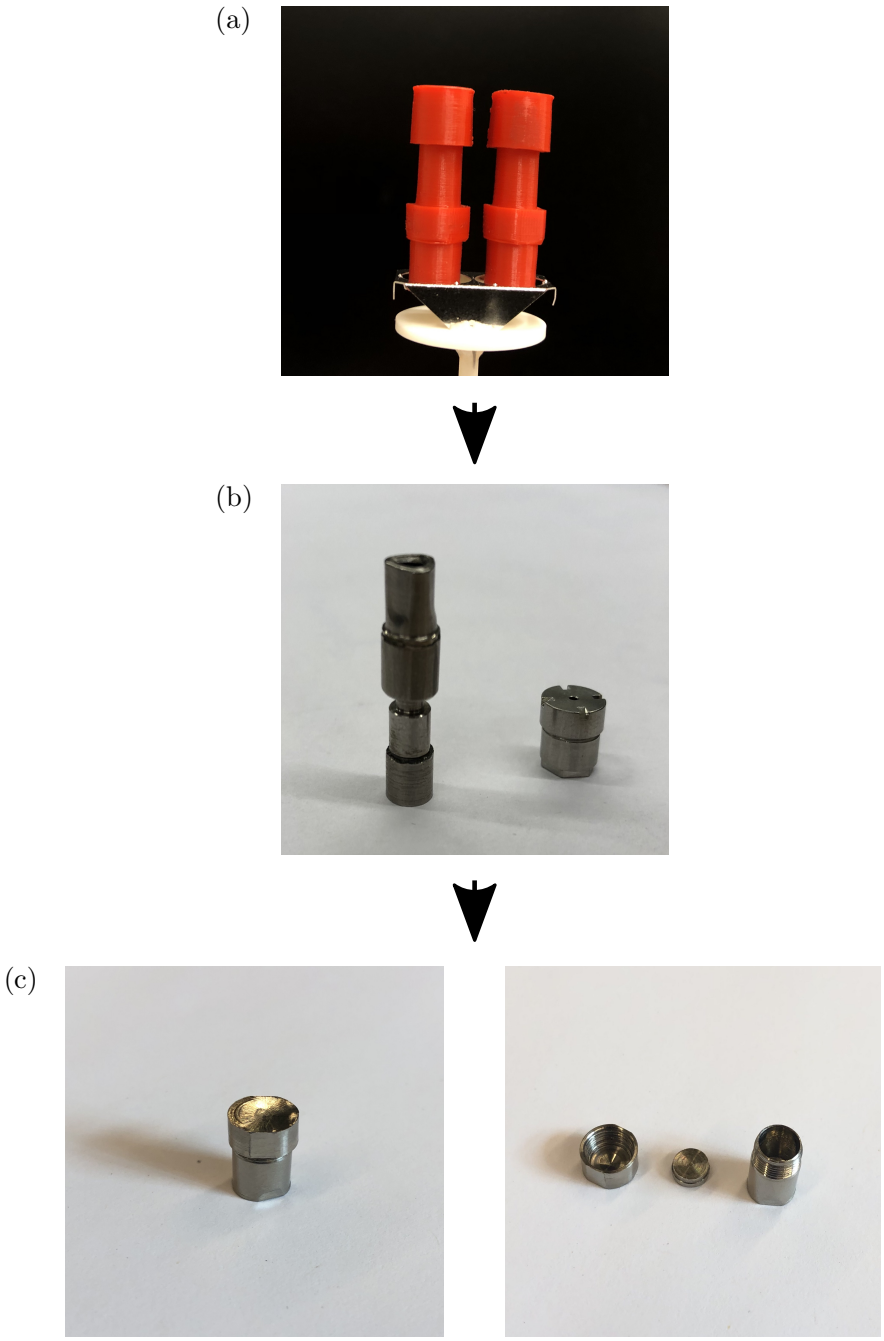

Figure 6.2. The timeline of design iteration of a prototype custom crucible for fluoride salt DSC measurements with a Netzsch STA 449 F1 Jupiter. (a) 3-D printed plastic prototype for dimensional fitting in crucible holder. (b) Stainless steel prototype crucible used to assess feasibility of threading and practises in glovebox. The crucible is to the left of a commercial Netzsch high-pressure crucible for reference. (c) Final nickel prototype crucible machined by Swiss turning.

A crucible design produced from such an iteration process is illustrated in Figure 6.3. The crucible design includes sharp edges on the bottom of the lid's threads and on the top of the body's threads for sealing a nickel gasket. A nickel gasket fits within the lid as a sealing medium to be partially crimped by the sharp edges of the lid and body. This gasket is shaped in a *top hat* design, to allow the gasket to partially sit into the body of the crucible for easier manipulation within the glovebox. The lid and body are also designed to include flats for ease of threading and manipulating the crucible within the glovebox. The final crucible is designed to weigh approximately 1.52 g empty (2.20 g maximum when filled with the heaviest component of interest, ThF_4), and offer an internal sample volume of approximately 99.8 mm^3. The crucible body is designed to withstand a pressure of 0.5 MPa with a 0.5 mm wall thickness and be machined to have a floor thickness of 0.4 mm for heat transfer to the Netzsch STA Jupiter 449 F1's single thermocouple. The outer diameter of the bottom of the crucible is predicted to expand from approximately 6.8 mm to 6.91 mm when ramping to 1100 °C, which leaves critical room between the platinum holder which is predicted only to expand from 6.90 mm to 6.98 mm in diamater. Figure 6.4 illustrates a designed crucible holding device to aid in the screwing together of the crucible within a glovebox. With such a holder device, the crucible would be restricted in all degrees of freedom, and the effective working size would be amply increased while working in the glovebox.

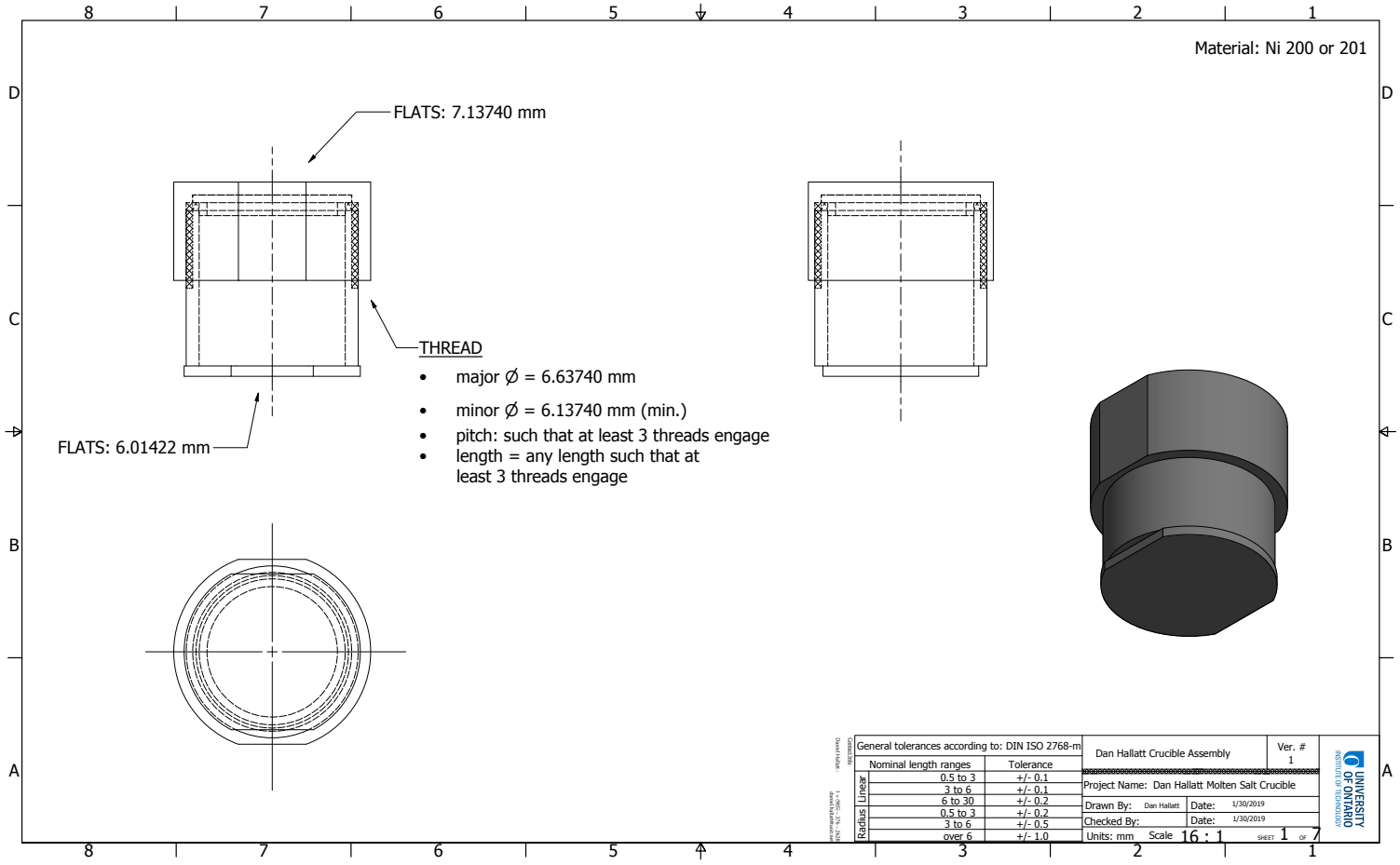

Figure 6.3. An innovative crucible design for fluoride molten salt STA measurements with a Netzsch STA 449 F1 Jupiter.

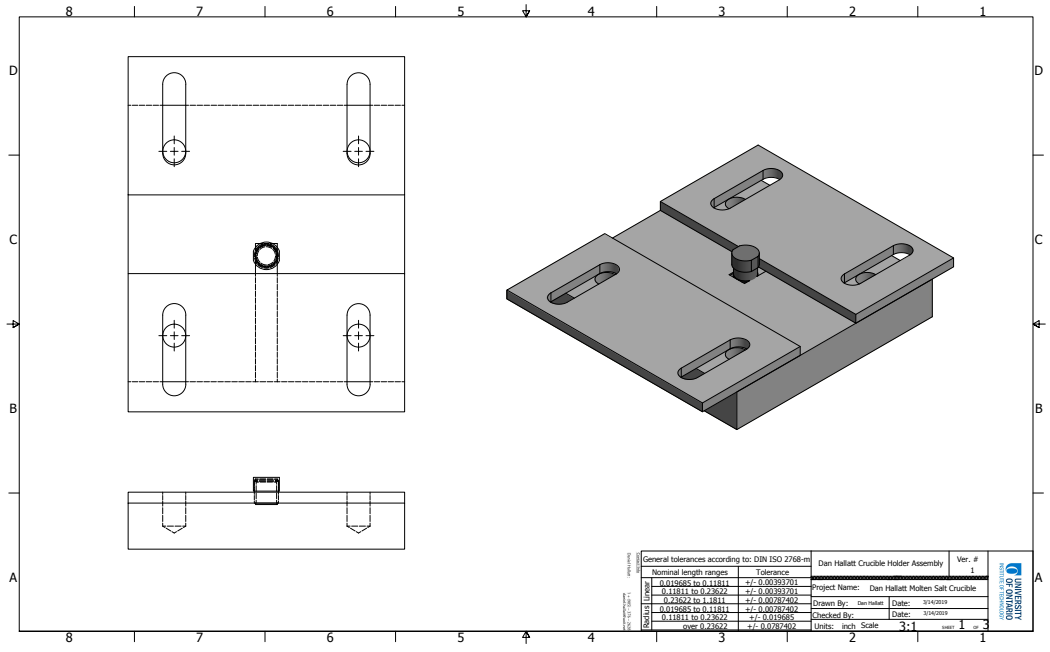

Figure 6.4. A holder device designed to aid in sealing the in-house designed crucible.

6.2 The Conclusion on Available Crucibles

Converging on the in-house crucible design illustrated in Figure 6.3, a bid for fabrication was offered to local machine shops. A focus on fabricating a non-lined version of the crucible was of primary interest, as fabricating a crucible out of a single material was predicted to be cost effective, measurement sensitive, and fabricable within the timeframe of a two year masters degree. With this design came requirements on finding a machine shop which could work with Ni-201 on a dimensionally small scale and which could supply a number of precise crucibles. A promising vendor was found in Advanced Machining of Fenella, Ontario who could employ their Swiss Turning capabilities to precisely machine crucibles according to the engineering drawings in Figure 6.3.

A resulting crucible prototype is shown in Figure 6.5 which was fabricated by

Advanced Machining. Despite obtaining four crucible prototypes however, Figure 6.5 represents a severe challenge that was identified in the fabricability of such a Ni crucible design.

(a) (b)

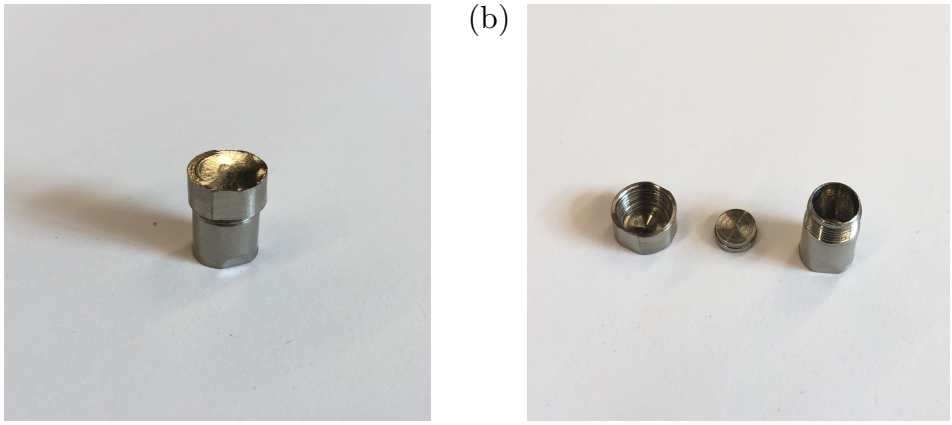

Figure 6.5. (a) Final prototype of Ni crucible designed in-house. (b) The three parts to the prototype of the Ni crucible, from left to right: lid, gasket, and body.

As the obtained crucibles were still a prototype, machining the Ni-201 required the machinist to make adjustments to the crucible's dimensions, ultimately resulting in the crucibles failing to meet the mass design requirement of 2.5 g (filled). Furthermore, the thickness of the crucible floor was fabricated thicker than the design, which complicates the confidence of their ability to provide accurate DSC measurements in a Netzsch STA 449 F1 Jupiter. The important differences between the fabricated Ni crucible prototype and the submitted design are outlined in Table 6.2.

Table 6.2. A comparison of the original STA crucible design (Figure 6.5) with the final prototype crucible which was fabricated.

Property	Design	Prototype
Empty Mass (g)*	1.52	2.52
Floor thickness (mm)	0.40	2.50
Wall thickness (mm)	0.25	0.60
Outer diamater of base (mm)	6.80	6.80

As a result of the failure of the fabricated Ni crucible prototypes to meet the mass requirements of the Netzsch STA 449 F1 Jupiter instrument, the crucible prototypes depicted in Figure 6.5 could not be used for obtaining DSC measurements. Consequently, further refinement to the Ni custom crucible design was stopped, and the alternative crucible options from Table 6.1 were reconsidered to address the goals of this thesis. Initially, a BN liner was considered for use in either the custom crucible design (with a structural body being constructed of a material easier to machine such as stainless steel) or the commercially available Netzsch high pressure crucibles. Although Figure 6.6 depicts a BN liner designed for the commercial Netzsch crucible, procurement of the machined liners shown in (a) of Figure 6.7 took far too long to be investigated within a reasonable timeline for this thesis. A bn lined custom crucible design was also discarded, as it was expected that the design would suffer from the fabrication and procurement timeframes associated with machining a second collection of stainless steel custom crucible prototypes in addition to the BN liners themselves.

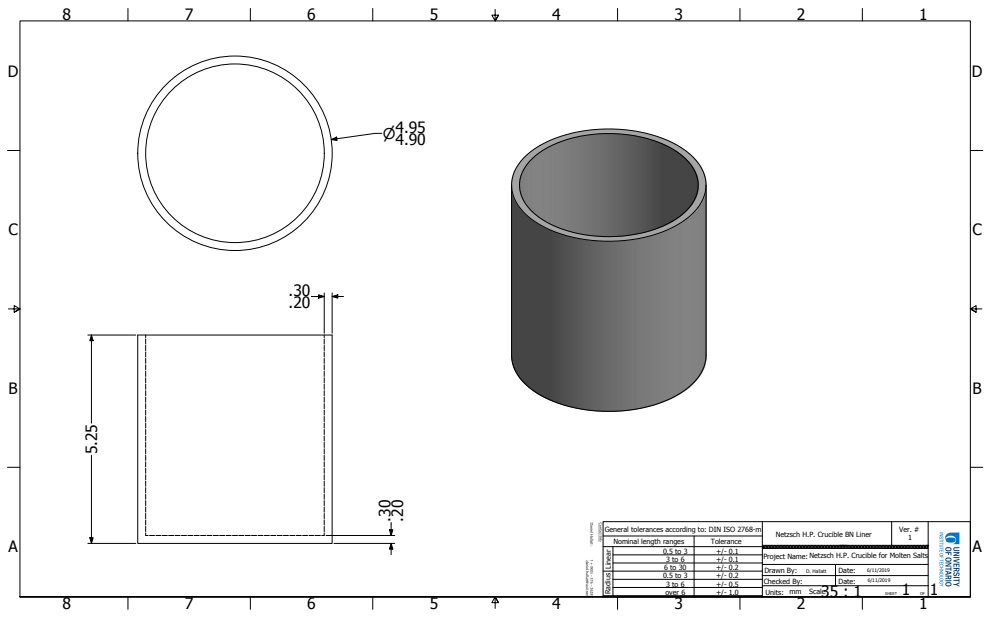

Figure 6.6. An engineering drawing of the BN designed for implementation into the Netzsch high pressure crucible.

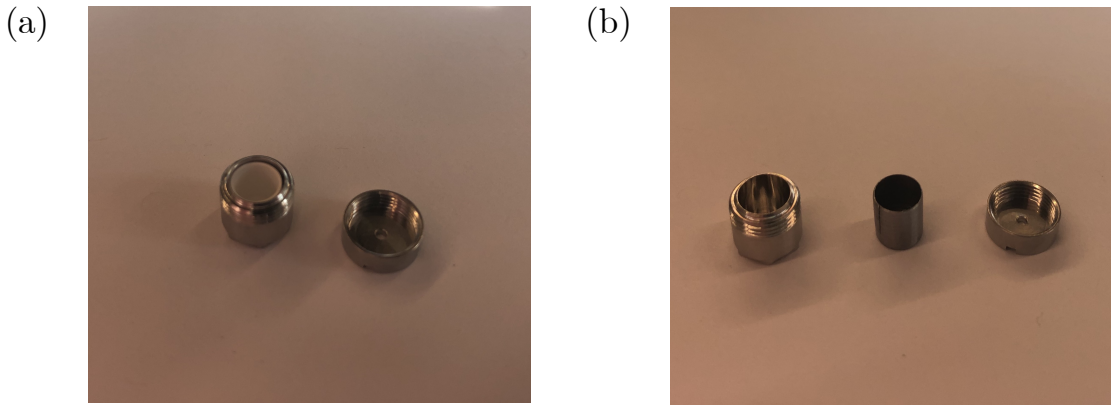

Figure 6.7. (a) Table 6.1's BN lined commercial crucible design for future qualification within the Netzsch high pressure crucible. (b) Table 6.1's Mo lined commercial crucible design for future qualification within the Netzsch high pressure crucible.

Reluctantly, it was compromised that the role of DSC in Figure 5.1's qualification of the measurement routine, could be realized with the use of non-lined Netzsch high pressure crucibles, provided that measurements made with such crucibles were evaluated relative only to similar measurements also made with the same Netzsch

commercial crucibles and not employed to draw conclusions on the basis of external reference standards. Taking the error of such measurements to be the quoted precision of the measuring instrument ($\pm 0.3\,^{\circ}\mathrm{C}$ [152]), inaccuracies associated with potential material interactions with the Netzsch crucible can be approached by shifting the conventional interpretation of DSC measurements from being stand alone observations to instead evaluating the differences between measurements. By using DSC measurements in such a way, the parameters of interest from DSC measurements are in fact the changes in the DSC differential signal between independent measurements, and act as form of block to the material interactions if assuming such errors are systematic. In a sense, this approach can be identified as a form of *differential* differential scanning calorimetry. Adopting such an approach, the Netzsch high pressure crucibles required replacement of the Au gasket with a Ni gasket to improve the expected operating temperature of the crucibles to those applicable to the salt systems of interest. Nickel which was punched from Ni-201 shim stock with the use of a punch set is depicted in Figure 6.8.

Figure 6.8. The Ni gaskets and punch set employed to retro-fit Netzsch high pressure crucibles for operation at higher temperatures applicable to a number of fluoride salts.

CHAPTER 7

Discussion of Results from Qualification

Congenital with the performance of novel thermodynamic measurements, the literature review in Chapter 3 identified value in the qualification of such novel measurement's experimental routine. The dashed, red arrows in Figure 5.1 illustrate the specifics of this thesis' intention to qualify such a routine, that of a DSC measurement of fluoride salt. Despite Chapter 6.2 discussing the difficulties in obtaining a crucible design acceptable for accurate DSC measurements with the Netzsch STA 449 F1 Jupiter instrument, it was also established in Chapter 6.2 that the use of commercial Netzsch high pressure crucibles may be sufficient for the qualification of the experimental routine. Despite Chapter 6.2 identifying the restriction of within-group interpretation using such crucibles, the use of commercially available crucibles was motivated by similar (unpublished) work which was produced by Johnson *et al.* of Besmann's group at the University of South Carolina USC. Even though the employed commercial crucibles introduce a source of compositional error, employing the same crucibles as Besmann's group at the USC allows this thesis to exploit the external measurements made at USC to provide a rudimentary form of reference data as a

standard. Such measurements by USC may also act as an insight into the sensitivity of such measurements to between-group environments. It was also decided that LiF, as a single component, was to be used as a material for the initial qualification of the measurement routine in Figure 5.1. Use of LiF not only maintained consistency with the group from USC for obvious correlation of the results, but also simplified the handling and reduction of extraneous sources of error or time (it is non-radioactive, relatively inexpensive, is reported to exhibit simple invariant melting and phase behaviour, etc.).

Using Netzsch high pressure crucibles it was realized that, for the application of qualification, systematic compositional errors associated with wall-salt interactions of the Ni−Cr alloy walls could be blocked by comparing the influence of processing techniques to measurements made on as-received material. Instead of correlating measurements to published reference values as generally done in literature, by assuming that the extent of error in each measurement consistent between measurements, interpreting the influence of a procedure could be approximated relative to an as-received measurement. The development of standardized practises is thus stressed, as it is important that external sources of error beyond those induced from the crucible also remain constant between all measurements for accurate blocking. It should also be noted that the intrinsic blocking of external environmental errors during a DSC measurement (ones not originating from material effects) further improves this argument as well.

It was also concluded that the prototype custom Ni crucibles depicted in Figure 6.5 could still be utilized to verify the expectation of a low wall-salt interactions under measurement conditions (through the liquid and solid state of fluoride salts). After qualifying the procedure for dehydration, by subjecting a quantity of dehydrated LiF to conditions equivalent to those of a typical DSC measurement (definite heat treatment and flowing Ar atmosphere) in a sealed prototype Ni crucible, XRD and DSC

measurements could be performed to investigate the influence of the Ni crucible walls relative to the results from LiF which had only been dehydrated (and not pre-melted in Ni). Such XRD and DSC was performed upon mechanical removal and division of the solidified LiF from the tested Ni prototype crucible within the glovebox.

Developed from the red, dotted arrows depicting qualification in Figure 5.1, a outline of the performed measurements in the qualification of non-actinoid fluoride salt routines is shown in Figure 7.1. To note in Figure 7.1 is an attempt to investigate the qualification of the Ni−Cr material for wall-salt interactions when using a Netzsch crucible without a liner. It is for this reason that the XRD measurement following the DSC measurement on material subject to the dehydration procedure was included: to provide insight into possible crystallographic effects from the Netzsch crucible on the LiF within all the other DSC measurements outlined in Table 7.1. For instance, if the XRD measurement on material after being dehydrated and then melted in a Netzsch crucible (during a DSC measurement) proved the same as material simply after dehydrating, differences between DSC measurements on other processed LiF and as-received LiF can be attributed to the associated processing of the material and not the crucible itself with higher confidence. Taking an XRD measurement on such material provides insight into the DSC measurements on LiF, as a portion of their inaccuracy relative to standard reference values can then be attributed to other effects beyond material purity such as a calibration.

Tables 7.1 and 7.2 outline the measurement conditions for each DSC and XRD measurements respectively that were performed according to the qualification outline of Figure 7.1. As-received material was decanted from the same lot of 99.99% pure LiF from Alfa-Aesar (lot#) and identical practises were performed between measurements according to respective procedures in Appendix A. Parameters for DSC measurements include four consecutive heating and cooling ramps $20\,\mathrm{K\,min^{-1}}$ under 99.99% Argon protective gas flowing at $250\,\mathrm{mL\,min^{-1}}$ in the Netzsch STA 449 F1 Jupiter instru-

ment of Figure 5.7. DSC measurements were made with a type-S TG-DSC sample carrier with an Al_2O_3 spacer disc and radiation shield and a single (empty) reference crucible was re-used between all measurements. XRD was performed with material held in a dome-style holder, as depicted in Figure 5.8, sealed within the glovebox, and subsequently observed between at 0.80 deg /min with a 0.020° step size. Due to the uncertainty in the high temperature performance, the radioactivity of the actinoids, and the high melting temperature of actinoid fluoride salts, qualification of the purification procedure for actinoid fluoride salts was investigated only by comparing XRD measurements before and after purification of ThF_4. Melting point analysis of the actinoid purification routine has not been studied in this work, and has been left until the confidence in a DSC crucible's performance can be matured.

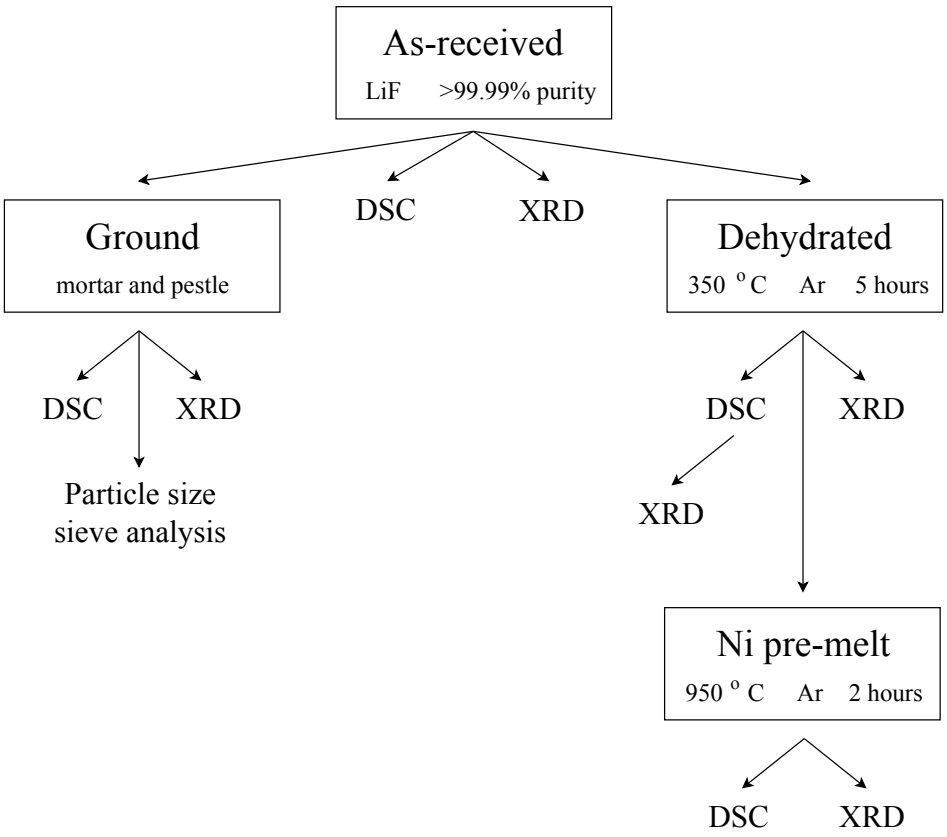

Figure 7.1. The outline for qualifying the measurement routine, according to the red arrows in Figure 5.1.

Table 7.1. A summary of measurement parameters from Figure 7.2's DSC measurements on the qualification of experimental routines using LiF. Material was sealed within an Ar filled glovebox, into new commercial Ni−Cr stainless steel high pressure crucibles with a custom Ni gasket, and measured by a Netzsch Jupiter STA 449 F1 with a type-S TG-DSC sample carrier with an Al_2O_3 spacer disc and radiation shield. A single (empty) reference crucible was re-used between all measurements.

Material	Temp. (°C)	Ramp rate (°C min^{-1})	# Ramps	Crucible mass (mg)*,†	Ref. crucible mass (mg)*,‡	Sample mass (mg)*
As-received LiF	750 - 950	20	4	1310.45	1314.59	13.40
Ground LiF	750 - 950	20	4	1314.35	1314.59	12.89
Dehydrated LiF	750 - 950	20	4	1314.27	1314.59	18.86
Ni-melted LiF	750 - 950	20	4	1305.90	1314.59	0.39

* An error of ±0.005 mg is taken as the recording error of a Sartorius Quintex analytical balance.
† Empty crucible.
‡ The same crucible was re-used as the reference crucible between all measurements.

Table 7.2. A summary of measurement parameters from Figure 7.2's XRD measurements on the qualification of experimental routines using LiF. Measurements were taken with material held a dome-style holder sealed within an Ar atmosphere glovebox.

Material	2θ domain (deg)	Sampling speed ($^\circ\,\mathrm{min}^{-1}$)	Step size ($^\circ$)	Sample mass (mg)*
As-received LiF	20 - 140	0.80	0.020	17.29
Ground LiF	20 - 140	0.80	0.020	19.30
Dehydrated LiF	20 - 140	0.80	0.020	18.99
Ni-melted LiF	20 - 140	0.80	0.020	4.54
Netzsch melted LiF	20 - 140	0.80	0.020	5.01

The following Figures 7.2, 7.3, and 7.4 and Tables 7.3, 7.4, and 7.5 are summaries of the results from the LiF qualification calendar of Figure 7.1. These figures are included prior to individual discussions on particular routine qualifications, as interpretation of the results is aided when the results from the entire qualification routine are presented together. Such results will likewise be referred to in the following Sections 7.1, 7.2, and 7.3. Figure 7.2 depicts the raw DSC signals from qualification of the experimental routine outlined in Figure 7.1. In figure 7.2, negative signals represent exothermic events throughout the four $20\,\mathrm{K\,min^{-1}}$ thermal cycles for each measurement between 750 K and 950 K. According to both Maria *et al.* and Rycerz *et al.*, it is evident that a simple peak is exhibited by all of the samples where the signals show no unique secondary or shoulder peaks [95, 100]. It is thus suggested that in all qualifying DSC measurements that the material did not pass through an off-eutectic region of multiple phases. Instead, it is more likely that with a simple DSC peak that the materials experienced either invariant melting or simple solution univariant melting by passing through a single solidus and liquidus phase boundary.

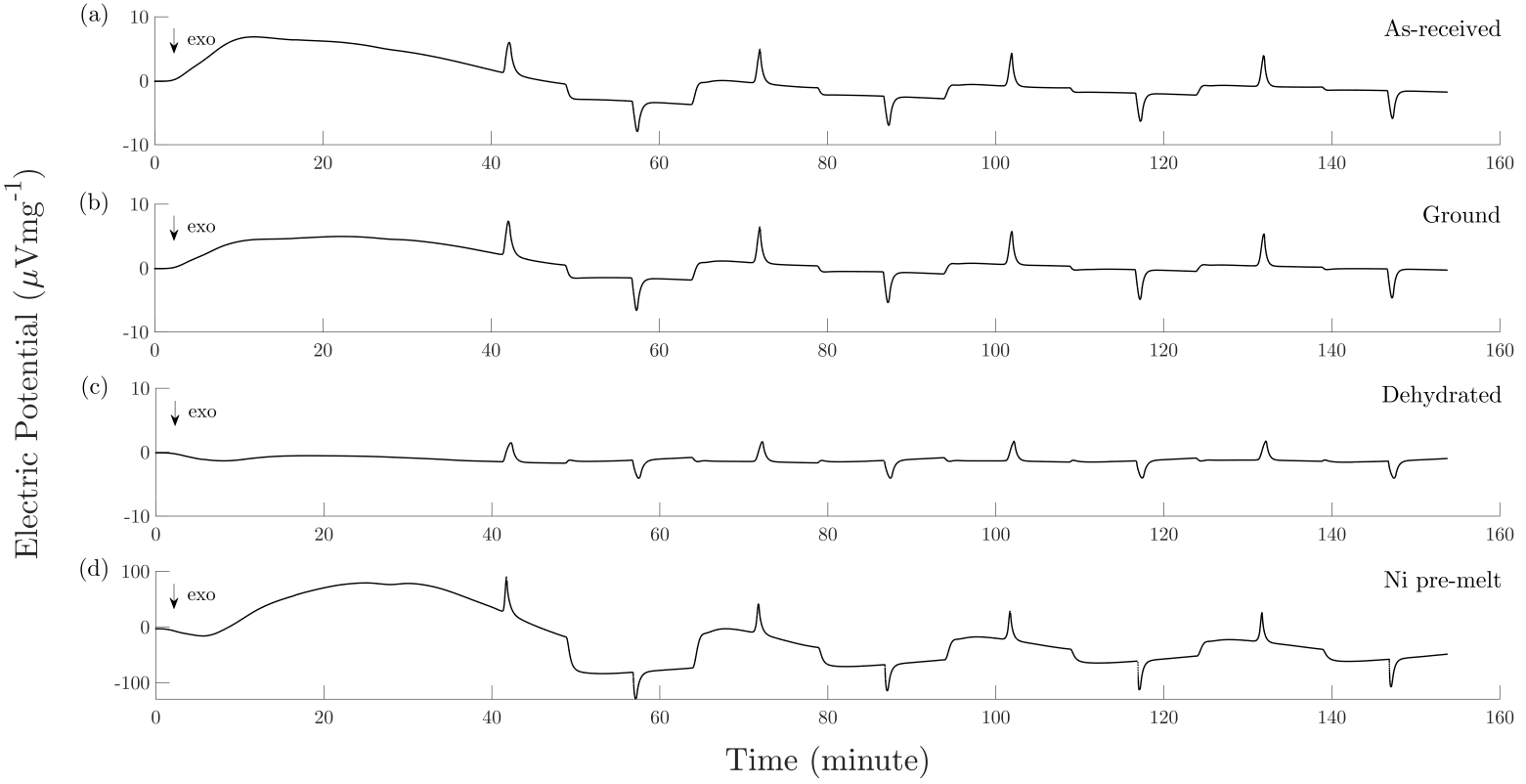

Figure 7.2. The DSC signals throughout qualification of the experimental routines according to Figure 7.1 and Table 7.1. Measurements were taken according to identical parameters over four consecutive heating and cooling ramps at $20\,\mathrm{K\,min^{-1}}$ between 750 K and 950 K, under 99.99% Argon protective gas flowing at $250\,\mathrm{mL\,min^{-1}}$. Material was sealed within an Ar filled glovebox, into new commercial Ni−Cr stainless steel high pressure crucibles with a custom Ni gasket, and measured by a Netzsch Jupiter STA 449 F1 with a type-S TG-DSC sample carrier with an Al_2O_3 spacer disc and radiation shield. A single (empty) reference crucible was re-used between all measurements. Plotted signals are depicted as (a) as-received LiF from Alfa-Aesar quoted at 99.99% purity, (b) reduced particle size LiF, (c) dehydrated LiF for 5 hours at 350 °C and (d) LiF subject to dehydration procedure, melted in the custom Ni crucible of Figure 6.5, extracted and ground in a mortar and pestle, and then subject to a DSC measurement.

Table 7.3 illustrates the temporal behaviour of the onset locations (T_{onset}^{heat} and T_{onset}^{cool}) of each peak in the consecutive ramps of the DSC signals in Figure 7.2. It is clear that by considering an error of $\pm 0.3\,^{\circ}C$, the onset temperatures for all of the heating and cooling measurements converge by the fourth ramp. Such a rate of convergence is in agreement with work by Khoklov *et al.* who record that results from DSC can generally be relied upon after the third consecutive cycle within the instrument's own error [67].

In Table 7.4, which summarizes the metrics from DSC of Figure 7.1's experimental plan, the fourth peak of each signal is therefore used in agreement with literature reports as a representative source for discussion on the DSC measurements [64,67,82,84]. Characteristic temperatures from the fourth ramp of each DSC signal in figure 7.2 have been calculated with the Netzsch Proteus software and also depicted in Figure 7.3 as a source of illustration accompanying the data in Table 7.4. Onset and endset temperatures of an energetic event (peak) during a DSC measurement were determined by associating a temperature with the location of intersection between two individual tangents from the baseline and inflection point of a peak.

Table 7.3. Onset temperatures of consecutive heating and cooling DSC peaks throughout the qualification of experimental routines on LiF. Measurements were taken according to identical parameters over four consecutive heating and cooling ramps at $20\,\mathrm{K\,min^{-1}}$ between 750 K and 950 K, under 99.99% Argon protective gas flowing at $250\,\mathrm{mL\,min^{-1}}$. Material was sealed within an Ar filled glovebox, into new commercial Ni−Cr stainless steel high pressure crucibles with a custom Ni gasket, and measured by a Netzsch Jupiter STA 449 F1 with a type-S TG-DSC sample carrier with an Al_2O_3 spacer disc and radiation shield. A single (empty) reference crucible was re-used between all measurements. A reference melting point of LiF is published by Capelli as $845.75\,^{\circ}\mathrm{C} \pm 10.00\,^{\circ}\mathrm{C}$ [29].

	Heating onset (°C)*,† : T_{onset}^{heat}				Cooling onset (°C)*,† : T_{onset}^{cool}			
Material	1^{st} ramp	2^{nd} ramp	3^{rd} ramp	4^{th} ramp	1^{st} ramp	2^{nd} ramp	3^{rd} ramp	4^{th} ramp
As-received LiF	852.0	847.0	845.9	845.9	844.5	845.9	847.1	847.4
Ground LiF	849.8	847.5	845.9	845.6	845.6	847.1	847.6	847.9
Dehydrated LiF	849.0	847.4	846.7	846.7	845.6	846.2	845.8	845.7
Ni-melted LiF	849.8	847.5	845.9	845.6	844.0	844.5	843.4	843.6

* The precision of the Netzsch Type S thermocouple is ±0.3 °C, whereas the accuracy is ±0.2 °C [152]. Due to the uncalibrated state of the measurements, interpretation of the results is only made within group (relative to the as-received state measurements) and thus the measurement precision (±0.3 °C) is taken as the error.

† Determined by tangent intersection method.

Table 7.4. Characteristics of the fourth DSC ramp's simple peak throughout qualification of the experimental routines using LiF. Measurements taken according to identical parameters over four consecutive heating and cooling ramps at $20\,\mathrm{K\,min^{-1}}$ between 750 K and 950 K, under 99.99% Argon protective gas flowing at $250\,\mathrm{mL\,min^{-1}}$. Material was sealed within an Ar filled glovebox, into new commercial Ni−Cr stainless steel high pressure crucibles with a custom Ni gasket, and measured by a Netzsch Jupiter STA 449 F1 with a type-S TG-DSC sample carrier with an Al_2O_3 spacer disc and radiation shield. A single (empty) reference crucible was re-used between all measurements. A reference melting point of LiF is published by Capelli as $845.75\,^{\circ}\mathrm{C} \pm 10.00\,^{\circ}\mathrm{C}$ [29].

Material	4^{th} Heating ramp				4^{th} Cooling ramp			
	T_{onset} (°C)*,†	T_{peak} (°C)*	T_{endset} (°C)*,†	Area ($\mu V\,mg^{-1}$)	T_{onset} (°C)*,†	T_{peak} (°C)*	T_{endset} (°C)*,†	Area ($\mu V\,mg^{-1}$)
As-received LiF	845.9	857.2	864.5	177.5 ±0.9	847.4	836.3	826.2	186.3 ±0.9
Ground LiF	845.6	857.7	863.5	195.0 ±1.0	847.9	837.3	827.3	192.5 ±0.9
Dehydrated LiF	846.7	862.3	871.1	165.2 ±0.8	845.7	833.0	820.4	169.6 ±0.8
Ni-melted LiF	845.6	853.1	858.4	1602 ±8.0	843.6	839.4	828.9	1600 ±8.0

* The precision of the Netzsch Type S thermocouple is ±0.3 °C, whereas the accuracy is ±0.2 °C [152]. Due to the uncalibrated state of the measurements, interpretation of the results is only made within group (relative to the as-received state measurements) and thus the measurement precision (±0.3 °C) is taken as the error. The systematic error (±0.2 °C) is assumed to be blocked within group.

† Determined by tangent intersection method.

‡ Positive values are endothermic, as per Figure 7.2.

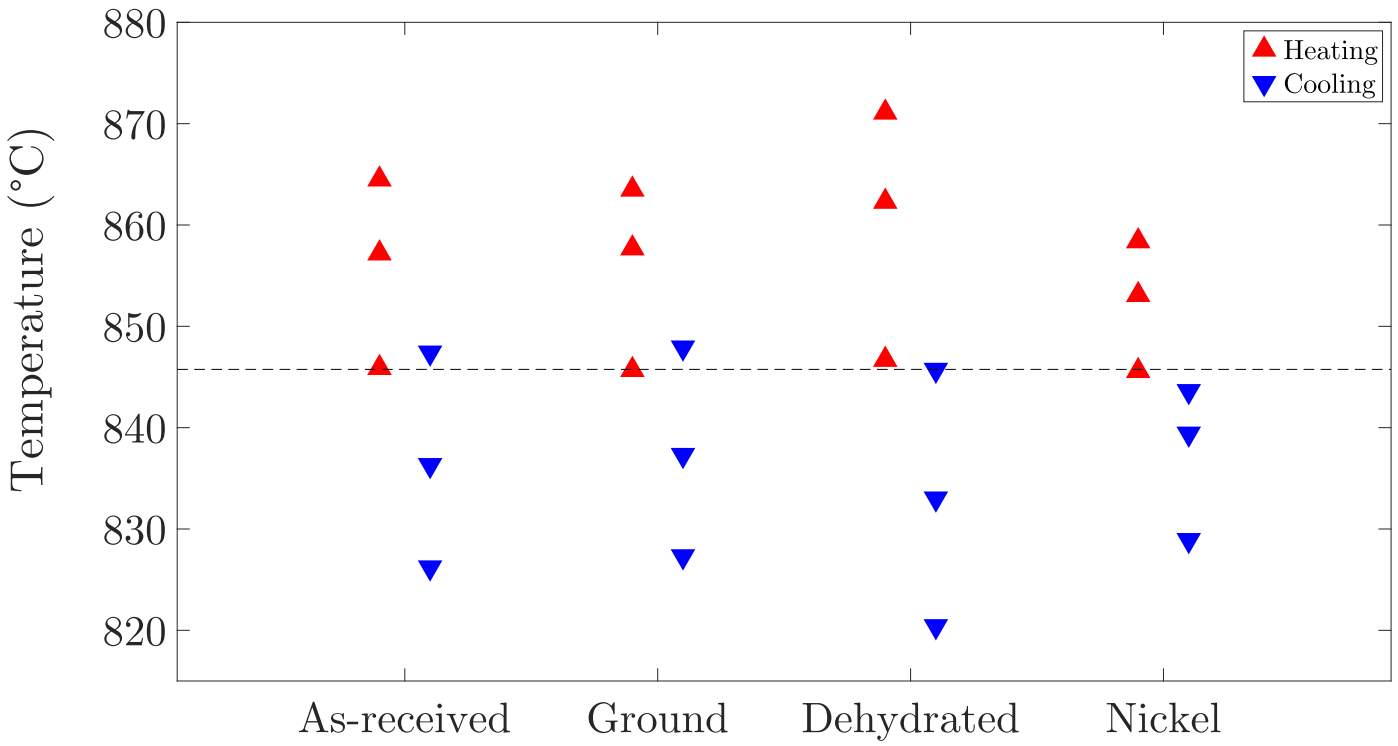

Figure 7.3. A summary of characteristics of the fourth DSC heating and cooling cycles qualifying experimental practises using LiF. Red, upward triangles represent the onset, peak, and endset temperatures of the fourth heating ramp, while blue, downward triangles represent that of the respective fourth cooling ramps. The black, dotted, horizontal line is the reference melting temperature of 845.75 °C reported by Capelli [29]. Measurements were taken according to identical parameters over four consecutive heating and cooling ramps at $20\,\mathrm{K\,min^{-1}}$ under 99.99% Argon protective gas flowing at $250\,\mathrm{mL\,min^{-1}}$. Material was sealed within an Ar filled glovebox, into new commercial Ni−Cr stainless steel high pressure crucibles with a custom Ni gasket, and measured by a Netzsch Jupiter STA 449 F1 with a type-S TG-DSC sample carrier with an Al_2O_3 spacer disc and radiation shield. A single (empty) reference crucible was re-used between all measurements.

From Table 7.4's metrics on each qualifying DSC measurement, Table 7.5 presents values of additional parameters which have been calculated for discussing the qualification of the experimental routine specifically between the measurements which were performed. In particular, the second and third columns in Table 7.5 represent two dependent approaches for calculating Rogers *et al.*'s supercooling between temperatures of the respective fourth heating and cooling ramps of Figure 7.1 [43]. As per Rogers *et al.*., and because of the restriction to within-group comparison due to the uncalibrated state of the DSC measurements, the extent of supercooling is taken as a possible insight into the purity of a material [43]. Where Rogers *et al.* define impurity constituents as nucleation sites in a liquid solution, the presence of contaminant species (or lack thereof) which exist in the solid state at the onset of solidification, and which also do not effect the final temperature of melting (invariant point or the liquidus), has been shown to alter the solidification temperature and thus the extent of supercooling of similar salt materials [43].

The difference between the two metrics for supercooling in columns two and three depend on the interpretation of the phase behaviour of the material during the DSC measurement however. If a DSC peak from Figure 7.2 represents an invariant melting event, where a single temperature defines a determined (zero degrees of freedom) equilibrium between a single liquid and single solid phase, a significant positive difference (larger than the error) between the onset temperatures of associated heating and cooling peaks ($T^{invariant}_{supercooling} = T^{heat}_{onset}$ - T^{cool}_{onset}) is taken to represent supercooling. Alternatively, if a DSC peak is interpreted as representing solution's univariant equilibrium, thermodynamic equilibrium may exist across a range of temperatures within the peak (between the solidus and liquidus), and supercooling should be calculated from the highest temperature of liquid-solid equilibrium during melting and the onset of solidification ($T^{univariant}_{supercooling} = T^{heat}_{peak}$ - T^{cool}_{onset}). It should be noted however, in the case of univariant (or *non-congruent*) melting behaviour, that the interpretation of supercooling is susceptible to sample size with the calculation dependant on the DSC

peak's maximum position.

It is well documented that peak maximum and peak endset positions are highly susceptible to sample mass and ramp rate, and therefore deductions dependent on them should be cognizant of their effect [153, 154]. In the case of supercooling, the third column in Table 7.5 may therefore be susceptible to type I errors (false positives) such that the extent of supercooling may be exaggerated for measurements with higher sample mass. Such an approach, to infer purity from the extent of supercooling, fundamentally assumes that solid impurity species are present during solidification. As such, either the impurity species may exist as individual solid particles throughout the measurement or dissolution of the impurity may only exist such that the contaminant species solidify at temperatures between the upper temperature of the measurement and the liquidus of the material (thus able to act as solid nucleation sites at the liquidus). The first behaviour lends itself to the second column of Table 7.5, whereas the second approach is related to the solution melting interpretation associated with the third column. By interpreting the DSC peaks in Figure 7.2 according to Maria *et al.* and Rycerz *et al.* et al., each peak suggests a simple melting behaviour which permits the definition of supercooling in both ways [95, 100].

One avenue considered was according to Rogers *et al.*, who surmised that a severe extent of supercooling may introduce an overwhelming energy signal which a single thermocouple DSC device cannot completely capture [43]. The change in the calculated area of the peaks during heating and cooling was therefore calculated in Tables 7.5's fifth column, to serve as a complimentary aid for interpreting the values of the univariant supercooling parameter (the third column). If confidence was evident for a clear inverse relationship between the size of the calculated invariant supercooling and the peak area depletion between associated heating and cooling peaks, one may infer that the melting of the material was experienced as a solution and not invariantly. This is evidently not the case. It is also clear that none of the processing

to LiF instigated an invariant supercooling which was larger in scale than that of any of the univariant supercooling calculations. Therefore, according to the supercooling, such a finding suggests that material does not transition from solution behaviour to pure invariant behaviour between any of the measurements (one would expect the scale of the invariant supercooling to surpass the univariant supercooling between measurements if that were the case).

The main consideration for measurement qualification that was discussed in Chapter 5 was the correlation of DSC and XRD measurements on processed LiF to those on as-received LiF. Changes in the calculated temperatures at the peak onset and peak maximum and the peak areas (normalized to sample mass) have therefore been calculated in Table 7.5 with respect to the measured values on the as-received material. Depending on the interpretation of the phase behaviour, such parameters can give insight into changes in the sample's solidus and liquidus phase boundaries along with any changes in energy associated with the melting phase change. Similarly, differing sample masses (reported in Table 7.1) can also effect the possibility of type I error in a number of these metrics, where artificial changes can be produced by differences in sample mass between one measurement sample and the next. Such an example may be evident in the fourth column in Table 7.5, where the LiF pre-melted in the Ni prototype crucible exhibits no significant change in its onset temperature (the difference being within instrument precision), however the position of the peak maximum during heating is noticeably depressed. Although phase behaviour could explain this observation by proposing the material's composition shift along a eutectic region (the onset remaining constant) and subsequently only exhibiting a changed liquidus temperature, the simple peak shape of Figure 7.2 suggests that this is not the case. Alternatively, the expected behaviour of a significantly smaller mass (apparent in Table 7.1) may explain the peak temperature depression without employing a phase or compositional interpretation.

Table 7.5. Analysis of DSC measurements throughout qualification of the experimental routines using LiF. Measurements taken according to identical parameters over four consecutive heating and cooling ramps at $20\,\mathrm{K\,min^{-1}}$ between 750 K and 950 K, under 99.99% Argon protective gas flowing at $250\,\mathrm{mL\,min^{-1}}$. Material was sealed within an Ar filled glovebox, into new commercial Ni−Cr stainless steel high pressure crucibles with a custom Ni gasket, and measured by a Netzsch Jupiter STA 449 F1 with a type-S TG-DSC-C_p sample carrier with an Al_2O_3 spacer disc and radiation shield. A single (empty) reference crucible was re-used between all measurements.

Material	$T^{\text{invariant}}_{\text{supercooling}}$ (°C)*,†	$T^{\text{univariant}}_{\text{supercooling}}$ (°C)*,‡	$\Delta T^{\text{heat}}_{\text{onset}}$ (°C)*,a	$\Delta T^{\text{heat}}_{\text{peak}}$ (°C)*,b	$\Delta\text{Area}_{\text{heat}}$ ($\mu\mathrm{V\,mg^{-1}}$)c,d	$\Delta\text{Area}_{\text{cool}}$ ($\mu\mathrm{V\,mg^{-1}}$)c,e	$\Delta\text{Area}^{\text{heat}}_{\text{cool}}$ ($\mu\mathrm{V\,mg^{-1}}$)c,f
As-received LiF	-1.5	9.8	0.0	0.0	0.0	0.0	-8.8 ±1.3
Ground LiF	-2.3	9.8	-0.3	0.5	17.5 ±1.3	-6.2 ±1.3	2.5 ±1.4
Dehydrated LiF	1.0	16.6	0.8	5.1	-12.3 ±1.2	16.7 ±1.3	-4.5 ±1.2
Ni-melted LiF	2.0	9.5	-0.3	-4.1	1424.5 ±8.1	-1413.7 ±8.1	2.0 ±11.3

* The propagated error from the precision of the Netzsch Type S thermocouple is ±0.42 °C [152].
† $T^{\text{invariant}}_{\text{supercooling}} = T^{\text{heat}}_{\text{onset}} - T^{\text{cool}}_{\text{onset}}$.
‡ $T^{\text{univariant}}_{\text{supercooling}} = T^{\text{heat}}_{\text{peak}} - T^{\text{cool}}_{\text{onset}}$.
a $\Delta T_{\text{onset}} = T^{\text{measurement}}_{\text{onset}} - T^{\text{as-received}}_{\text{onset}}$.
b $\Delta T_{\text{peak}} = T^{\text{measurement}}_{\text{peak}} - T^{\text{as-received}}_{\text{peak}}$.
c The propagated error from the precision error of the Netzsch Type S thermocouple ±0.71 $\mu\mathrm{V\,mg^{-1}}$ [152].
d $\Delta\text{Area}_{\text{heat}} = \text{Area}^{\text{measurement}}_{\text{heat}} - \text{Area}^{\text{as-received}}_{\text{heat}}$.
e $\Delta\text{Area}_{\text{cool}} = \text{Area}^{\text{measurement}}_{\text{cool}} - \text{Area}^{\text{as-received}}_{\text{cool}}$.
f $\Delta\text{Area}_{\text{cool}} = \text{Area}_{\text{heat}} - \text{Area}_{\text{cool}}$.

XRD patterns obtained by the qualification outlined in Figure 7.1 are collected in Figure 7.4. Significant peaks of each XRD pattern from Figure 7.4 were determined by the Rigaku PXRD software and are summarized and compared to a standard database reference of the LiF crystal structure in Table 7.6. Comparison of the XRD patterns in Figure 7.4 to one another is illustrated in Figure 7.5, where the differences between diffraction patterns are represented by the *residuals*. It is clear that in general, good agreement is found between most of the observed diffraction pattern peaks in qualification materials and that of the reference dataset. However, clear differences are apparent in the two samples subject to pre-melt treatments prior to XRD (extracted from Ni prototype crucible and also in the Netzsch crucible after solidification). As a result of the significant peak intensity differences present in such measurements, it is supposed that sample preparation difficulties in obtaining sufficient particle size and distribution are a reasonable explanation for this discrepancy. As a result of the relatively large sample size differences disclosed in Table 7.2, the samples of these measurements were initially measured by XRD in their solidified state immediately after pre-melting. In such a state, the material exhibited a non-trivial height above the flat surface of the XRD measurement bed and the conditions resulted in a poor XRD pattern. The material was thus subsequently rotated at 120 rpm in a second XRD measurement, however such conditions also produced the same poor result. Lastly, the material was ground in a mortar and pestle for 15 minutes and rotated at the same rate for a third XRD measurement. Such treatment of the material only produced small area coverage of the XRD sample holder and subsequently also produced an effectively equivalent diffraction pattern, Figure 7.4. The discrepancy of such XRD measurements is proposed to have occurred as a result of an inadequate representation of the sample's crystallographic orientations by grinding such a small sample size and likewise not achieving effective conditions for powder XRD.

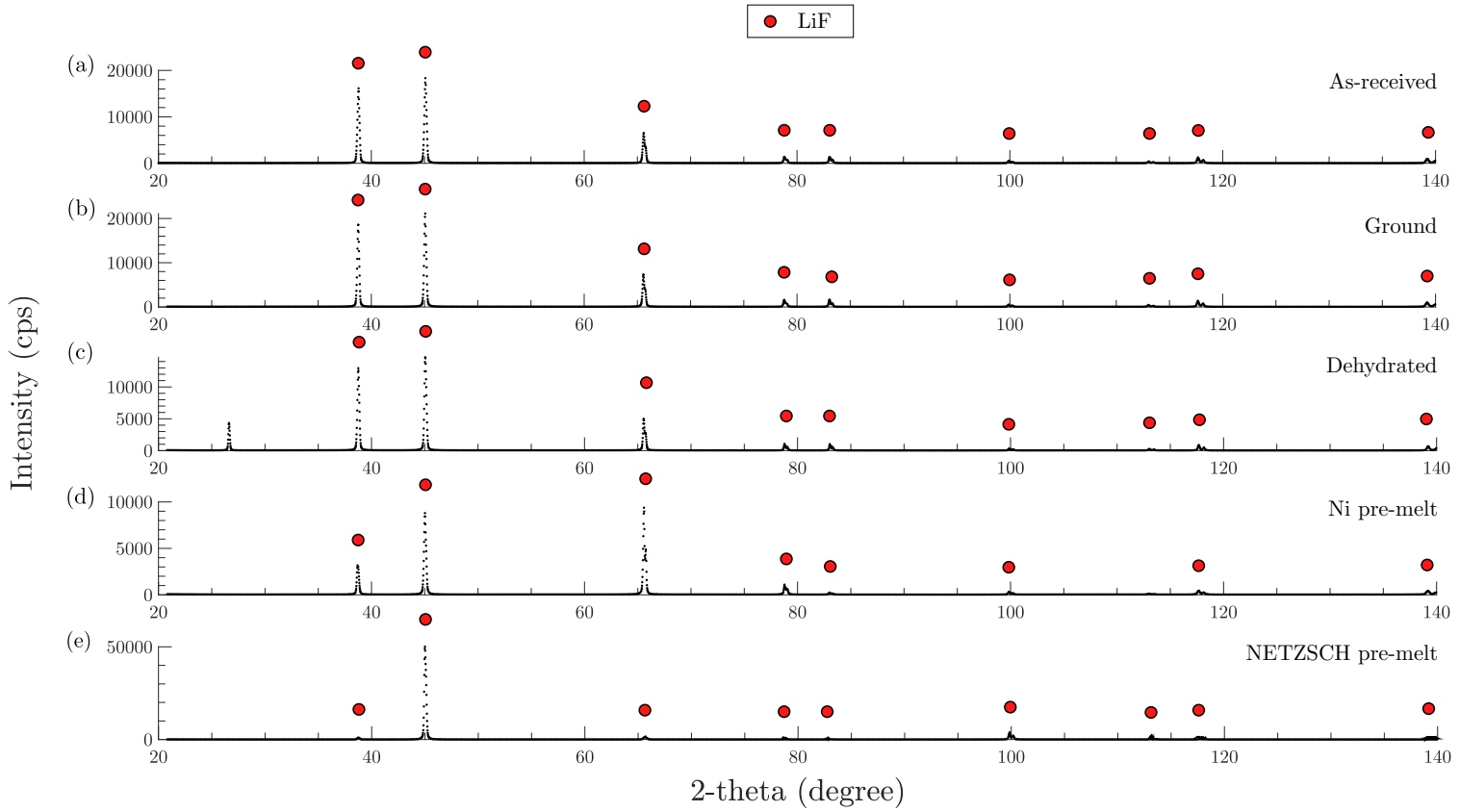

Figure 7.4. A summary of XRD measurements qualifying experimental practises using LiF (a) As-received LiF from Alfa-Aesar quoted 99.99% pure. (b) Reduced particle size LiF. (c) Dehydrated LiF for 5 hrs at 350 °C. (d) LiF dehydrated, melted in custom Ni crucible, mechanically extracted, ground in a mortar and pestle, and subject to the DSC measurement according to (c) in Figure 7.2. (e) LiF subject to DSC measurement in Netzsch crucible, mechanically extracted, and ground in a mortar and pestle. Measurements were taken with a Rigaku dome-style holder at $0.80\,^{\circ}\,\mathrm{min}^{-1}$ between 20 deg and 140 deg through a step size of 0.020°.

Table 7.6. A comparison of the XRD peaks identified by Rigaku's PXRD software relative to a LiF reference diffraction pattern[†] to investigate the potential sources compositional error throughout an experimental campaign. Measurements were taken with a Rigaku dome-style holder at $0.80\,^{\circ}\,\mathrm{min}^{-1}$ between 20 deg and 140 deg through a step size of 0.020°.

Experimental (2θ)					
As received	Ground	Dehydrated[*]	Melted in Ni	Melted in Fe−Cr	ICDD standard (2θ)[†]
		26.704			
38.794	38.762	38.759	38.676	38.774	38.70
45.078	45.049	45.040	45.011	44.986	45.00
		50.167			
65.595	65.564	65.562	65.568	65.519	65.49
				65.678	
				66.001	
78.830	78.812	78.809	78.790	78.735	78.77
		81.563			
83.076	83.055	83.054	82.990	83.032	83.00
99.921	99.889	99.888	99.856	99.847	99.83
113.052	113.037	113.035	112.989	113.077	112.97
117.700	117.671		117.664	117.734	117.61
			132.7		
	134.9				
139.235	139.234	139.218	139.198	139.18	139.13
0.797	0.989	0.282	0.633	0.911	: Figure of merit

[*] This is a second attempt at obtaining a measurement from dehydrated quantity. A first sample was decanted from the dehydrated bulk quantity but showed visible trace black impurities. Differences between both sample's XRD patterns however are negligible.

[†] Database card number: 00-004-0857.

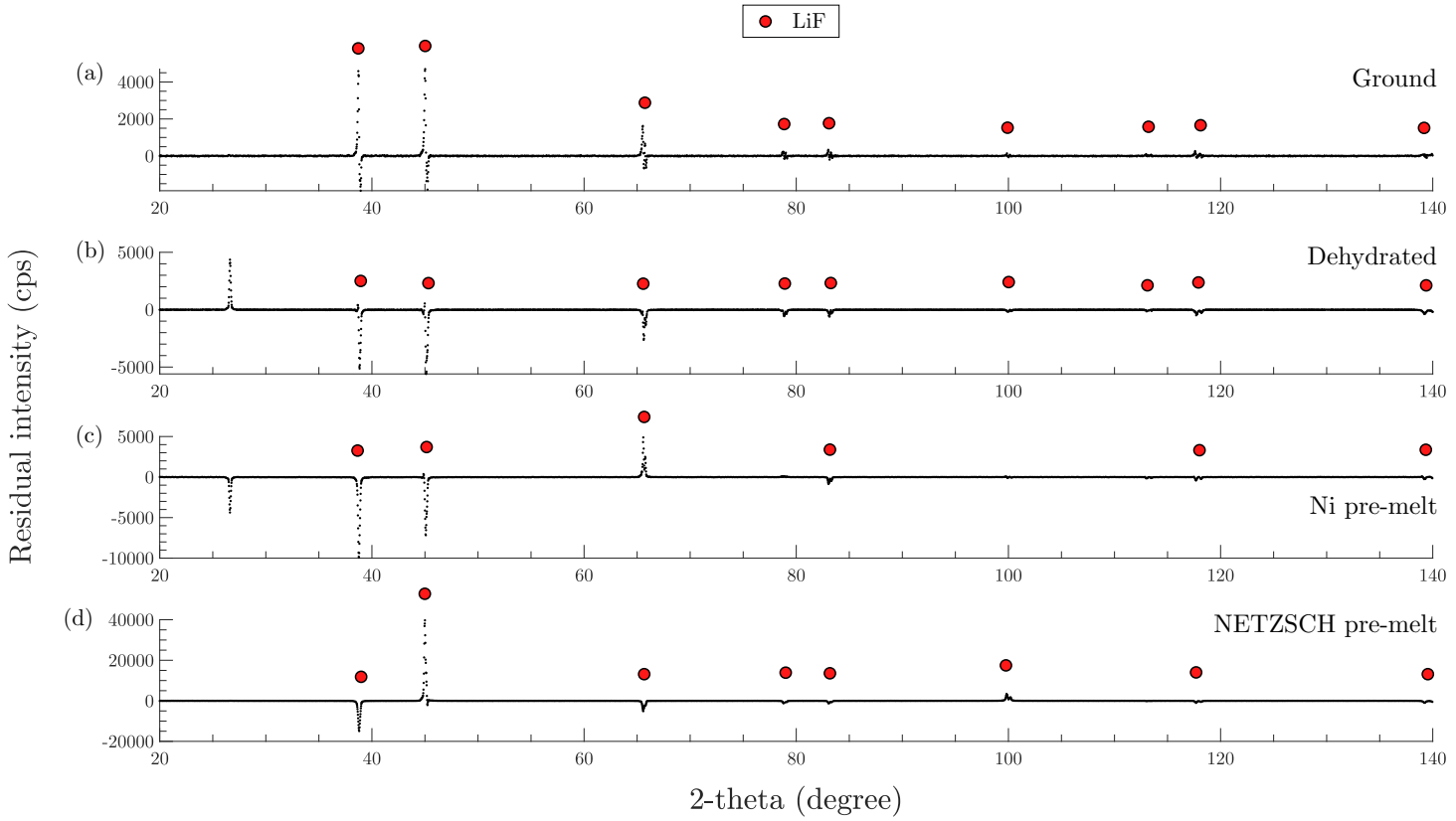

Figure 7.5. Residual XRD patterns on LiF illustrating the influence of the respective experimental procedures (a) Difference between dehydrated and as-received XRD patterns of LiF. (b) Reduced particle size LiF. (c) Dehydrated LiF for 5hrs at 350 °C. (d) LiF dehydrated, melted in custom Ni crucible, mechanically extracted, ground in a mortar and pestle, and subject to the DSC measurement as (c) in Figure 7.2. Measurements were taken with a Rigaku dome-style holder at 0.80 ° min^{-1} between 20 deg and 140 deg through a step size of 0.020°.

7.1 Particle Size Reduction

To aid in the success of purification, mixing, and DSC resolution itself, particle size reduction was first employed on as-received LiF. Qualification of such a procedure is concerned with two metrics: (1) the effectiveness of the technique to reduce both the average particle size and also produce a right-skew distribution of particle size and (2) the influence of the grinding procedure on compositional contamination of the salt component.

According to Figure 5.1, qualification of the particle size reduction technique first required a baseline particle size distribution to be measured of the as-received 99.99% pure (*Puratronic* grade) LiF from Alfa Aesar. However, because of the relative inexpensiveness of KNO_3, and the use of KNO_3 by Beneš *et al.* in literature, KNO_3 was used in place of LiF for the particle size measurement aspect of the particle size reduction qualification [66]. A quantity of material was thus sampled from the bulk as-received KNO_3 and subject to particle size segregation by sieve analysis. This procedure was done in strict accordance with ASTM standard B214-16, except that a sample size of roughly 20 g was used [145]. For random sampling, the decanted materials from the as-received batch of LiF was only sampled after mixing the bulk quantity by shaking the bottle gently. Such measurement was performed according to the developed SOP in Appendix A.1. This measurement was individually repeated three times on unique sample quantities for statistical significance.

Following the baseline measurement, as received KNO_3 was ground with a cleaned mortar and pestle by hand for 15 minutes within the glovebox, as depicted in Figure 5.3. Following grinding according to the SOP in Appendix A.2, a portion of the sample was subject to the same sieve particle size analysis to determine the particle size distribution. A sample size of three was again utilized in order to construct confidence intervals for quantitative comparison between the two distributions.

According to Figure 7.6, it is clear that the grinding operation on as-received KNO_3 was successful in both reducing the average particle size and shifting the measured particle size distribution to be heavily right skewed. Furthermore, confidence was achieved according to the ASTM B214-16 standard, where the procedures were in agreement with standardized criteria for a successful measurement. Although the recovery fraction of the particle size distribution measurement did not comply with the 99.9 % cut-off according to ASTM B214-16, a highly replicable recovery fraction was achieved between all six individual measurements and was found to be $99.85\,\% \pm 0.01\,\%$ with 95 % confidence. Such a discrepancy is arguably acceptable in part due to its close value to the cut-off, and its highly replicable distribution, but also when considering the working conditions of performing such measurements within a glovebox and with a significantly reduced quantity of material than the standard amount.

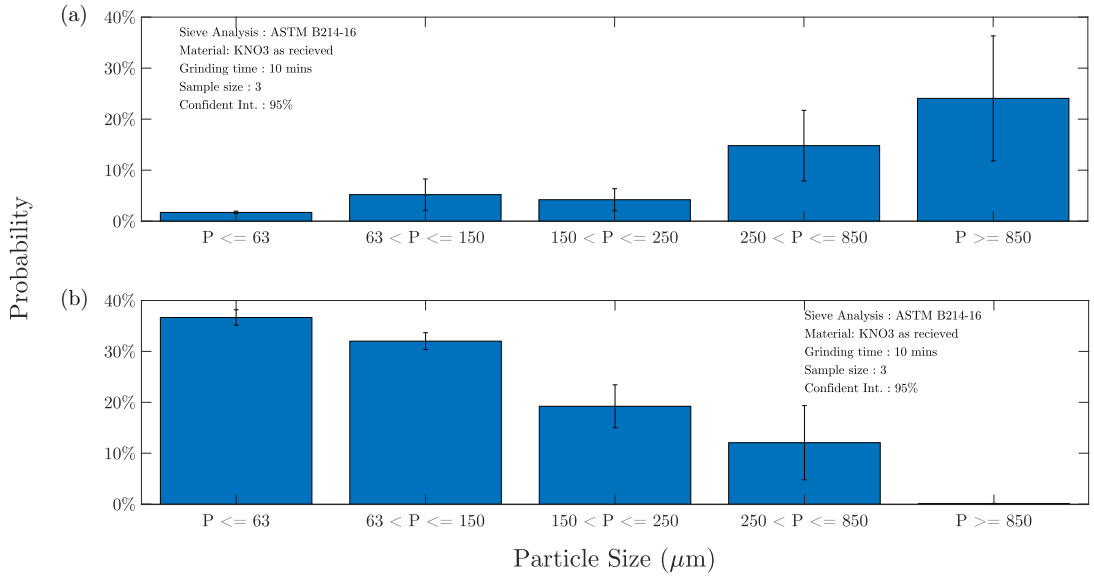

Figure 7.6. (a) Particle size distribution of as-received KNO_3. (b) Particle size distribution of KNO_3 after subject to grinding procedure in SOP of Appendix A.2 and A.1. Sample size 3 for each distribution made according to ASTM B-214-16 with recovery of 98.5%.

Following particle size distribution measurements, compositional influence of the grinding technique was qualified by investigation of the material's phase transition behaviour and crystal structure (as outlined in Figure 7.1 with the use of DSC and XRD). Prior to grinding, the melting point of the as-received LiF was measured by DSC in a Netzsch crucible without a liner. A cleaned Netzsch high pressure crucible was filled and tamped down with as-received LiF sealed within the glovebox, and DSC was conducted all according to Table 7.1. The DSC was not calibrated, however the two crucibles (filled and empty reference) were cleaned, dried, and positioned in the sample holder the same way [155]. Such conditions are similar to those employed by Johnson *et al.*, with other sources of literature, and with recommendations from Netzsch [154, 156]. It should be noted that TGA was also performed simultaneously to the DSC to evaluate the potential event of a crucible leak. No evidence of a leak was observed throughout any measurement. Additionally, the crystal structure of the as-received LiF was also measured using XRD. A cleaned dome-style holder was filled with as-received LiF within the glovebox and sealed before egress from the glovebox. When egressing from the glovebox, consideration was taken regarding the possible degradation of the holder's sealed Ar environment within the glovebox's antechamber, and thus only partial vacuums were employed to reduce this risk. The XRD measurement was taken according to Table 7.2. A written SOP was followed for the salt specific details of XRD sample handling as included in Appendix A.4. A grinding procedure was then performed on roughly 40 g of as-received LiF and identical STA and XRD measurements were made as described in Tables 7.1 and 7.2.

Figure 7.2 (a) and (b) illustrate that the two thermal analyses before and after grinding, respectively, were found to be very similar. Figure 7.2 shows that single phase transformation peaks were observed through each of the heating and cooling cycles on both as-received and ground material. In Table 7.4's summary of the extrapolated temperature characteristics from the fourth DSC peak, the two material's similarity is also evident. Measurements of the onset temperature suggest that the

ground material and as-received material exhibit identical solidus temperatures in the interpretation assuming melting isn't invariant. Considering that no temperature calibration was performed, or no heating ramp considerations were made, the slight differences in peak maximum position and endset temperature are also minimal. The depression of the endset temperature after grinding is also in agreement with the smaller mass of the sample disclosed in Table 7.1. By taking the onset of a DSC peak to represent the melting point of the sample, Table 7.4 reports that deduced melting points of the two samples are the same insignificant distance (0.15 °C) from the reference value of 845.75 °C from Capelli and within precision error of the instrument [29]. Table 7.4 also describes that according to invariant supercooling the grinding process has no improvement to inducing supercooling in the material. If instead, the thermal analyses is conducted in a non-invariant frame of reference, this found phenomena would be more physical. Interpreting the onset of heating to be the solidus transition and the onset of cooling to be the liquidus, one may expect the liquidus found by cooling curves to be above the solidus determined from heating (without significant supercooling). Furthermore, in such an interpretation it is also common to interpret the heating peak as an indication of the solidus point which is un-effected by phenomena such as supercooling. As such, the heating peak liquidus would be expected to be found at higher temperatures than those found by the onset of cooling curves which may be influenced by supercooling. Such an environment is in fact reflected by both sets of measured data in Table 7.4 and is not unreasonable given that both measurements were not subject to any form of purification and could have formed a solution with impurity species.

Figure 7.4 (a) and (b) illustrate that the XRD measurements on both as-received and ground samples of LiF also show very similar observations. No significant contamination causing a change in crystal structure is found to occur by the process of mortar and pestle grinding. Similarities between measured crystal structures are also apparent in Figure 7.5, which depicts that difference between the two patterns

and identifies zero additional diffraction peaks which cannot be attributed to LiF according to diffraction reference card number DB: 00-004-0857. The major conclusion drawn from the XRD pattern of as-received LiF is that Table 7.6 suggests that no impurities exist in the as-received stock significant enough to alter the diffraction pattern beyond the identifiable reference peaks. It should be noted that the calculated figure of merit and some of the additional peaks in Table 7.6 are questionable, as the addition or subtraction of peaks in the table is not represented by the produced diffraction pattern in Figure 7.4.

7.2 Purification

Qualification of the dehydration technique for non-actinoid fluoride salts began by subjecting 100 mg of as-received LiF to the dehydration procedure developed in the SOP of Appendix A.3. Heating the sample to a desired temperature however required that the equipment be characterized first. As such, The hotplate and sand bath configuration were subject to a number of heat treatments, where a thermocouple was used to identify the difference between the set hot plate temperature and the actual temperature of the sand. Understanding the temporal and thermal behaviour of the dehydration procedure, Figure 7.7 provided an accurate and replicable benchmark to confidently achieve the desired heat treatment of the sample salt during subsequent purification.

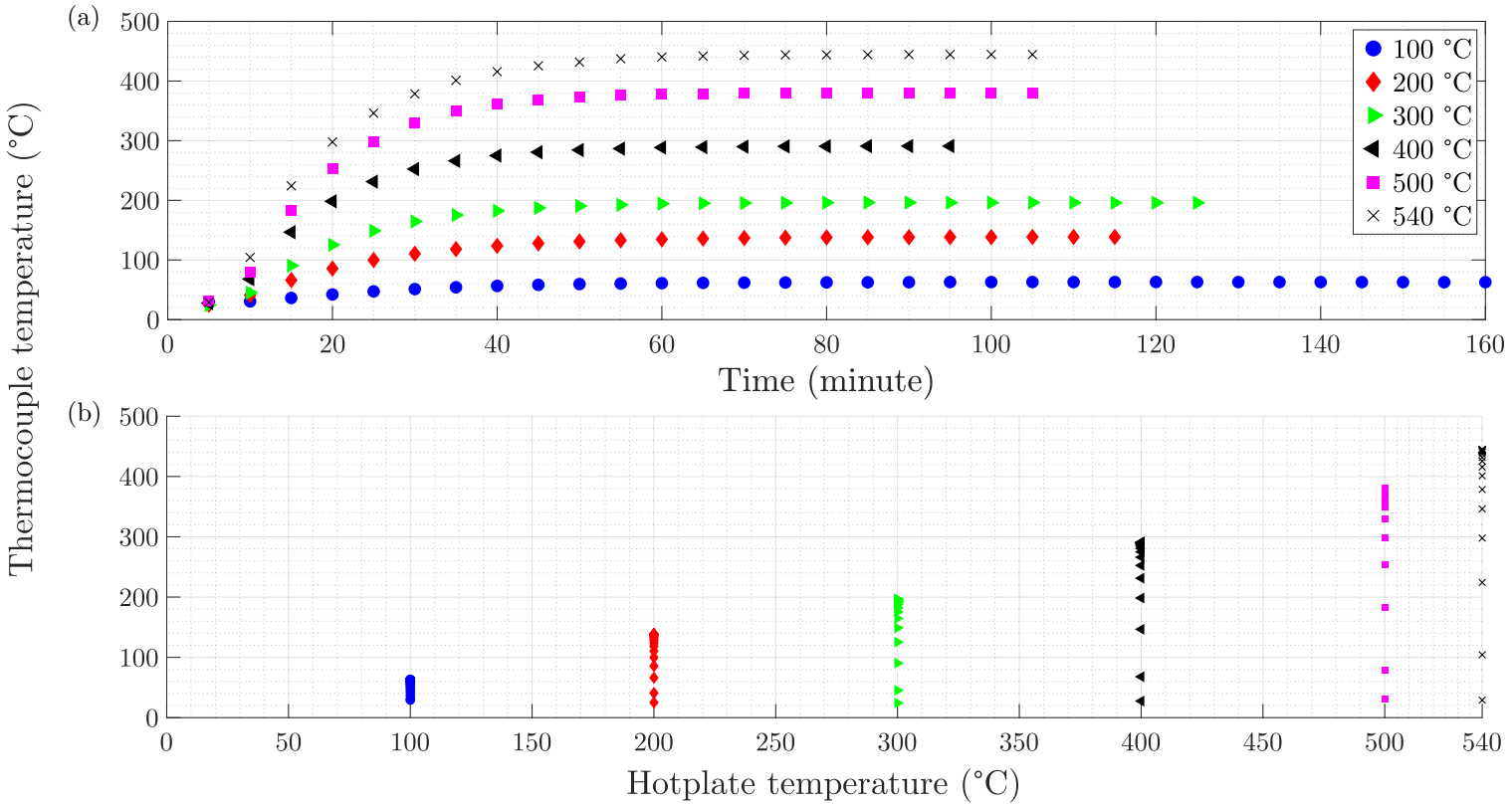

Figure 7.7. (a) Temporal characterization of the hotplate setup used for dehydration and fluorination procedures for purifying salt materials. (b) Thermal characterization of the hotplate setup used for dehydration and fluorination procedures for purifying salt materials.

Following characterization of the dehydration environment, as-received LiF was then subject to the dehydration procedure in the glovebox at 350 °C for 5 hours in a nickel reaction vessel according to the SOP in Appendix A.3 and as show in Figure 5.4. With a quantity of heat-treated LiF, DSC and XRD measurements were then conducted according to identical conditions used to obtain the measurements on as-received LiF described in Section 7.1, described in Tables 7.1 and 7.2. Comparing the thermal analyses of dehydrated sample with as-received sample, Figure 7.2 suggests again a very similar behaviour between the two measurements: a simple endothermic peak during melting with little shoulder and no secondary peaks. The one characteristic that Figure 7.2 does identify is the severely reduced jump in signal between the heating and cooling curves of Figure 7.2 (c), the background sensible energy sections between peaks are relatively flat compared to the as-received sample in Figure 7.2 (a). Such behaviour is of little quantifiable interest to the material's phase change in the measurement however, as the transition behaviour is dependant on a number of experimental parameters and occurs throughout the baseline of the measurement within an area of the thermal routine most likely to experience transients unrelated to thermodynamics.

Table 7.4 defines the characteristic temperatures deduced from the STA curves of Figure 7.2 (a) and (c). Coupled with the graphical representation of Figure 7.3, an interesting behaviour is found in the relationship between the onset temperatures of the heating and cooling curves. Firstly, the onset temperature from the heating ramp is found to be further away from Capelli's reference value than that observed for as-received material Figure 7.3. Such a behaviour may suggest that the dehydration procedure in fact made the purity worse, however as discussed, the measurement was not calibrated so comparison to a reference value is challenged. Alternatively, it is suggested in Table 7.5, that in comparison to the as-received and ground samples, LiF subject to the dehydrated procedure exhibits a cooling onset which is supercooled relative to the onset of its heating curve. If the extent of supercooling is taken as a

measure of purity as proposed by Rogers *et al.* [43], this would suggest that the dehydration procedure resulted in a reduction in the influence of potential nucleation impurities. Irrespective of an invariant or solution phase behaviour throughout melting this behaviour stands.

The univariant definition of supercooling in Table 7.5 highlights that the material subject to the dehydration routine experiences both a significantly large supercooling driving force and a relatively larger extent of supercooling compared to the other materials. In such a case one may expect that the difference between the areas of the heating and cooling peaks be most significant (and negative) for the dehydrated measurement. The change in the calculated area of the peaks during heating and cooling were therefore calculated as Tables 7.5's fifth column, which in fact shows that, despite the severe univariant supercooling of dehydrated material, the DSC was not overwhelmed with the quick release of exothermic energy from solidification. Although such an approach is not a robust argument for univariant behaviour (given that the measurement capability of the Netzsch STA Jupiter 449 F1 is unknown), it does not disprove the inherent idea that dehydration should result in a pure material demonstrating melting univariant behaviour. It should be noted however, that the larger sample mass recorded in Table 7.1 contributes to type I error in any conclusions drawn on the DSC measurement's supercooling. According to literature, the artificially larger sample mass of the LiF subject to dehydration is expected to increase the peak maximum temperature of the DSC signal, which is in fact found in Table 7.5. Likewise, the increase in the extent of supercooling depicted in Table 7.5 cannot be taken with the utmost confidence without qualitatively knowing the sensitivity of the DSC signal on sample mass.

The XRD measurement of dehydrated LiF shown in Figure 7.4 (c) however suggests that an additional peak at 26.704° was observed. Such a conclusion is also in agreement with the software calculated peaks shown in Table 7.6. An attempt to de-

termine the crystallographic source of the additional peak was made through a manual and automatic search of the XRD software, however an affiliated compound remains unknown. This difference in XRD patterns is interesting in that it aligns with the same trend in Table 7.5's onset temperatures from DSC. There is a question regarding the relation between the fact that the LiF which was subject to the dehydrated routine is shown to be the only DSC measurement exhibiting a significant change in onset temperature and also the only measurement providing an additional significant peak from XRD.

The purification of actinoid fluoride salts also employed the characterized hotplate infrastructure within the glovebox, as a stacked set of Ni reaction vessels was subject to a pair of heat-treatments (described in Section 5.3 with Figure 5.5). Assuming a 1.0% ThO_2 impurity level in as-received ThF_4, a molar ratio of roughly 5.2:1 (NH_4HF_2:ThO_2) was mixed and subject to 250 °C for 12 hours. Following this fluorination procedure, a second heat-treatment was conducted on the remaining sample in the reaction vessel at 350 °C for 5 hours.

The XRD diffraction patterns from as-received and purified ThF_4 shown in Figure 7.8 suggest that the purification did not significantly alter the observable crystallographic structure. By investigating the residual XRD measurements, Figure 7.9 demonstrates that the difference between the as-received and purified ThF_4 measurements exists predominantly in two regions: (1) around 20° and 28°, and (2) around 42° and 48°, the regions of highest peak density when investigating for potential contaminant peaks. In Figure 7.9, only slight differences in peak positions are clear between the two sample of materials, where the differences in diffraction patterns are only found to exist at effectively the same angle (signifying just a chance in peak strength). After purification however, the peaks around the 42° and 48° domain appear to be less resolved. Unfortunately, due to the radioactive nature of the material, higher resolution scans in this area were not completed with restrictions on labora-

tory time and feasibility. For both XRD patterns, the relation of measured peaks to a reference standard ThF_4 (DB: 00-017-0945) was assessed as evident by the red dots in Figure 7.8. Between the reference database card of the XRD software and the ThF_4 diffraction patterns published by Che at al. and Capelli, both measured patterns are found to suggest the presence of pure ThF_4, with the exception of a peak at 28.23° [29, 81]. Common impurity peaks were assessed from literature sources and no theorized peaks which could be identified with confidence. Other than the peak at 28.23° the XRD insights into the as-received purity of ThF_4 suggest that quantity was procured in a highly pure state.

Table 7.7. A summary of measurement parameters from Figure 7.2's XRD measurements on the qualification of the actinoid purification procedure using ThF_4, outlined in Chapter 5.3. Measurements were taken with material held a dome-style holder sealed within an Ar atmosphere glovebox.

Material	2θ domain	Sampling speed ($^\circ\,min^{-1}$)	Step size (°)	Sample mass (mg)
As-received LiF	10 - 90	0.80	0.020	11.02
Purified LiF	10 - 90	0.80	0.020	12.08

Initially, a literature scan of Che *et al.*'s paper suggests that a similar peak to the anomaly at 28.23° may exist due to the presence of $ThOF_2$, which Che *et al.* report to having a peak at 28.39° [81]. Relative to the material which was subject to mixing with NH_4HF_2, literature reports that such a product would be expected as a result of the immediate heating of the $ThOF_2$ and NH_4HF_2 [81]. However, the presence of the 28.39° in the as-received material challenges this conclusion. A manual search for related compounds was thus performed, which was initially focused on the compounds investigated by Che *et al.* including ThO_2, $(NH_4)_4ThF_8$, and $(NH_4)_3ThF_7$. However the same argument was made, where the presence of the peak in the as-received state suggests that the peak was not a product of the purification procedure. Confidence can be made in suggesting that the ThO_2, $(NH_4)_4ThF_8$, and $(NH_4)_3ThF_7$ probably do not exist in a significant quantity within either samples based on their standard

diffraction data. Otherwise, the most likely explanation for the 28.39° peak is an as-received contaminant in some form which does not react easily with NH_4HF_2 or is not driven off by temperatures of 350 °C.

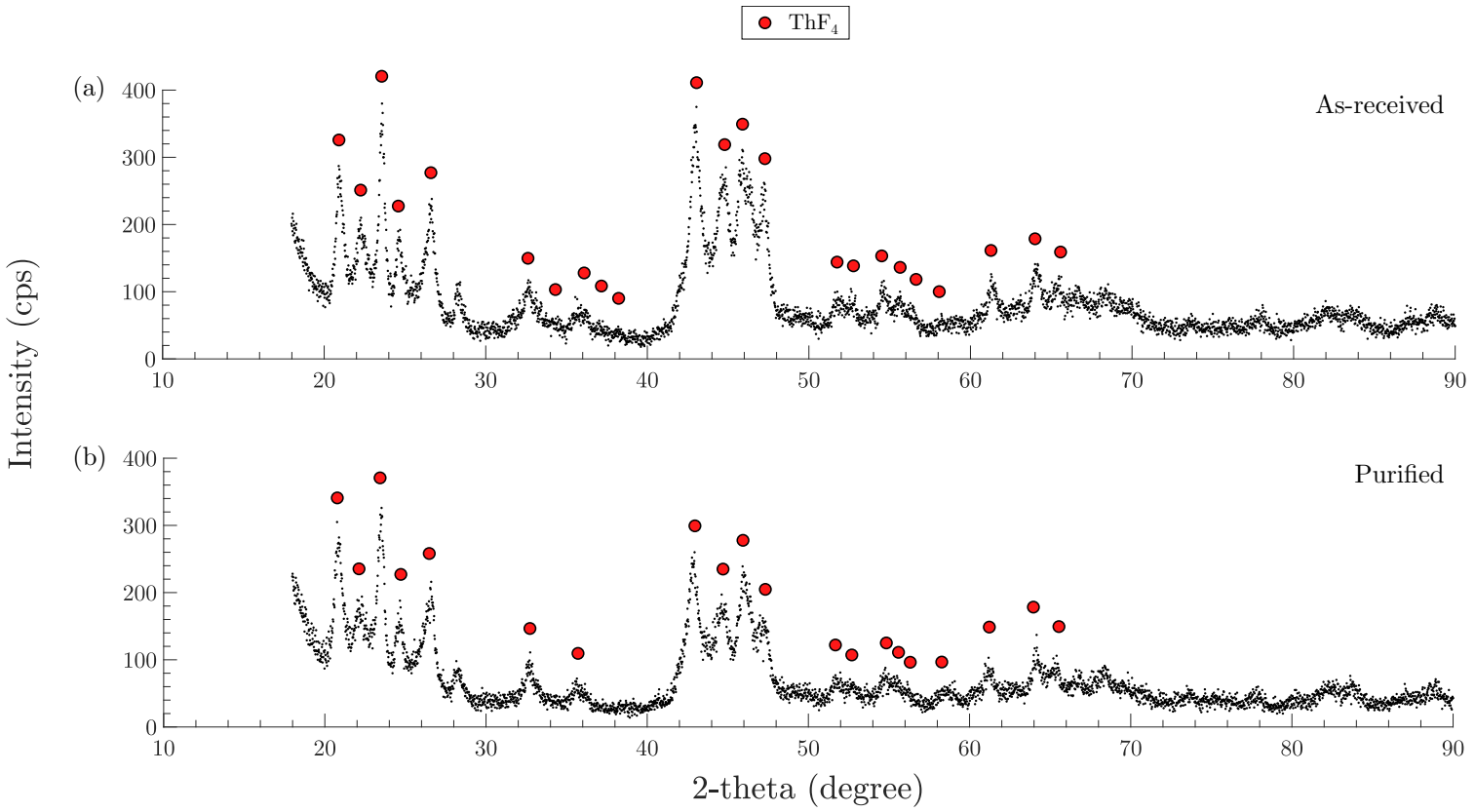

Figure 7.8. A summary of XRD measurements on ThF_4 qualifying the purification technique using NH_4HF_2 (a) As-received ThF_4 from IBI-Labs quoted 99.95% pure. (b) ThF_4 subject to the purification technique with NH_4HF_2. Measurements were taken with a Rigaku dome-style holder at $0.80\,^\circ\,\mathrm{min}^{-1}$ between 10 deg and 90 deg through a step size of 0.020°.

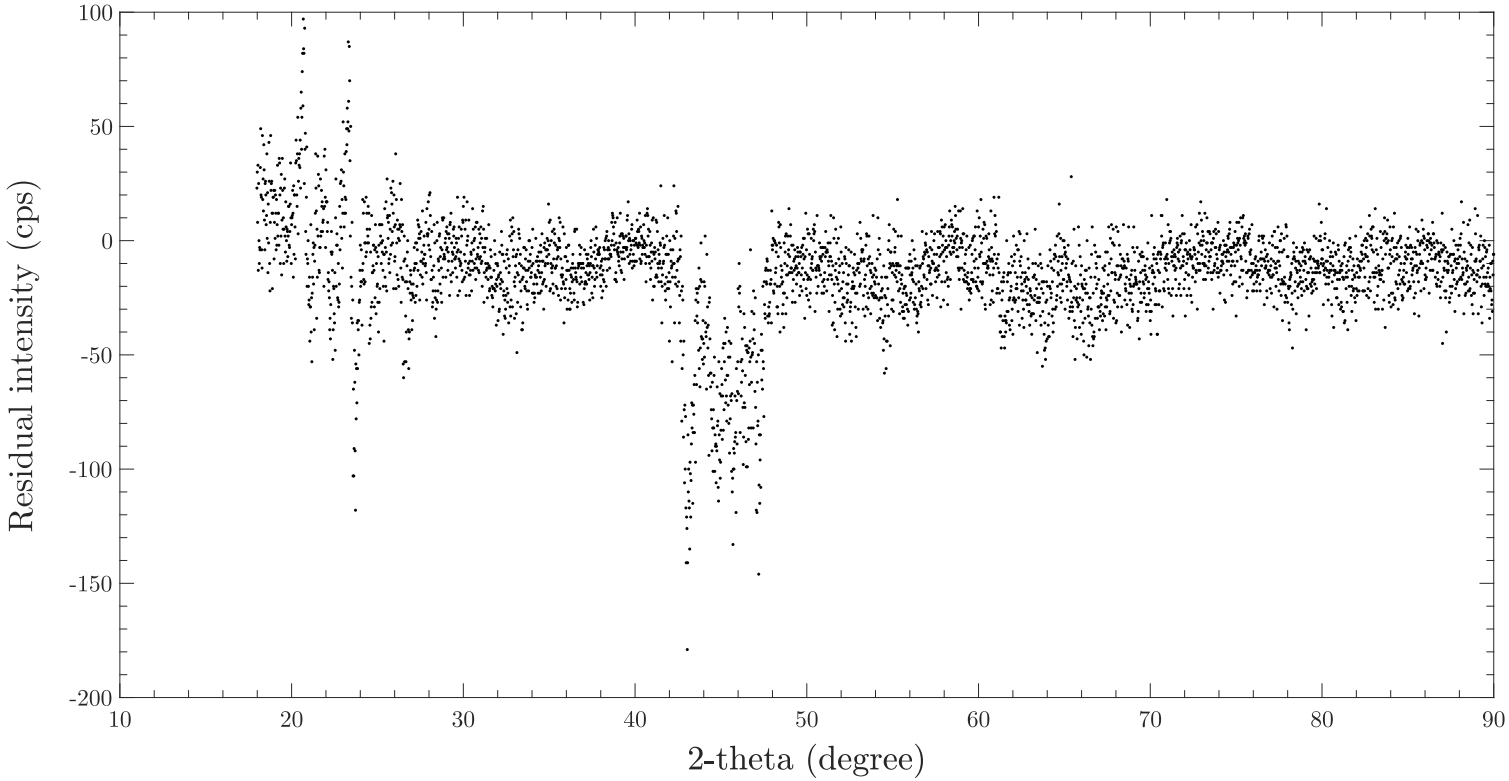

Figure 7.9. Residual XRD patterns of ThF_4 illustrating the observed difference between as-received material and that which was subject to the purification procedure with NH_4HF_2. Measurements were taken with a Rigaku dome-style holder at $0.80\,^{\circ}\,\mathrm{min}^{-1}$ between 10 deg and 90 deg through a step size of 0.020°.

7.3 Crucible Material Interaction

Despite the inability to employ the fabricated Ni prototype of the custom crucible design for DSC measurements, a qualification effort was still performed with use of the commercially available Netzsch high pressure crucibles. However, by melting LiF in the Ni prototype crucible, material could be mechanically extracted once it solidified and used as sample quantities in DSC and XRD measurements to explore the interaction of the LiF with Ni during conditions representative of a typical DSC measurement.

Before using the Netzsch STA 449 F1 Jupiter TGA to melt the LiF in an inert ar environment around the custom crucible, an identical test was performed in an open environment box furnace to ensure that the structural integrity of the crucible could withstand the temperatures and vapour pressure of molten LiF. Ramping at a rate of 15 °C min^{-1} to 1100 °C, Figure 7.10 shows that the Ni crucible remained intact for the full 2 hour heat-treatment and showed no signs of mechanical degradation. Considering that such a conclusion was made under the oxidizing environment of air, this qualification provided confidence in using the TGA to provide an Ar environment for melting LiF in a custom crucible.

Following the high temperature screening of the LiF filled custom Ni crucible, a second Ni prototype crucible was filled with dehydrated LiF in the glovebox and subject to 1000 °C for 2 hours in an Ar environment using the TGA. Dehydrated LiF was used as a material to provide as realistic material compositions for the study of wall-salt interactions as possible according to Figure 7.1. Following heat-treatment, the Ni crucible was opened within the glovebox and its solidified contents were ground with a mortar and pestle to obtain a powder for improved resolution in an XRD measurement. Crushed material was then analyzed for its melting point and crystallographic structure by DSC and XRD according to the conditions published in Tables 7.1 and

7.2 respectively.

Figure 7.10. The custom Ni crucible after subject to 1100 °C for 2 hours in air while filled with dehydrated LiF according to Figure 7.1.

The behaviour of the DSC signal from the dehydrated LiF which was pre-melted in Ni is depicted in Figure 7.2 (d). Figure 7.2 illustrates the thermal analyses onset, peak, and endset temperatures measured from the DSC signal, and suggests that the potential for Ni wall-salt interactions is low after comparing such metrics to the dehydrated and as-received measurements in Table 7.4. Although Table 7.5 identifies that the onset temperature of the heating peak is lower than that of the purely dehydrated measurement, the value actually more closely resembles that of the 845.75 °C reference melting point from Capelli [29]. More appropriately (due to the uncalibrated measurement), the behaviour of invariant supercooling is consistent with the dehydrated sample, such that the onset temperature from cooling is lower than that found during heating. However, when considering that the material may be melting non-trivially in a solution, Table 7.5 illustrates that the univariant supercooling suggests that the pre-melting in Ni restores the extent of supercooling to the same degree after before

dehydration. It should be considered however that that the peak temperatures reported in Table 7.5 exhibit the predicted temperature depression which is reported by Netzsch as a result of a smaller sample size than the dehydrated measurement and likewise a reduction of the univariant supercooling [154].

A significant effect measured with DSC on the LiF pre-melted in the Ni crucible is a larger peak area, evident in Table 7.5. With a particular energy released or absorbed during thermal events in the DSC signal of Figure 7.2, Table 7.1 supports the drastically larger peak area as a result of the smaller sample size relative to the other qualification measurements. Figure 7.2 shows that the signal from pre-melted LiF in nickel is approximately an order of magnitude larger than the other measurements, in agreement with the approximate scale of the difference in sample mass. Such a result is not intuitive given that one may expect the (non-normalized) peak area to be proportional to the sample size, all other conditions equivalent. Thus, with the sample size normalization of the signal producing a significantly different peak area, a physical phenomena cannot be ruled out. However, by considering other effects such as supercooling, peak onset and peak maximum temperatures, baseline DSC signals, and XRD observations (to be discussed further), no additional arguments support this behaviour.

The XRD measurement of the LiF that was pre-melted in Ni is illustrated in Figure 7.4. Despite resolution degradations as a result of a small quantity of pre-melted material, Figure 7.4 suggests that there is little evidence supporting significant material interaction between the LiF and Ni, in agreement with the DSC findings other than signal area. However, an interesting product of Figure 7.4 is the disappearance of the 26.704° peak that was discussed in Section 7.2 regarding the dehydrated measurement in Figure 7.4 (b). Such an observation would agree with the extent of univariant supercooling, and also the onset temperature of Table 7.5, which suggest the pre-melting in Ni returns the sample to behaving similar to the pre-dehydration

state. Disregarding the difficulties in obtaining a satisfactory particle representation, the disappearance of the 26.704° peak after melting the dehydrated LiF suggests that possibly the higher temperature experienced during ramp to the the molten state drove an impurity out of the sample, or the molten state itself provided an opportunity to achieve a higher purity.

Optical microscopy was also performed on the cross-section of the custom Ni crucible, which was used for the subsequent DSC measurement. Following ASTM standard E407, samples were wet polished by hand to 1200 grit using silicon carbide sand paper and immersion etched for 20 seconds with a solution of 20%HNO_3 - 80%HCl (by volume, etchant number 147) [157]. Figure 7.11 is an optical micrograph of the inner salt facing wall of the Ni crucible, whereas Figure 7.12 is of the bottom floor of the crucible.

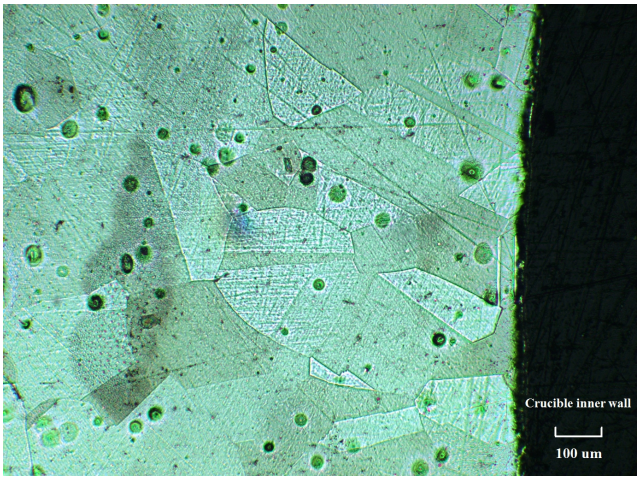

Figure 7.11. An optical micrograph of a cross section of the wall of the custom Ni crucible used to melt dehydrated LiF for DSC and DSC. ASTM E407 20%HNO_3 - 80%HCl (volume) etchant number 147 used. The micrograph was used to investigate the wall-salt interactions after melting LiF inside the crucible for 2 hours.

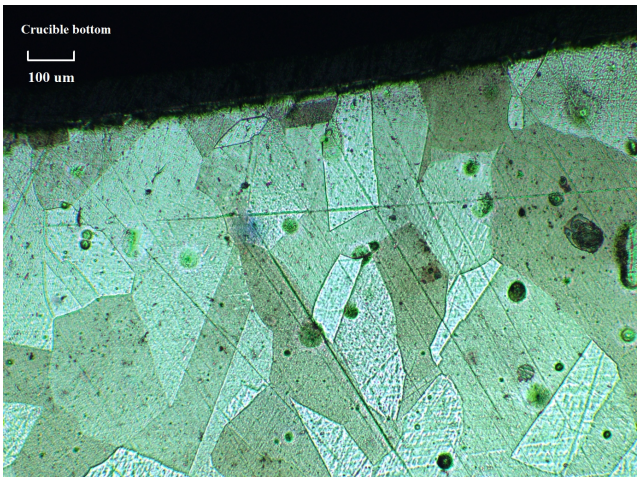

Figure 7.12. An optical micrograph of a cross section of the floor of the custom Ni crucible used to melt dehydrated LiF for DSC and DSC. ASTM E407 20%HNO_3 - 80%HCl (volume) etchant number 147 used. The micrograph was used to investigate potential material interactions after melting LiF inside the crucible for 2 hours.

Lastly, the interaction of the commercial Netzsch Ni−Cr alloy was investigated by use of optical microscopy and XRD, as outlined in Figure 7.1. Immediately following the DSC measurement of as-received LiF, the crucible was opened within the glovebox and the solidified sample was mechanically removed. The solid LiF was then ground with a mortar and pestle in the same manner as the material melted and extracted from the Ni crucible. An XRD measurement was performed according to identical experimental parameters of all other LiF XRD scans and is included in Figures 7.4 and 7.5.

An XRD measurement to qualify the material interactions of the commercial Ni−Cr crucible was particularly important because the DSC measurements that were made with them were uncalibrated. Comparing the similiar XRD patterns between the as-received sample of LiF and that of one which was subject to a full DSC measurement provides an insight into the compositional error in all other DSC results from a Netzsch crucible. Observing the small difference between Figure 7.4 (a) and (e) helps differentiate the small compositional sources of error from those induced from a lack of calibration and provide greater confidence in the interpretation and comparison

between other DSC results in Figure 7.4.

The crucible used to perform the DSC measurement on as-received LiF was then cross sectioned (Figure 7.13), polished, and etched identical to the custom Ni crucibles. Figures 7.14 and 7.15 are the wall and floor micrographs of the Ni−Cr alloy crucible after four consectutive thermal ramps between 700 °C and 1000 °C with dehydrated LiF.

Figure 7.13. The commercial Netzsch high pressure crucible outfitted with a custom Ni gasket in the lid after subject to the as-received LiF DSC measurement. During the measurement, the crucible experienced four thermal cycles from 700 °C to 1000 °C at 20 °C min^{-1} in Ar.

(a) 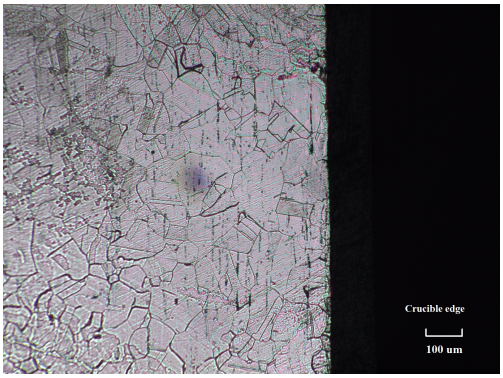

(b) 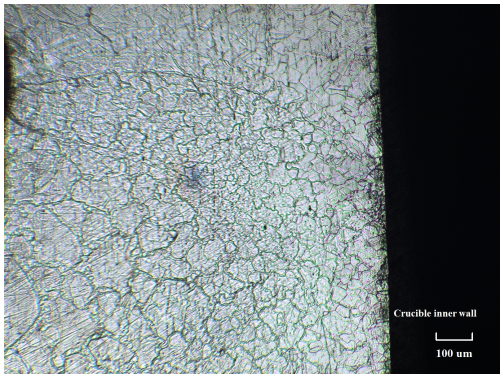

Figure 7.14. An optical micrograph of a cross section of both sides ((a) and (b)) of the walls of the commercial Netzsch crucible used for DSC of dehydrated LiF from Section 5.3. ASTM E407 20%HNO_3 - 80%HCl (volume) etchant number 147 used. The micrographs were used to investigate potential material interactions after a DSC measurement of LiF.

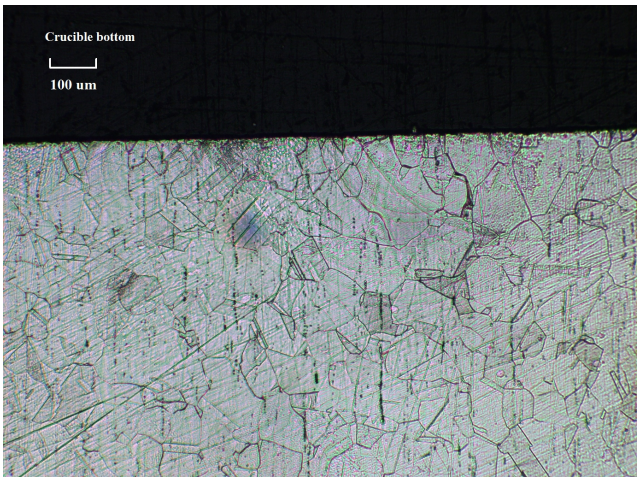

Figure 7.15. An optical micrograph of a cross section of the floor of the commercial Netzsch crucible used for DSC of dehydrated LiF from Section 5.3. ASTM E407 20%HNO_3 - 80%HCl (volume) etchant number 147 used. The micrograph was used to investigate potential material interactions after a DSC measurement of LiF.

It is clear that relative to the micrographs of the Ni crucible, one side wall of the commercially available Ni−Cr crucible appears to be damaged to a small extent, roughly to 10 µm in depth from the wall-salt interface. However, as suggested by the DSC and XRD results, the crucible induced source of compositional error is seemingly insignificant. Micrographs focused on the performance of the custom Ni gasket within the Netzsch crucible have also been made. Figure 7.16 (a) shows how the

gasket remained intact over top of the hole in the lid of the crucible, while (b) shows success of the crimping of the gasket between the lid and the body. Such confidence in the Netzsch high pressure crucibles' ability to maintain a hermetic with an in-house Ni gasket agrees with observed STA behaviour which showed no leaking during all reported DSC measurements.

(a) (b)

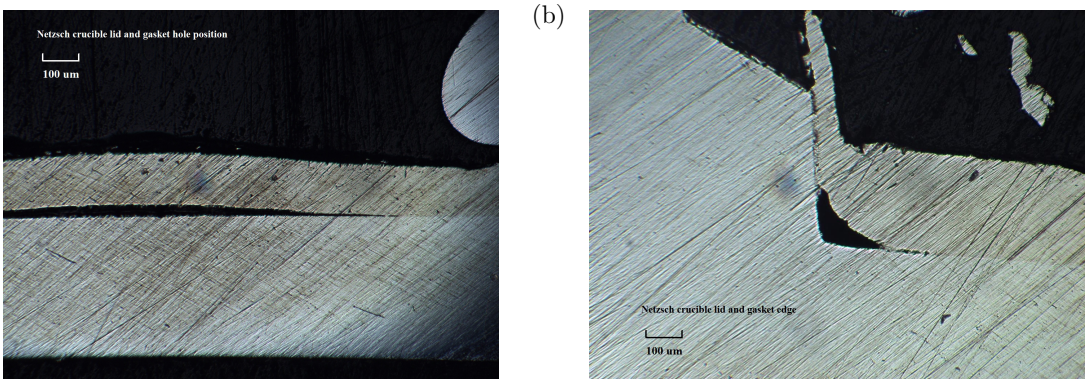

Figure 7.16. (a) An optical micrograph of the in-house made Ni gasket within a used Netzsch high pressure crucible. The separation is around the area of the hole in the lid, however the gasket remained intact without being comprimised. (b) An optical micrograph of the crimping of the in-house made Ni gasket within a used Netzsch high pressure crucible.

CHAPTER 8

Conclusions

The requirements and conditions considered in fuel behaviour of an MSR are vastly different than the mature understanding of solid fuelled reactors. It is therefore important for the community to develop a comprehensive thermodynamic understanding of fluoride fuel salt to be able to predict the fuel's material properties such as its melting point, solubility, heat capacity, and phase stability. However, practical complications exist in the handling and replicability of studying fluoride salt materials and challenge the use of commercially available devices and standard techniques.

An in-house framework for performing thermodynamic measurements was developed within the NFMG, which included particle size reduction, purification, component mixing, and DSC measurements themselves. SOPs were developed in an attempt to improve the replicability, quality, and understanding of salt fabrication techniques, and individual routines were qualified throughout a measurement for their influence on the compositional purity of the salt materials. A custom crucible for DSC was also developed and prototypes were analyzed. By developing capabilities to perform both

DSC and XRD on fluoride salts, it was suggested that little contamination may be introduced during the developed techniques for processing salt materials. Furthermore, depending on the interpretation of DSC measurements, there is reason to suggest that dehydration procedures on non-actinoid salts are successful in improving the measured thermal behaviour of the salt material. Purification of actinoids however was found to produce negligible change on XRD patterns, and the presence of an unidentified peak was present throughout. This activity should be further investigated, inspired by work from Che *et al.* [81].

A literature review was also conducted to construct a roadmap for future research by the NFMG, providing insight into gaps in current literature on fission product systems and certain experimental practises. The literature review also constructed a database suggesting common practises between reported work and identified auxiliary techniques (such as Tammann diagrams) which may aid in future campaigns studying novel salt systems.

CHAPTER 9

Recommendations for Future Research

Throughout development of the experimental framework described in this work, a number of considerations became apparent which could aid future efforts that employ this work. An obvious requirement is to acquire a fully qualified DSC crucible design. Improvements to the quantitative qualification of the entire experimental routine could then be made, and temperature calibration could be justified. If experimental equipment was more developed towards the use of ICP-MS, quantification of compositional accuracy would greatly benefit and the environment of uncertainty in DSC measurements would be improved in an area yet unreported or unstandardized in open literature. There are also other techniques, such as Extended X-ray Absorption Fine Structure (EXAFS) or Nuclear Magnetic Resonance (NMR) which would provide direct and quantitative insights into the interactions of salt with processing and measurement materials as well.

Additionally, the purification of actinoid fluorides should be revisited according to the work by Che *et al.* [81], where an experimental process of room temperature re-

action for a number of days is investigated relative to the conclusions found form this work. Results from the purification of ThF_4 which was not based precisely on the process reported by Che at al. proved inconclusive and this should be addressed through both an improvement to the purification procedures but also with DSC measurements on ThF_4 to couple to the XRD observations. There is also room to comprehensively perform an assessment of the DMM against a bulk mixing approach, where statistical replicability should be a major focus. Inspired by the early work of ORNL, crucible sealing and crucible filling (mixing) procedures could also be completely re-considered with a crimping or welding design with the development of a custom crucible filling needle [37].

APPENDIX A

Standard Operating Procedures

The following is a collection of SOPs have been written. Experience gained through using these documents in the fabrication of salt materials and throughout experiment qualification has led to revisions and improvements resulting in their current form. Complimenting each SOP, D. Hallatt has also constructed standardized worksheets which are to accompany the operator of the respective SOP for an organized and accountable original version of experimentally recorded values. Such experimental worksheets are stored together in the NFMG laboratory in ERC 2096, and only photocopies of the original documents leave the room. The official source for SOPs and worksheets, including their revision logs, affiliated safety sheets, and approval logs, are available for dissemination in the ERC 2096 SOP binder. Electronic copies of all documentation are also made available online at `https://nuclear.ontariotechu.ca/piro/`.

A.1 Particle Size Measurement

In accordance with ASTM B214-16 ($2.50\,\text{g} \pm 0.01\,\text{g}$ quantity)

1. Ensure that the operator is in good physical condition with no expected back, wrist, or arm fatigue/pain.

2. Clean and dry sieves, brushes, and scoopulas (2) according to SOP A.6.

3. Unless already in the glovebox, a blank High Density PolyEthylene (HDPE) container, a stack of paper sticky notes, the appropriate worksheet, and the cleaned items from step #2 into the glovebox.

4. Ensure material to be measured is in a closed (*bulk*) container (ideally HDPE) within the glovebox.

5. Tape this SOP onto the outside of the glovebox for reference.

6. Put on disposable latex gloves, enter hands into glovebox gloves, and put on latex gloves over top of the installed glovebox gloves within the glovebox.

7. Ensure that the scale within the glovebox is properly calibrated and levelled.

8. Ensure that sieves are in good working condition (mesh is not compromised) and are also stacked from the largest to finest mesh size (starting with the lid and ending with the blind).

9. Zero the scale and weigh the filled, bulk, container of material. Record this value on the worksheet as item *a*. Place container on floor of glovebox once done.

10. Label a new and empty HDPE container with permanent marker to designate it for material that is going to be measured for its particle size (*ChemicalFormula.-PS.IterationNumber*). Note: for statistical significance this procedure should

be repeated on new sample material, and hence designated with an iteration number each time.

11. Tare the scale to a new small white tray sitting inside of a new large white tray. The large white tray is to catch spillage onto the scale's surface.

12. Rotate the weighed container of material in the pitch, yaw, and roll directions to mix particle sizes. This is to improve sampling representation.

13. Carefully open the bulk container of material, trying not to jolt the material into an inhomogeneous particle size distribution (spatially).

14. Hole the bulk open container of material with one hand through one side of the scale's side window, and a scoopula in the other hand through the scale's other side window. Both hands should be over top of the small-large white tray stack on top of the scale's surface.

15. Use a cleaned scoopula to weigh out a quantity of $2.50\,\mathrm{g} \pm 0.01\,\mathrm{g}$ into the small white tray that was tared and sitting on the scale. Once close to $2.5\,\mathrm{g}$, remove hands from the scale, close windows, and record this value as item c on the worksheet once the mass settles.

16. Close the bulk container of material.

17. Remove lid off of sieve stack, careful not to contaminate the inner mesh with any noticeable amounts of material, and ensure ordering of the sieves is correct in the stack.

18. Remove small white tray of material from the scale and gently pout weighed material into top sieve in a localized hill of material without spilling.

19. If residue or material is left behind in the small white tray, fold the tray into a triangle and use as a make-shift funnel to pour remaining material out of a corner.

20. Place now emptied, small, white tray and large white tray into appropriate waste container within the glovebox.

21. Place lid of sieve stack back onto stack.

22. Zero the scale, weigh the bulk container of material, record the value on the worksheet as item b, and return the container to storage within the glovebox.

23. Ensure that the sieve stack remain in place together until otherwise instructed.

24. Move pad of sticky pads in front of operator on the glovebox floor against the inner glass/wall.

25. Place the sieve stack on top of sticky notes to cushion the following sieve shaking process against the floor of the glovebox.

26. Set and start the glovebox timer for 15 minutes.

27. With two hands, hole the stack of sieves between your thumbs (on the lid) and remaining fingers (on the bottom of the blind).

28. Quickly rotate the stack in the clockwise and anti-clockwise direction in the plane of the floor, switching directions every minute. In addition, hit the bottom of the sieve stack against the pad of sticky notes every 360°.

29. Shut off the alarming timer and stop sieve motion.

30. Obtain a new large white tray and ensure that the scale is properly calibrated.

31. Tare the scale to the new, large, white tray.

32. Remove the tared large white tray from the scale and place it on the glovebox floor to the dominant hand side of the sieve stack.

33. Gently remove the lid from the sieve stack and turn it upside down so no residue falls out.

34. Rotate the sieve stack lid over top of the tares large white tray and pour/tap any residue into the tray.

35. Place the lid far away from the action within the glovebox.

36. Hold the stack of sieves and gently tap the top of the outer structural ring of the topmost sieve with the handle of a brush.

37. Gently remove the topmost sieve and hold the sieve over top of the sieve stack.

38. Hold the brush in your other hand and gently brush the inner walls and surface of the bottom of the sieve's mesh to allow any residue to fall onto the top mesh of the sieve below it (the *new* topmost sieve of the stack).

39. Move the sieve over top of the tare large white tray and gently rotate the sieve up on one side to allow material to fall into the edge of the mesh and inner wall of the sieve, ready for pouring out.

40. Carefully pour out the material inside the sieve into a localized hill in the tared large white tray.

41. Rotate the sieve just past 90° (just past perpendicular to the tared large white tray), and gently brush the inside wall and mesh of the sieve to remove any material residue into the tared large white tray.

42. Place the sieve on an edge of the sieve's top outer structural ring on a clean section inside of the tared large white tray's floor so that the top of the sieve's mesh is facing the tared large white tray.

43. Gently knock the bottom of the structural ring of the sieve around 360° to remove and residual material into the tared large white tray.

44. Life the sieve out and inspect the top of the sieve for any residual material. Brush off any residuals int he large white tray.

45. Place the empty sieve neear the lid.

46. Weigh the tared large white tray and appropriately record its value in the worksheet (appropriate with respect to the associated sieve size, items d - h).

47. Tare the scale the the filled large white tray.

48. Repeat steps 38 - 47 working down in the sieve stack until the blind is remaining.

49. Follow steps 39 - 46 for the blind container of the sieve stack.

50. Remove the large white tray from the scale and place it away from the operator on the floor of the glovebox.

51. Zero the scale, ensuring no spilled material is on the scale's surface, and record the mass of the empty HDPE container (which was designated and labelled previously for the particle size measurement) in the worksheet as item i.

52. Remove the container from the scale, open it, and place it in a new, large, white tray on the flow of the glovebox to catch spillage.

53. Pour contents of the weighed large white tray into the HDPE container.

54. If required due to remainng residue, fold the large white tray into a triangle and crinkle and tap the folded *funnel*, large, white tray into the labeled HDPE container.

55. Close the labeled HDPE container and put the folded, large, white tray into the appropriate waste container within the glovebox.

56. Place the filled HDPE container on the scale and record the value in the worksheet as item j.

57. Stack the dirty sieves back together and egress them from the glovebox for cleaning according to SOP A.6.

58. When calculating the recovery fraction, use 98.5% as a minimum cut-off instead of the ASTM standard 99%.

A.2 Particle Size Reduction

1. Ensure that the particle size of the as-received material have been characterized according to SOP A.1.

2. Clean and dry a mortar, pestle, brush, and at least two scoopulas according to SOP A.6, and ingress them into the glovebox along with an appropriate worksheet.

3. Ensure that the operator is in good physical condition with no expected back, wrist, or arm fatigue/pain.

4. Ensure that a blank HDPE container and a timer are in the glovebox and in working order.

5. Ensure that the material to be processed is in a closed container (ideally HDPE) within the glovebox.

6. Tape this SOP onto the outside of the glovebox for reference.

7. Put on disposable latex gloves, enter hands into glovebox gloves, and put on latex gloves over top of the installed glovebox gloves within the glovebox.

8. Label the blank HDPE container with a permanent marker to designate it for material that is to undergo particle size reduction (*ChemicalFormula.PSR.IterationNumber*). Note: for statistical significance, this procedure should be repeated on new sample material, and hence designated with an iteration number.

9. Place visibly clean, large, white tray underneath the mortar in a comfortable place o the floor of the glovebox. This is to catch and spillage while grinding.

10. Ensure that the scale within the glovebox is properly calibrated and levelled.

11. Zero the scale, weigh the bulk HDPE container of larger particle size material, and record the value on the worksheet as item *a*.

12. Carefully open the weighed HDPE container of material and use a clean and dried scoopula to add material into mortar until a maximum of 1/3 of the mortar is filled (by volume).

13. Close the container of larger particle size material and weigh this container again with the scale, recording its value in the worksheet as item *b*.

14. Set and start the glovebox timer for 5 minutes.

15. With the operator's less-dominant hand, hold down the mortar inside the large white tray.

16. With the operator's dominant hand, grind the material in the mortar by pressing down with medium-hard pressure in circular motions being careful not to spill material out of the mortar. As needed, also press pestle from edge to bottom of mortar, working the material into a powder until all material is pushed away from linear line of pressing (rotate mortar and continue pressing down from edge where material has moved to).

17. Shut the alarming timer off and stop grinding.

18. Weigh the labelled HDPE container and record the value on the worksheet as item *c*.

19. Open the labeled HDPE container from and put container in new, clean, large white tray for possible spillage.

20. Remove the mortar from the large white tray and use a clean and dry scoopula to carefully collect material into one side of mortar while holding assembly above the large white tray for possible spillage.

21. Pour the mortar contents into the empty, labeled HDPE container and scrape any remaining material with the scoopula.

22. If any residue remains in the mortar use the clean and dry brush to transfer into the HDPE container.

23. Close the labeled HDPE container, weigh the container + contents, and record the value on the worksheet as item *d*.

A.3 Dehydration

1. Clean and dry the small nickel reaction vessel, brushes, and scoopulas (2) according to SOP A.6.

2. Unless already in the glovebox, ingress an appropriate worksheet, a blank HDPE container, and the cleaned items into the glovebox.

3. Ensure the material to be processed is in a closed (bulk) container (ideally HDPE container) within the glovebox, along with the glovebox thermocouple and timer.

4. Put on disposable latex gloves, enter hands into glovebox gloves, and put on latex gloves over top of the installed glovebox gloves within the glovebox.

5. Label the blank HDPE container with a permanent marker to designate it for material that is to undergo dehydration (*ChemicalFormula.Dehy.IterationNumber*). Record this label on the worksheet in the notes for item *a*.

6. Ensure that the scale within the glovebox is properly calibrated and levelled.

7. Zero the scale, weigh the bulk HDPE container of material to be measured, and record the value on the worksheet as item *a*.

8. Put a 500 ml glass beaker filled with 100 ml of sand on top of the hotplate within the glovebox and the retort stand beside the hot plate with the thermocouple and probe held outside of the beaker by the retort stand.

9. Tare the scale to the small nickel crucible sitting inside of a new large white tray. The large white tray is to catch spillage onto the scale surface (reduce false positive material addition).

10. Hold the bulk open container of material with one hand through one side of the scale's side window, and a scoopula in the other hand through the scale's other

side window. Both hands should be over top of crucible-large white tray stack on top of scale surface.

11. Use a cleaned scoopula to weigh out a quantity of material into the nickel crucible that was tared against. Once close to the intended mass: remove hands from scale, close windows, and record this value on the worksheet as item c once the mass is settled.

12. Remove the filled crucible from the scale and close the bulk container of material.

13. Zero the scale, weigh the bulk container of material on the scale, record the value on the worksheet as item b, and return the container to the storage location within glovebox.

14. With the tips of the tongs, carefully place the filled nickel crucible into the sand bath on the hotplate, pressing down to immerse the crucible to at least 12.7 mm depth in the sand.

15. Place the nickel lid on the crucible, but with approximately 6.35 mm of the lid sitting off the edge of the crucible to allow produced gases/evaporated moisture to escape.

16. Adjust the retort stand such that the thermocouple probe is immersed into the sand of the beaker. The thermocouple probe should be immersed to the same depth as the base of the nickel crucible.

17. Ensure that no flammable items are touching the surface of the hotplate or in a position susceptible to falling into the hotplate over then next 6 hours.

18. Unless otherwise specified, set the hotplate to a temperature of 400 °C on the hotplate's display. This should result in a temperature of roughly 350 °C at the crucible, as per the hotplate characterization.

19. Set and start the glovebox timer for 5 hours, and take latex gloves off of installed glovebox gloves. NOTE: the current glovebox timer does not go this long, so skip this step.

20. Remove right hand from glovebox and hold the left glovebox glove outside of the glovebox while removing left hand.

21. Tie the left glove into a knot to avoid the glove touching the hotplate. Lock this left glove port afterwards.

22. Let right glove remain inflated in glovebox and lock right glove port.

23. Set and start personal phone (or other) timer for 4.75 hours.

24. Write *Glovebox is hot. Contact operator at phone number in case of emergency* on a piece of paper in permanent ink and tape to outside window of glovebox.

25. Once alarming, shut the personal alarming timer off, and wait until the glovebox timer starts alarming.

26. Unlock glove ports of the glovebox and turn off hotplate within glovebox after un-tying left glove.

27. Repeat steps 21 - 22 and set glovebox timer for 30 minutes.

28. Once glovebox timer is alarming, check temperature of glovebox thermocouple, if reading less than or equal to 40 °C: take sign off glovebox window, remove the thermocouple and probe from the vicinity of the beaker and remove the sand filled beaker from the hotplate. If not, continue waiting until true.

29. Remove the lid of the nickel crucible and carefully remove the crucible from the sand beaker to the floor of the glovebox with the tongs.

30. Place the sand beaker back on top of the hot plate.

31. Place the labeled HDPE container inside a clean large white tray on the floor of the glovebox. The white tray is to help with any spillage.

32. Ensure that the scale within the glovebox is properly calibrated and levelled.

33. Zero the scale, weigh the labelled, empty HDPE container, and record the value on the worksheet as item *d*.

34. Place the empty, labeled HDPE container in the large white tray and pour the (hopefully dehydrated) contents of the nickel crucible into the HDPE container as best the operator can, empty any spilled contents of the white tray into the HDPE container, and close the lid of the container.

35. Wipe the surface of the HDPE container with a *kimtech* wipe to ensure no spilled material is on the bottom particularly.

36. Measure the mass of the filled HDPE container, and record the value on the worksheet as item *e*.

A.4 X-ray Diffraction

It should be made clear that the nuclear materials laboratory of ERC 4056 does not actively hold a radiation permit for the use of ThF_4. However, a temporary radiation permit can be issued by the radiation safety officer of UOIT for planned work. Minor revisions to the technical procedures outlined in the respective SOPs accompany the handling of radioactive substances, by which the operator is referred to the NFMG's radiation safety protocols and the UOIT radiation safety manual. Following the completion and expiry of a temporary radiation permit, the associated operators along with Prof. Markus Piro present the radiation safety officer with a performance and summary memo outlining the practises that were followed and the recordings of final radiation scans of the laboratory.

1. Ensure that the XRD dome-style holder, XRD dome-style holder fitting tool, brushes, a glass microscope slide, a set of plastic tweezers, an appropriate work-sheet, and scoopulas (min. 2) are all inside of the glovebox.

2. Ensure that a sensitivity study has been performed on the XRD dome-style holder's seal, consecutively scanning a quantity of material in sequential measurements back-to-back. Resultant diffraction patterns should overlap with no significant impurity detected.

3. Physically verify that no one is using the XRD instrument in ERC 4056 before beginning this SOP.

4. Go to the XRD computer in ERC 4056 and complete the measurement profile with specific measurement parameters and file name according to the SOP manual [158].

5. While in ERC 4056, begin XRD x-ray tube warm up sequence via the computer. This will take approximately 20 minutes, and can run while the following steps

are completed in ERC 2096 [158].

6. Ensure that a background XRD measurement has been performed according to the exact same conditions (holder type, scanning rate, scanning length, *etc.*).

7. Clean and dry an XRD dome-style holder, brushes, a glass microscope slide, and scoopulas according to SOP A.6.

8. Make sure to keep the bottom of the XRD holder, the top (dome) of the XRD holder, and the XRD holder fitting tool away from one another until intended as they are all magnetic. Unfortunately, pieces can snap together (succumbing to the magnetic field) and spill powder.

9. Put on disposable latex gloves, enter hands into glovebox gloves, and put on latex gloves over top of the installed glovebox gloves within the glovebox.

10. Label the blank HDPE container with a permanent marker to designate it for material that is to undergo XRD measurement (*ChemicalFormula.X.IterationNumber*). Record this label on the worksheet in the notes for item *c*.

11. Place the bottom of the XRD dome-style holder on an upside down large white plastic tray.

12. Ensure that the scale within the glovebox is properly calibrated and levelled.

13. Zero the scale, weigh the bulk HDPE container of material to be measured, and record the value on the worksheet as item *a*.

14. Open container of material and use a scoopula to carefully remove some material onto the inner indent (diameter of 10 mm) of the circular inset in the face of the XRD dome-style holder base. This material should be put on as a small heap with less material than required to fill the holder's indent. Too little is better than too much in this step.

15. Use the cleaned glass microscope slide to pull material across the face of the XRD holder's indent. Add more material as required: stop once entire face of indent is covered flat and evenly with powdered material.

16. Use the glass microscope slide to flatten and compress the material in the XRD holder base by pressing the slide flat down onto the material. The powder should visibly compress evenly against the slide (the slide is transparent).

17. Remove the microscope slide and evaluate for quality of powder surface. The powder should be fairly flat and flush to the same height as the holder. Too much powder perpendicular to the face of the holder reduces the effectiveness of measuring low angle diffraction.

18. Once surface of powder is acceptable, carefully place the lid of the XRD holder (dome) inside of the XRD dome-style holder fitting device with the magnets holding it in place. Use plastic tweezers, if required, to avoid magnetic interference.

19. Gently lower the XRD dome lid over top of the holder's base (which is filled with material) until they are sitting together. Care must be taken, as the magnetic attraction between the two components causes them to snap together. Thus, they should be attached with a focus on fitting them exactly on top of one another to avoid material placed in the base from shifting out of the indent. Keep the fitting device attached. Removing the fitting device is jolting (due to the magnets), and is easier to perform outside of the glovebox with bare hands without disrupting the carefully levelled powder.

20. Place bulk HDPE container of material on the scale and record its value in worksheet as item b.

21. Remove outer latex gloves from installed glovebox gloves and remove hands from glovebox.

22. Egress the sealed XRD holder from the glovebox, while being careful when putting the filled holder into the antechamber and when taking it out do not jar the material from its designated position in the holder. The egress procedure may be adjusted to include 6 partial vacuums of the ante-chamber rather than 3 *full* vacuums. Such practise may help reduce the possibility of the XRD holder's seal being broken during the egress procedure vacuum.

23. Once the XRD holder is outside of the glovebox, carefully tilt the filled holder fitting device from the sealed holder assembly (body and dome lid) and remove without breaking the seal of the holder itself. This step may be made easier by using plastic (non-magnetic) tweezers or the operators fingers to hold the edge of the salad holder while pulling the fitting device away. If seal breaks, repeat this SOP with fresh salt.

24. Place the filled dome-style holder in the transport box and transport to ERC 4056 via the stairs. This process should take 30-60 seconds and is less variable than waiting for the elevator.

25. Enter ERC 4056 and begin XRD measurement on the dome-style holder and contents, once operator has donned new latex gloves.

26. Once the measurement is complete, return the holder to ERC 2096 in a timely fashion and ingress the filled holder into the glovebox.

27. Put on disposable latex gloves, enter hands into glovebox gloves, and put on latex gloves over top of the installed glovebox gloves within the glovebox.

28. Weigh the empty, labelled HDPE container labeled and record its value in the worksheet as item *c*.

29. Remove the HDPE container from the scale, place it in a large white tray on the floor of the glovebox, and open the container.

30. Carefully open the XRD dome-style holder and remove contents into this empty HDPE container from by tapping the side of the XRD holder against the mouth of the container and using a scoopula to remove any residual particles.

31. Close the HDPE container full of measured material and place the container on the scale for measurement.

32. Record the mass of the HDPE container on the worksheet as item *d*.

A.5 Fluorination Purification

1. Clean and dry the stacked nickel reaction vessel (a large commercial nickel vessel, and a second with an exhaust pipe built in), brushes, and scoopulas (2) according to SOP A.6.

2. Unless already in the glovebox, ingress an appropriate worksheet, a blank HDPE container, and the cleaned items into the glovebox.

3. Ensure the material to be processed is in a closed (bulk) container (ideally HDPE container) within the glovebox, along with the glovebox thermocouple and timer.

4. Put on disposable latex gloves, enter hands into glovebox gloves, and put on latex gloves over top of the installed glovebox gloves within the glovebox.

5. Label the blank HDPE container with a permanent marker to designate it for material that is to undergo dehydration (*ChemicalFormula.Dehy.IterationNumber*). Record this label on the worksheet in the notes for item *a*.

6. Ensure that the scale within the glovebox is properly calibrated and levelled.

7. Zero the scale, weigh the bulk HDPE container of material to be measured, and record the value on the worksheet as item *a*.

8. Put a 500 ml glass beaker filled with 100 ml of sand on top of the hotplate within the glovebox and the retort stand beside the hot plate with the thermocouple and probe held outside of the beaker by the retort stand.

9. Tare the scale to the large commercial nickel crucible sitting inside of a new large white tray. The large white tray is to catch spillage onto the scale surface (reduce false positive material addition).

10. Hold the bulk open container of material with one hand through one side of the scale's side window, and a scoopula in the other hand through the scale's other

side window. Both hands should be over top of crucible-large white tray stack on top of scale surface.

11. Use a cleaned scoopula to weigh out a quantity of material into the nickel crucible that was tared against. Once close to the intended mass: remove hands from scale, close windows, and record this value on the worksheet as item *c* once the mass is settled.

12. Close the bulk container of material and temporarily put the container in the second white tray (on the floor of the glovebox).

13. Tare the scale with the large white tray and the filled, large, nickel crucible.

14. Open the container of NH_4HF_2 beads and, with a clean scoopula, measure out a quantity equivalent to approximately a 5.5:1 molar ratio of NH_4HF_2:ThO_2. Do so by holding the container of NH_4HF_2 with one hand through one side of the scale's side window, and a scoopula in the other hand through the scale's other side window. Both hands should be over top of crucible-large white tray stack on top of scale surface. Record this value in the worksheet as item *f*.

15. Remove the large white tray and large, nickel crucible from the scale.

16. Use the scoopula from to stir the binary mixture of materials in the large crucible for approximately 20 seconds, while it sits inside the large white tray.

17. With the tips of the tongs, carefully place the filled nickel crucible into sand bath on the hotplate, pressing down to immerse the crucible to at least 12.7 mm depth in the sand.

18. Put a nickel lid on the large nickel crucible while it sits in the sand to avoid contamination of the binary mixture of actinoid fluoride material and NH_4HF_2.

19. Zero the scale, tare the scale to a clean large white tray, weigh the bulk container of material on the scale, record the value in the worksheet as item *b*, and return

the bulk container to the appropriate storage location within the glovebox.

20. Tare the scale to the upper nickel reaction vessel (the one with the exhaust pipe) as it sits in a new, clean large white tray.

21. Open the container of NaOH and place the lid away from activity in the glovebox.

22. Hold the bulk open container of NaOH with one hand through one side of the scale's side window, and a clean scoopula in the other hand through the scale's other side window. Both hands should be over top of crucible-large white tray stack on top of scale surface.

23. Carefully use a cleaned scoopula to weigh out 5 g of NaOH from the bulk container into the nickel reaction vessel (around the inner pipe). Once close to 5 g: remove hands from scale, close windows, and record this value in the worksheet as item g once mass is settled.

24. Close the bulk container of NaOH and return it to the storage location in glovebox.

25. Remove the lid from the large nickel reaction vessel sitting in the sand bath and slide the exhausted nickel vessel into the large nickel reaction vessel (it sits partially inside like stacking cups).

26. Place the nickel lid on top of the stacked large nickel reaction vessel, and place the designated weight on top of this assembly using the tongs.

27. Put the arm of the glovebox thermocouple probe in the retort stand and adjust it so that the thermocouple probe is immersed into the sand bath. The thermocouple probe should be immersed to the same depth as the base of the nickel crucible.

28. Ensure that no flammable items are touching the surface of the hotplate or in a position susceptible to falling into the hotplate over then next 16 hours.

29. Unless otherwise specified, set the hotplate to a temperature of 350 °C on the hotplate's display. This should result in a temperature of roughly 250 °C at the crucible, as per the hotplate characterization.

30. Throughout the operation of the hotplate, ensure that the temperature read by the glovebox thermocouple does not exceed 400 °C. If so, turn down the control knob of the hotplate and evaluate.

31. Set and start the glovebox timer for 12 hours, and take latex gloves off of installed glovebox gloves.

32. Remove right hand from glovebox and hold the left glovebox glove outside of the glovebox while removing left hand.

33. Tie the left glove into a knot to avoid the glove touching the hotplate. Lock this left glove port afterwards.

34. Let right glove remain inflated in glovebox and lock right glove port.

35. Set and start personal phone (or other) timer for 11.75 hours. item Write *Glovebox is hot and contains hot radioactive materials. Contact operator at phone number in case of emergency* on a piece of paper in permanent ink and tape to outside window of glovebox.

36. DO NOT LEAVE THE LAB UNATTENDED (RAD. MATLS IN USE).

37. Once alarming, shut the personal alarming timer off, and wait until the glovebox timer starts alarming.

38. Unlock glove ports of the glovebox and turn off hotplate within glovebox after un-tying left glove.

39. Repeat steps 33 - 34 and set glovebox timer for 30 minutes.

40. Once glovebox timer is alarming, check temperature of glovebox thermocouple, if reading less than or equal to 40 °C: take sign off glovebox window, remove the thermocouple and probe from the vicinity of the beaker and remove the sand filled beaker from the hotplate. If not, continue waiting until true.

41. Remove the lid on top of the stacked crucibles and carefully remove the nickel reaction vessel from the sand beaker into the large white tray. Move this pair away from action in the glovebox temporarily.

42. Place another large white tray on the floor of the glovebox, and place the labeled and empty HDPE container inside. The white tray is to help with any spillage.

43. Zero the scale, weigh the empty HDPE container, and record the value in the worksheet as item *d*.

44. Place the empty, labeled HDPE container in the large white tray and pour the (hopefully purified) contents of the nickel reaction vessel into the HDPE container as best the operator can, empty any spilled contents of the white tray into the HDPE container, and close the lid of the container.

45. Wipe the surface of the HDPE container with a *Kimtech* wipe to ensure no spilled material is on the bottom particularly.

46. Tare the scale to a new large white tray and measure the weight of the filled HDPE container in the white tray, and record the value in the worksheet at item *e*

A.6 Cleaning Tools

1. Identify which tools are to be washed.
2. Turn on drying furnace (standard box furnace in Energy systems and nuclear science Research Centre [ERC] 4056) & set furnace control to 70 °C to achieve 65 °C in the furnace. Note: If washing/drying sieve or dome-style XRD holder, set furnace to 40 °C to be careful of the rubber o-rings and seals.
3. Insert furnace thermocouple probe with thermocouple reader attached.
4. If required, remove identified utensils and & tools from glovebox.
5. Put on disposable latex gloves.
6. Set items beside the sink in ERC 2096. If items have large scale chemical contamination, clean with *kimtech* wipe and dispose of chemicals in chem-waste accordingly.
7. Fill large beaker with soap and water and place them in the sink.
8. One at a time, submerge items in the soap/water beaker and scrub the surfaces gently with a brush in the drying rack labeled *for washing*. May also use a cotton ball or *kimtech* wipe for scrubbing. Note: if washing sieves, there is a specific procedure for this step:
   (a) Submerge sieve in soap/water beaker top up 5 times with force.
   (b) Flip sieve over (now bottom up) and gently brush and poke bottom of sieve. Do so in-between submerging sieve to maintain wet mesh.
   (c) Flip sieve over (now top op) and brush surface of mesh and inner sides of sieve frame.
   (d) Brush external side of sieve frame.
9. One at a time, rinse items with de-ionized water, then with ethanol, and place on drying rack. Note: if washing XRD dome-style holder, do not rinse with ethanol.
10. Subject rinsed items to hair dryer on *warm* setting for 30 seconds, rotating.
11. Wipe surfaces of items as best as possible with a dry *kimtech* wipe. Important to remove any drops of liquid.
12. Place dried item on dry paper towel.
13. Once all items have been washed and placed on dry paper towel, place all items in clean transport plastic baggie.

14. Dispose of current disposable latex gloves, and carry items up to the furnace in ERC 4056.

15. Put on new disposable latex gloves once inside ERC 4056.

16. Place items in hot furnace once external thermocouple reads greater than 5 °C less than the desired temperature, and set a timer for 60 minutes. Note: if drying sieves or a XRD dome-style holder, only set the timer for 30 minutes. Re-evaluate success of drying after that time.

17. Once timer is alarming: turn off furnace, remove items from furnace while wearing new disposable latex gloves, and put items into a new plastic baggie for transport back to ERC 2096.

References

[1] M. Roser, "Human development index (hdi)," *Our World in Data*, 2019.

[2] "Global energy and CO_2 status report 2018," tech. rep., International Energy Agency, Paris, France, 2018.

[3] S. Alexander, "Peak oil, energy descent, and the fate of consumerism," *Social Science Research Network*, pp. 1–18, 2012.

[4] N. Goodwin, J. Nelson, F. Ackerman, and T. Weisskopf, *Consumption and the Consumer Society*, vol. A GDAE Teching Module on Social and Environmental Issues in Economics. Medford, MA, USA: Global Development And Environment Institute, Tufts University, 2008.

[5] *The Future of Nuclear Energy in a Carbon-Constrained World, An Interdisciplanry MIT Study.* MIT Future of, Cambridge, Massachusetts, USA: Massachusetts Institute of Technology, 2018.

[6] "Energy and climate change; world energy outlook special briefing for COP21," tech. rep., International Energy Agency, Paris, France, 2015.

[7] "Energy and climate change; world energy outlook special report," tech. rep., Inernational Energy Agency, Paris, France, 2015.

[8] P. Droege, ed., *Urban Energy Transition From Fossil Fuels to Renewable Power*. World Council for Renewable Energy, Oxford, UK: Elsevier, 2008.

[9] I. Dincer, "Renewable energy and sustainable development: a crucial review," *Renewable and Sustainable Energy Reviews*, vol. 4, no. 2, pp. 157 – 175, 2000.

[10] "New energy strategy plan," tech. rep., Energy Strategy Office, Policy Planning and Coordination Division, Commisioner's Secretariat, Agency for Natural Resourcees and Energy of Japan, 2018.

[11] A. Markandya and P. Wilkinson, "Electricity generation and health," *The Lancet*, vol. 370, no. 9591, pp. 979 – 990, 2007.

[12] M. Vasilis and C. Hyung, "Greenhouse-gas emissions from solar electric- and nuclear power: A life-cycle study," *Energy Policy*, vol. 35, no. 4, pp. 2549 – 2557, 2007.

[13] R. Turconi, A. Boldrin, and T. Astrup, "Life cycle assessment (LCA) of electricity generation technologies: Overview, comparability and limitations," *Renewable and Sustainable Energy Reviews*, vol. 28, pp. 555 – 565, 2013.

[14] Canadian Small Modular Reactor Roadmap Steering Committee, "A call to action: A canadian roadmap for small modular reactors," tech. rep., Ottawa, Ontario, Canada, 2018.

[15] U.S. Department of Energy Research Advisory Committee, "A technology roadmap for generation IV nuclear energy systems," Tech. Rep. GIF-002-00, Generation IV International Forum, 2002.

[16] Generation IV International Forum, "GIF research and development outlook for generation nuclear energy systems: 2018 update," tech. rep., Generation IV International Forum, 2018.

[17] J. Serp, A. Michel, O. Beneš, S. Delpech, O. Feynberg, V. Ghetta, D. Heuer, D. Holcomb, V. Ignatiev, J. L. Kloosterman, L. Luzzi, E. Merle-Lucotte, J. Uhlíř, R. Yoshioka, and D. Zhimin, "The molten salt reactor (MSR) in generation IV: Overview and perspectives," *Progress in Nuclear Energy*, vol. 77, pp. 308–319, 2014.

[18] T. Dolan, *Molten Salt Reactors and Thorium Energy.* Duxford, United Kingdom: Woodhead Publishing is an imprint of Elsevier, 2017.

[19] O. Beneš, "Molten Salt Reactor Fuel and Coolant," in *Comprehensive Nuclear Materials* (R. J. M. Konings, ed.), vol. 3, ch. 3.13, pp. 359–389, Oxford: Elsevier, 2012.

[20] J. McMurray, T. M. Besmann, J. Ard, B. Fitzpatrick, M. H. A. Piro, J. Jerden, M. Williamson, B. Collins, B. Betzler, and A. Qualls, "Multi-physics simulations for molten salt reactor evaluation: Chemsitry, modelling, and database development," Tech. Rep. ONRL/SPR-2018/864, Oak Ridge National Laboratory, Oak Ridge, Tennessee, USA, 2018.

[21] O. Beneš and R. Konings, "Thermodynamic evaluation of the MF–LaF_3 (M=Li, Na, K, Rb, Cs) systems," *Calphad*, vol. 32, no. 1, pp. 121–128, 2008.

[22] E. Capelli, O. Beneš, P. E. Raison, M. Beilmann, C. Künzel, and R. J. M. Konings, "Thermodynamic investigation of the CaF_2-ThF_4 and the LiF-CaF_2-ThF_4 systems," *Journal of Chemical & Engineering Data*, vol. 60, no. 11, pp. 3166–3174, 2015.

[23] D. Leblanc, "Molten salt reactors: A new beginning for an old idea," *Nuclear Engineering and Design*, vol. 240, no. 6, pp. 1644–1656, 2010.

[24] E. Corcoran, M. Kaye, and M. Piro, "An overview of thermochemical modelling of CANDU fuel and applications to the nuclear industry," *CALPHAD: Computer Coupling of Phase Diagrams and Thermochemistry*, vol. 55, pp. 52–62, 2016.

[25] M. Piro, J. Banfield, K. Clarno, S. Simunovic, T. Besmann, B. Lewis, and W. Thompson, "Coupled thermochemical, isotopic evolution and heat transfer simulations in highly irradiated UO_2 nuclear fuel," *Journal of Nuclear Materials*, vol. 441, no. 1-3, pp. 240–251, 2013.

[26] R. Thoma, "Phase Diagrams of Nuclear Reactor Materials," Tech. Rep. ORNL-2548, Oak Ridge National Laboratory, Oak Ridge, Tennessee, USA, 1959.

[27] R. Thoma and W. Grimes, "Phase equilibrium diagrams for fused salt systems," Tech. Rep. ORNL-2295, Oak Ridge National Laboratory, Oak Ridge, Tennessee, USA, 1960.

[28] O. Beneš, *Thermodynamics of Molten Salts for Nuclear Applications - JRC-ITU-TN-2008/40*. Doctoral thesis, Institute of Chemical Technology, Faculty of Chemical Technology, Department of Inorganic Chemistry, Prague, Czech Republic, 2008.

[29] E. Capelli, *Thermodynamic Characterization of Salt Components for Molten Salt Reactor Fuel*. Doctoral thesis, TU Delft, Melkeweg, The Netherlands, 2016.

[30] A. E. Gheribi, D. Corradini, L. Dewan, P. Chartrand, C. Simon, P. A. Madden, and M. Salanne, "Prediction of the thermophysical properties of molten salt fast reactor fuel from first-principles," *Molecular Physics*, vol. 112, no. 9-10, pp. 1305–1312, 2014.

[31] A. L. Smith, "A new approach for comprehensive modelling of molten salt properties," in *Thorium Energy Conference*, (Brussels, Belgium), 2018.

[32] E. Capelli and R. Konings, "Thermodynamic assessment of the niobium-fluorine system by coupling density functional theory and CALPHAD approach," *Journal of Fluorine Chemistry*, vol. 208, pp. 55–64, 2018.

[33] O. Beneš, P. Zeller, M. Salanne, and R. J. M. Konings, "Density functional theory, molecular dynamics, and differential scanning calorimetry study of the RbF-CsF phase diagram," *The Journal of Chemical Physics*, vol. 130, no. 13, pp. 134716(1)–134716(4), 2009.

[34] N. Paulson, B. Bocklund, R. Otis, Z. Liu, and M. Stan, "Quantified uncertainty in thermodynamic modeling for materials design," *Acta Materialia*, vol. 174, pp. 9–15, 2019.

[35] C. Guéneua, S. Gossé, A. Quaini, N. Dupin, B. Sundman, D. Manara, R. Konings, M. Kurata, T. Besmann, P. Turchi, J. Dumas, E. Corcoran, M. Piro, T. Ogata, R. Hania, B. Lee, R. Kennedy, and S. Massara, "Fuelbase, taf-id databases oc software: Advanced computational tools to perform themrmodynamic calculations on nuclear fuel materials," in *The 7th European Review Meeting on Sever Accident Research (ERMSAR-2015)*, (Marseille, France), 2015.

[36] J. Blomeke, "Investigation of ThF_4 fused salt solutions for homogeneous breeder reactors," Tech. Rep. ORNL-1030, Oak Ridge National Laboratory, Oak Ridge, Tennessee, USA, 2015.

[37] P. Tucker and E. Joy, "Thermal-gradient quenching furnace for preparation of fused salt samples for phase analysis," *American Ceramic Society Bulletins*, vol. 36, no. 2, pp. 52–54, 1957.

[38] H. Friedman, G. Hebert, and R. Thoma, "Thermal analysis and gradient quenching apparatus and techniques for the investigation of fused salt phase equilibria," Tech. Rep. ORNL-3373, Oak Ridge National Laboratory, Oak Ridge, Tennessee, USA, 1962.

[39] L. V. Jones, D. E. Etter, C. R. Hudgens, A. A. Huffmann, T. B. Rhinehammer, N. E. Rogers, P. A. Tucker, and L. J. Wittenberg, "Phase equilibria in the ternary fused-salt system LiF-BeF_2-UF_4," *Journal of the American Ceramic Society*, vol. 45, no. 2, pp. 79–83, 1962.

[40] J. F. Eichelberger, C. R. Hudgens, L. V. Jones, G. Pish, T. B. Rhinehammer, P. A. Tucker, and L. J. Wittenberg, "Phase equilibria for the ternary fused-salt system NaF-BeF_2-UF_4," *Journal of the American Ceramic Society*, vol. 46, no. 6, pp. 279–283, 1963.

[41] R. E. Thoma, G. M. Hebert, H. Insley, and C. F. Weaver, "Phase equilibria in the system sodium fluoride-yttrium fluoride," *Inorganic Chemistry*, vol. 2, no. 5, pp. 1005–1012, 1963.

[42] R. E. Thoma, H. Insley, H. A. Friedman, and C. F. Weaver, "Phase equilbira in the systems BeF_2-ThF_4 and LiF_2-BeF_2-ThF_4," *The Journal of Physical Chemistry*, vol. 64, no. 7, pp. 865–870, 1960.

[43] D. J. Rogers, T. Yoko, and G. J. Janz, "Fusion properties and heat capacities of the eutectic lithium fluoride-sodium fluoride-potassium fluoride melt," *Journal of Chemical & Engineering Data*, vol. 27, no. 3, pp. 366–367, 1982.

[44] R. E. Thoma, H. Insley, and G. M. Hebert, "The sodium fluoride-lanthanide trifluoride systems," *Inorganic Chemistry*, vol. 5, no. 7, pp. 1222–1229, 1966.

[45] J. P. M. van der Meer, R. J. M. Konings, M. H. G. Jacobs, and H. A. J. Oonk, "A miscibility gap in LiF–BeF_2 and LiF–BeF_2–ThF_4," *Journal of Nuclear Materials*, vol. 344, no. 1, pp. 94–99, 2005.

[46] F. Abdoun, A. Gaune-Escard, and G. Hatem, "Calorimetric and thermal analysis investigations of the MF-LaF_3 mixtures (m = alkali metal)," *Journal of Phase Equilibria*, vol. 18, no. 1, pp. 6–20, 1997.

[47] A. Fortunato, "DSC: History, Instruments and Devices," in *Drug-Biomembrane Interaction Studies* (R. Pignatello, ed.), Woodhead Publishing Series in Biomedicine, ch. 5, pp. 169 – 212, Woodhead Publishing, 2013.

[48] K. C. Hong and O. J. Kleppa, "Thermochemistry of the liquid mixtures of the alkaline earth fluorides with alkali fluorides," *The Journal of Physical Chemistry*, vol. 82, no. 14, pp. 1596–1603, 1978.

[49] G. Hatem, K. Mahmoud, and M. Gaune-Escard, "Thermodynamics of ZrF_4 based molten salt mixtures," in *Halide Glasses V*, vol. 32 of *Materials Science Forum*, pp. 635–642, Trans Tech Publications Ltd, 1 1991.

[50] K. C. Hong and O. J. Kleppa, "Thermochemistry of the liquid mixtures of aluminum fluoride with alkali fluorides and with zinc fluoride," *The Journal of Physical Chemistry*, vol. 82, no. 2, pp. 176–182, 1978.

[51] O. J. Kleppa and K. C. Hong, "Enthalpies of mixing in liquid alkaline earth fluoride-alkali fluoride mixtures. ii. calcium fluoride with lithium, sodium, and potassium fluorides," *The Journal of Physical Chemistry*, vol. 78, no. 15, pp. 1478–1481, 1974.

[52] K. Hong and O. Kleppa, "Thermochemistry of the liquid mixtures of alkali earth fluorides with alkali fluorides," *The Journal of Physical Chemistry*, vol. 82, no. 14, pp. 1596–1603, 1979.

[53] G. Hatem and M. Gaune-Escard, "Calorimetric investigation of xKF+(1-x)NdF_3," *The Journal of Chemical Thermodynamics*, vol. 25, no. 2, pp. 219 – 228, 1993.

[54] A. D. Pelton, S. A. Degterov, G. Eriksson, C. Robelin, and Y. Dessureault, "The modified quasichemical model I—Binary solutions," *Metallurgical and Materials Transactions B*, vol. 31, no. 4, pp. 651–659, 2000.

[55] A. D. Pelton and P. Chartrand, "The modified quasi-chemical model: Part II. Multicomponent solutions," *Metallurgical and Materials Transactions A*, vol. 32, no. 6, pp. 1355–1360, 2001.

[56] A. D. Pelton, P. Chartrand, and G. Eriksson, "The modified quasi-chemical model: Part IV. Two-sublattice quadruplet approximation," *Metallurgical and Materials Transactions A*, vol. 32, no. 6, pp. 1409–1416, 2001.

[57] A. D. Pelton and P. Chartrand, "Thermodynamic evaluation and optimization of the LiCl-NaCl-KCl-RbCl-CsCl-$MgCl_2$-$CaCl_2$ system using the modified quasi-chemical model," *Metallurgical and Materials Transactions A*, vol. 32, no. 6, pp. 1361–1383, 2001.

[58] P. Chartrand and A. D. Pelton, "Thermodynamic evaluation and optimization of the Li, Na, K, Mg, Ca//F, Cl reciprocal system using the modified quasi-chemical model," *Metallurgical and Materials Transactions A*, vol. 32, no. 6, pp. 1417–1430, 2001.

[59] P. Chartrand and A. D. Pelton, "Thermodynamic evaluation and optimization of the LiF-NaF-KF-MgF_2-CaF_2 system using the modified quasi-chemical model," *Metallurgical and Materials Transactions A*, vol. 32, no. 6, pp. 1385–1396, 2001.

[60] J. van der Meer, R. Konings, M. Jacobs, and H. Oonk, "Thermodynamic modelling of LiF-LnF_3 and LiF-AnF_3 phase diagrams," *Journal of Nuclear Materials*, vol. 335, pp. 345–352, 12 2004.

[61] J. van der Meer, R. Konings, and H. Oonk, "Thermodynamic assessment of the LiF–BeF_2–ThF_4–UF_4 system," *Journal of Nuclear Materials*, vol. 357, no. 1-3, pp. 48–57, 2006.

[62] J. P. M. van der Meer, R. J. M. Konings, K. Hack, and H. A. J. Oonk, "Modeling and calculation of the LiF-NaF-MF_3 (M = La, Ce, Pu) phase diagrams," *Chemistry of Materials*, vol. 18, no. 2, pp. 510–517, 2006.

[63] M. Berkani and M. Gaune-Escard, "Study of binary systems NdF_3-MF (M = Li, Na, K): experimental, modeling and thermodynamic computation," *MATEC Web of Conferences;XXXIX JEEP - 39th Edition of the Joint European Days on Equilibrium Between Phases*, vol. 3, no. 01033, pp. 1–3, 2013.

[64] E. Capelli, O. Beneš, and R. Konings, "Thermodynamics of soluble fission products cesium and iodine in the Molten Salt Reactor," *Journal of Nuclear Materials*, vol. 501, pp. 238–252, 2018.

[65] A. Abbasalizadeh, S. Sridar, Z. Chen, M. Sluiter, Y. Yang, J. Sietsma, S. Seetharaman, and K. Hari Kumar, "Experimental investigation and thermodynamic modelling of $LiF-NdF_3-DyF_3$ system," *Journal of Alloys and Compounds*, vol. 753, pp. 388–394, 2018.

[66] O. Beneš, R. Konings, S. Wurzer, M. Sierig, and A. Dockendorf, "A DSC study of the $NaNO_3$-KNO_3 system using an innovative encapsulation technique," *Thermochimica Acta*, vol. 509, no. 1, pp. 62 – 66, 2010.

[67] V. Khokhlov, I. Korzun, V. Dokutovich, and E. Filatov, "Heat capacity and thermal conductivity of molten ternary lithium, sodium, potassium, and zirconium fluorides mixtures," *Journal of Nuclear Materials*, vol. 410, no. 1, pp. 32–38, 2011.

[68] N. Vozárová, A. Smith, J. Colle, P. Raison, D. Bouëxière, R. Konings, and O. Beneš, "Thermodynamic determination and assessment of the CsF-ThF_4," *The Journal of Chemical Thermodynamics*, vol. 114, pp. 71 – 82, 2017.

[69] C. Barton, H. Friedman, W. Grimes, H. Insley, R. Moore, and R. Thoma, "Phase equilibria in the alkali fluoride-uranium tetrafluoride fused salt systems: I, the systems $LiF-UF_4$ and $NaF-UF_4$," *Journal of the American Ceramic Society*, vol. 41, no. 2, pp. 63–69, 1958.

[70] I. dos Santos, D. Klimm, S. Baldochi, and I. Ranieri, "Thermodynamic modeling of the $LiF-YF_3$ phase diagram," *Journal of Crystal Growth*, vol. 360, pp. 172 – 175, 2012.

[71] S. Mukherjee and S. Dash, "Thermodynamic investigation of $NaF-ThF_4$ system and fuel salts of molten salt reactor," *Journal of Fluorine Chemistry*, vol. 212, pp. 17 – 25, 2018.

[72] Q. Dong, R. Chirico, X. Yan, H. Xiangrong, and M. Frenkel, "Uncertainty reporting for experimental thermodynamic properties," *Journal of Chemical Data*, vol. 50, pp. 546–550, 2005.

[73] Working Group 1, "Evaluation of measurement data - guide to the expression of uncertainty in measurement," Tech. Rep. JCGM 100:2008, Joint Committee for Guides in Metrology, Paris, France, 2008.

[74] G. Blyum, "Statistical treatment of experimental data obtained in an investigation of phase equilibira for liquid-vapor and liu," *Theoretical and Experimental Chemistry*, vol. 1, no. 6, pp. 807–14, 1965.

[75] S. Mabrey and J. Sturtevant, "Investigation of phase transitions of lipids and lipid mixtures by high sensitivity differential scanning calorimetry," *Proceedings of National Academic Society*, vol. 73, no. 11, pp. 3862–3866, 1976.

[76] D. Manara, C. Ronchi, M. Sheindlin, M. Lewis, and M. Brykin, "Melting of stoichiometric and hyperstoichiometric uranium dioxide," *Journal of Nuclear Materials*, vol. 342, no. 1, pp. 148 – 163, 2005.

[77] O. Beneš, "Private communication." 2019.

[78] B. Wani, S. Pate, U. Rao, and K. Venkateswalu, "Fluorination of Oxides of Uranium and Thorium by Ammonium Hydrogenfluoride," *Journal of Fluorine Chemistry*, vol. 44, pp. 177–185, 1989.

[79] O. Beneš and R. Konings, "Thermodynamic assessment of the LiF–CeF_3–ThF_4 system: Prediction of PuF_3 concentration in a molten salt reactor fuel," *Journal of Nuclear Materials*, vol. 435, no. 1-3, pp. 164–171, 2013.

[80] E. Capelli, O. Beneš, and R. Konings, "Thermodynamic assessment of the LiF–ThF_4–PuF_3–UF_4 system," *Journal of Nuclear Materials*, vol. 462, pp. 43–53, 2015.

[81] N. A. C. Z. B. Che, A. F. Ismail, and A. A. Majid, "Synthesis of thorium tetrafluoride (ThF_4) by ammonium hydrogen difluoride (NH_4HF_2)," *Nuclear Engineering and Technology*, vol. 51, no. 3, pp. 792 – 799, 2019.

[82] O. Beneš, J. P. M. van der Meer, and R. J. M. Konings, "Modelling and calculation of the phase diagrams of the LiF–NaF–RbF–LaF_3 system," *Calphad*, vol. 31, no. 2, pp. 209–216, 2007.

[83] M. Beilmann, O. Beneš, R. Konings, and T. Fanghänel, "Thermodynamic investigation of the (LiF+NaF+CaF_2+LaF_3) system," *The Journal of Chemical Thermodynamics*, vol. 43, no. 10, pp. 1515–1524, 2011.

[84] E. Sooby, A. Nelson, J. White, and P. McIntyre, "Measurements of the liquidus surface and solidus transitions of the $NaCl_3-UCl_3$ and $NaCl_3-UCl_3-CeCl_3$ phase diagrams," *Journal of Nuclear Materials*, vol. 466, pp. 280–285, 2015.

[85] R. Reddy, "Novel molten salts thermal energy storage for concetrating solar cell generation," presentation slides, The University of Alabama, Department of Metallurgial and Materials Engineering, 2013.

[86] G. J. Janz and D. J. Rogers, "Thermal behaviour of the potassium-sulfur electrolyte," *The Electrochemical Society*, no. 10.1149/198403.0322PV, pp. 322–334, 1984.

[87] O. Sotelo-Mazón, C. Cuevas-Arteaga, J. Porcayo-Calerón, V. Salinas Bravo, and G. Izquierdo-Montalvo, "Corrosion behaviour of pure Ce, Ni, Fe exposed to

molten salts at high temperature," *Advances in Materials Science and Engineering*, no. 923271, pp. 1–12, 2014.

[88] L. Olson, J. Ambrosek, K. Sridharan, M. Anderson, and T. Allen, "Materials corrosion in molten LiF – NaF – KF salt," *Journal of Fluorine Chemistry*, vol. 130, no. 1, pp. 67–73, 2009.

[89] P. Peretz, G. Hatem, M. Gaune-Escard, and M. Hoch, "The AlF_3-BaF_2-NaF molten salt system: calorimetric investigations and modelling," *Thermochimica Acta*, vol. 262, pp. 45 – 54, 1995.

[90] J. P. Young, "Windowless spectrophotometric cell for use with corrosive liquids," *Analytical Chemistry*, vol. 36, no. 2, pp. 390–392, 1964.

[91] A.-L. Rollet, C. Bessada, A. Rakhmatoulline, Y. Auger, P. Melin, M. Gailhanou, and D. Thiaudière, "In situ high temperature nmr and exafs experiments in rare-earth fluoride molten salts," *Comptes Rendus Chimie*, vol. 7, no. 12, pp. 1135 – 1140, 2004.

[92] A.-L. Rollet, C. Bessada, Y. Auger, P. Melin, M. Gailhanou, and D. Thiaudiere, "A new cell for high temperature exafs measurements in molten rare earth fluorides," *Nuclear Instruments and Methods in Physics Research Section B: Beam Interactions with Materials and Atoms*, vol. 226, no. 3, pp. 447 – 452, 2004.

[93] V. Lacassagne, C. Bessada, P. Florian, S. Bouvet, B. Ollivier, J.-P. Coutures, and D. Massiot, "Structure of high-temperature $NaF-AlF_3-Al_2O_3$ melts: A multinuclear NMR study," *The Journal of Physical Chemistry B*, vol. 106, no. 8, pp. 1862–1868, 2002.

[94] E. Robert and B. Gilbert, "Raman Spectroscopy Study of Molten $M_xAlF_{3+x}-M_xAlF_{3+x}$ Systems (M = Li, Na, K)," *Applied Spectroscopy*, vol. 54, no. 3, pp. 396–401, 2000.

[95] A. Maria, E. Millam, and C. Wright, "Using a differential scanning calorimeter to teach phase equilibiria to students of igneous and metamorphic petrology," *Journal of Geoscience Education*, vol. 59, pp. 63–70, 2011.

[96] ASTM International, "Standard test method for temperature calibration of differential scanning calorimeters and differential thermal analyzers," Tech. Rep. E967-18, West Conshohocken, Pennsylvania, USA, 2018.

[97] ASTM International, "Standard practise for heat flow calibration of differential scanning calorimeters," Tech. Rep. E968-02, West Conshohocken, Pennsylvania, USA, 2014.

[98] ASTM International, "Standard test method for melting and crystallization temperatures by thermal analysis," Tech. Rep. E794-06, West Conshohocken, Pennsylvania, USA, 2018.

[99] NETZSCH Instruments North America, LLC, "Temperature and Sensitivity Calibrations for DSC," tech. rep., Analyzing & Testing Business Unit, 2017.

[100] L. Rycerz, "Practical remarks concerning phase diagrams determination on the basis of differential scanning calorimetry," *Journal of Analytical Calorimetry*, vol. 113, pp. 231–238, 2013.

[101] M. Tucker, "Private communication." 2019.

[102] J. Engel, H. Bauman, J. Dearing, W. Grimes, E. McCoy, and W. Rhoades, "Conceptual design characterstics of a denatured molten-salt reactor with once-through refuelling," Tech. Rep. ORNL-7207, Oak Ridge National Laboratory, Oak Ridge, Tennessee, USA, 1980.

[103] P. Sabharwall, M. Ebner, M. S. Sohal, P. Sharpe, M. Anderson, K. Sridharan, J. Ambrosek, L. Olson, and P. Brooks, "Molten salts for high temperature reactors university of Wisconsin molten salt corrosion and flow loop experiments

- issues identified and path forward," Tech. Rep. INL/EXT-10-18090, Idaho National Laboratory, Idaho Falls, USA, 2010.

[104] C. Davis, "Physical properties and correlations for the molten salt FLIBE and their implementation in the RELAP5/ATHENA thermal-hydraulics code," Tech. Rep. INEEL/EXT-05-02658, Idaho National Engineering and Environmental Laboratory, Idaho Falls, Idaho, USA, 2004.

[105] S. Boyd and C. Taylor, "Chemical fundamentals and applications of molten salts," in *Molten Salt Reactors and Thorium Energy* (T. J. Dolan, ed.), ch. 3, Woodhead Publishing, 2017.

[106] R. Serrano-López, J. Fradera, and S. Cuesta-López, "Molten salts database for energy applications," *Chemical Engineering and Processing: Process Intensification*, vol. 73, pp. 87–102, 2013.

[107] O. Beneš, S. Delpech, P. Hosnedl, V. Ignatiev, R. Konings, D. Lecarpentier, O. Matal, E. Merle-Lucotte, C. Renault, and J. Uhlir, "Assessment of Liquid Salts for Innovative Applications (ALISIA)," Review Report on Liquid Salts for Various Applications D-50, Eurpean Commision, 2009.

[108] R. C. Briant and A. M. Weinberg, "Molten fluorides as power reactor fuels," *Nuclear Science and Engineering*, vol. 2, pp. 797–803, Nov. 1957.

[109] George Flanagan, "ORNL Research and Demonstration Reactors," July 21 - 25 2010.

[110] W. Grimes, "Molten-salt reactor chemistry," *Nuclear Applications and Technology*, vol. 8, no. 2, pp. 137–155, 1970.

[111] W. Grimes, "Chemical research and development for molten salt breeder reactors," Tech. Rep. ORNL-TM-1853, Oak Ridge National Laboratory, 1967.

[112] P. N. Haubenreich and J. R. Engel, "Experience with the Molten-Salt Reactor Experiment," *Nuclear Applications and Technology*, vol. 8, no. 2, pp. 118–136, 1970.

[113] M. Seregin, A. Parshin, A. Kuznetsov, L. Ponomarev, and S. Mel'nikov, "Solubility of UF_4, ThF_4, and FeC_3 in the $NaF-ZrF_4$ melt," *Radiochemistry*, vol. 53, no. 1, pp. 69–72, 2011.

[114] *Physical and Chemical Feasibility of Fueling Molten Salt Reactors with TRU's Trifluorides*, no. INIS-FR-1128, (Paris, France), Global 2001 international conference on: back-end fuel cycle: from research on solutions, 2001.

[115] E. S. Bettis, R. Schroeder, G. Cristy, H. Savage, R. Affel, and R. Hemphill, "The Aircraft Reactor Experiment—Design and Construction," *Nuclear Science and Engineering*, vol. 2, pp. 804–825, 1957.

[116] A. Fraas and A. Savolainen, "Design report on the aircraft reactor experiment," Tech. Rep. ORNL-2095(Del.), Oak Ridge National Laboratory, Oak Ridge, Tennessee, USA, 1956.

[117] J. McWherter, "Molten salt breeder expeirment design bases," Tech. Rep. ORNL-TM-3177, Oak Ridge National Laboratory, Oak Ridge, Tennessee, USA, 1970.

[118] J. Krepel, "Molten salt reactor: sustainable and safe reactor for the future?," in *Nuclear energy and safety research division colloquium*, (Forschungsstrasse, Switzerland), Paul Scherrer Institut, 2016.

[119] E. S. Bettis and R. C. Robertson, "The Design and Performance Features of a Single-Fluid Molten-Salt Breeder Reactor," *Nuclear Applications and Technology*, vol. 8, no. 2, pp. 190–207, 1970.

[120] D. Heuer, E. Merle-Lucotte, M. Allibert, M. Brovchenko, V. Ghetta, and P. Rubiolo, "Towards the thorium fuel cycle with molten salt fast reactors," *Annals of Nuclear Energy*, vol. 64, pp. 421–429, 2014.

[121] L. Mathieu, D. Heuer, R. Brissot, C. L. Brun, E. Liatard, J. M. Loiseaux, O. Méplan, E. Merle-Lucotte, A. Nuttin, J. Wilson, C. Garzenne, D. Lecarpentier, and E. Walle, "The Thorium Molten Salt Reactor : Moving on from the MSBR," *Progress in Nuclear Energy*, vol. 48, no. 7, pp. 664–679, 2006.

[122] E. Merle-Lucotte, D. Heuer, C. L. Brun, L. Mathieu, R. Brissot, E. Liatard, O. Meplan, and A. Nuttin, "Fast Thorium Molten Salt Reactors Started With Plutonium," in *ICAPP '06: International Congress on Advances in Nuclear Power Plants*, no. 6132, (Reno, NV, USA), 2006.

[123] "ISTC Project #1606 Final Report," Tech. Rep. 1606, Moscow, Russia, 2004.

[124] V. Ignatiev, O. Feynberg, I. Gnidoi, A. Merzlyakov, A. Surenkov, V. Uglov, A. Zagnitko, V. Subbotin, I. Sannikov, A. Toropov, V. Afonichkin, A. Bovet, V. Khokhlov, V. Shishkin, M. Kormilitsyn, A. Lizin, and A. Osipenko, "Molten salt actinide recycler and transforming system without and with Th–U support: Fuel cycle flexibility and key material properties," *Annals of Nuclear Energy*, vol. 64, pp. 408–420, 2014.

[125] X. Hongjie, X. Cai, and W. Guo, "Thorium Energy R&D in China," Oct. 2013.

[126] "Status report-MSR-FUJI," tech. rep., International Atomic Energy Agency, Vienna, Austria, 2016.

[127] V. Kuznetsov, "Status of Small Reactor Designs Wihout On-Site Refuelling," 2007.

[128] D. Cooper, "Making nuclear sustainable," in *Thorium Energy Conference*, (Brussels), Seaborg Technologies, 2018.

[129] T. Pedersen, "Copenhagen atomics waste burner in 5 minutes," 2016. Commercial video from Copenhagen Atomics.

[130] "Status report-ThorCon," tech. rep., International Atomic Energy Agency, Vienna, Austria, 2016.

[131] "Status report-LFTR," tech. rep., International Atomic Energy Agency, Vienna, Austria, 2016.

[132] P. Vijayan, A. Basak, I. Dulera, K. Vaze, S. Basu, and R. Sinha, "Conceptual design of indian molten salt breeder reactor," *Pramana Journal of Physics*, vol. 85, no. 3, pp. 539–554, 2015.

[133] "Status report-IMSR-400," tech. rep., International Atomic Energy Agency, Vienna, Austria, 2016.

[134] A. Owens, "Stable salt reactors - a roadmap to thorium," in *Thorium Energy Conference*, (Brussels, Belgium), Moltex, 2018.

[135] "Status report-SSR-U," tech. rep., International Atomic Energy Agency, Vienna, Austria, 2016.

[136] E. Compere, S. Kirslis, E. Bohlmann, F. Blankenship, and W. Grimes, "Fission product behavior in the molten salt recator experiment," Tech. Rep. ORNL-4865, Oak Ridge National Laboratory, Oak Ridge, Tennessee, USA, 1975.

[137] V. V. Ignatiev, O. S. Feynberg, A. V. Zagnitko, A. V. Merzlyakov, A. I. Surenkov, A. V. Panov, V. G. Subbotin, V. K. Afonichkin, V. A. Khokhlov, and M. V. Kormilitsyn, "Molten-salt reactors: New possibilities, problems and solutions," *Atomic Energy*, vol. 112, no. 3, pp. 157–165, 2012.

[138] V. Ignatiev, O. Feynberg, I. Gnidoi, A. Merzlyakov, V. Smirnov, A. Surenkov, I. Tretiakov, R. Zakirov, V. Afonichkin, A. Bovet, V. Subbotin, A. Panov, A. Toropov, and A. Zherebtsov, "Progress in Development of Li,Be,Na/F Molten

Salt Actinide Recycler & Transmuter Concept," *Proceedings of ICAPP 2007*, no. 7548, 2007.

[139] O. Beneš and R. Konings, "Actinide burner fuel potential compositions based on the thermodynamic evaluation of mf−puf_3 (m=li,na,k,rb,cs and laf_3−puf_3 systems," *Journal of Nuclear Materials*, vol. 377, no. 3, pp. 449–457, 2008.

[140] O. Beneš and R. Konings, "Thermodynamic evaluation of the (LiF+NaF+BeF_2+PuF_3) system: An actinide burner fuel," *The Journal of Chemical Thermodynamics*, vol. 41, no. 10, pp. 1086–1095, 2009.

[141] C. Yu, X. Li, X. Cai, C. Zou, Y. Ma, J. Han, and J. Chen, "Analysis of minor actinides transmutation for a Molten Salt Fast Reactor," *Annals of Nuclear Energy*, vol. 85, pp. 597–604, 2015.

[142] B. Fitzpatrick, P. Bajpai, D. Hallatt, K. Lipkina, M. Poschmann, and M. Piro, "Progress in experimental and computational investigations for small modular reactors," in *14th International Conference on CANDU Fuel*, (Mississauga, ON, Canada), 2019.

[143] G. Silva, *Evaluation of low-temperature fluoride routes to synthesize actinide nitrides and oxide solid solutions*. Doctoral thesis, University of Nevada, Las Vegas, Las Vegas, Nevada, USA, 2009.

[144] G. Chinthaka Silva, C. Yeamans, G. Cerefice, A. Sattelberger, and K. Czerwinski, "Synthesis and nanoscale characterization of $(NH_4)_4ThF_8$ and Th_4F," *Inorganic Chemistry*, vol. 48, no. 13, pp. 5736–5746, 2009.

[145] ASTM International, "Standard test method for sieve analysis of metal powders," Tech. Rep. B214-16, West Conshohocken, Pennsylvania, USA, 2016.

[146] P. Vichos, "Private communication." 2019.

[147] O. Beneš, "Private communication." 2019.

[148] Special Metals, "Nickel 200 & 201 Data Sheet," tech. rep., Special Metals, 2016.

[149] R. Kirby, "Platinum - a thermal expansion reference material," *International Journal of Thermophysics*, vol. 12, no. 4, pp. 679–685, 1991.

[150] Saint-Gobain, "Combat boron nitride solids production data sheet," Tech. Rep. ISO-9001, ISO-14001, Saint-Gobain, 2017.

[151] 2019.

[152] BU Analyzing & Testing, "Key technical data sta 449 f3 jupiter," *NETZSCH-Gerätebau GmbH*, 2019.

[153] E. Ferreira, M. Lima, and E. Zanotta, "Dsc method for determining the liquidus temperature of glass-forming systems," *Journal of American Ceramics*, vol. 93, no. 11, pp. 3757–3763, 2010.

[154] Analysing & Testing Business Unit, *Introduction to Simultaneous Thermal Analysis Method: Measuring Principle, TGA-DSC/DTA Instruments and Accessories*. NETZSCH Instruments North America, LLC, 2017.

[155] E. Gmelin and S. Sarge, "Calibration of differential scanning calorimeters," *Pure and Applied Chemistry*, vol. 67, no. 11, pp. 1789–1800, 1995.

[156] K. Johnson, "Private communication." University of South Carolina 2019.

[157] ASTM International, "Standard practise for microetching metals and alloys," Tech. Rep. E407-07e1, West Conshohocken, Pennsylvania, USA, 2015.

[158] E. Geiger and M. Poschmann, "Standard operating procedure: X-ray diffraction." Ontario Tech University, 2019.